Multiscale Structure of Turbulent Channel Flow and Polymer Dynamics in Viscoelastic Turbulence

This thesis is submitted in fulfilment of the requirements
for the degree of Doctor of Philosophy of the Imperial College London

by

Vassilios Dallas

Department of Aeronautics &
Institute for Mathematical Sciences
Imperial College London
53 Prince's Gate
London SW7 2PG

2010

Abstract

This thesis focuses on two important issues in turbulence theory of wall-bounded flows. One is the recent debate on the form of the mean velocity profile (is it a log-law or a power-law with very weak power exponent?) and on its scalings with Reynolds number. In particular, this study relates the mean flow profile of the turbulent channel flow with the underlying topological structure of the fluctuating velocity field through the concept of critical points, a dynamical systems concept that is a natural way to quantify the multiscale structure of turbulence. This connection gives a new phenomenological picture of wall-bounded turbulence in terms of the topology of the flow. This theory validated against existing data, indicates that the issue on the form of the mean velocity profile at the asymptotic limit of infinite Reynolds number could be resolved by understanding the scaling of turbulent kinetic energy with Reynolds number.

The other major issue addressed here is on the fundamental mechanism(s) of viscoelastic turbulence that lead to the polymer-induced turbulent drag reduction phenomenon and its dynamical aspects. A great challenge in this problem is the computation of viscoelastic turbulent flows, since the understanding of polymer physics is restricted to mechanical models. An effective numerical method to solve the governing equation for polymers modelled as nonlinear springs, without using any artificial assumptions as usual, was implemented here for the first time on a three-dimensional channel flow geometry. The superiority of this algorithm is depicted on the results, which are much closer to experimental observations. This allowed a more detailed study of the polymer-turbulence dynamical interactions, which yields a clearer picture on a mechanism that is governed by the polymer-turbulence energy transfers.

I hereby declare that this thesis is my own work and effort and that the work of others is appropriately acknowledged.

Contents

List of Figures

List of Tables

Acknowledgements

I would like to express my gratitude to my supervisor, Prof. Christos Vassilicos, whose zest for scientific research, creativity and dedication saw me through this work. I would also like to thank him and my co-supervisor, Prof. Geoffrey Hewitt, for their guidance on how to approach scientific problems and for giving me the opportunity to be their fellow-traveller in this journey of knowledge.

I wish to thank all the members of the Turbulent, Mixing and Flow Control group and in particular the people in the Institute for Mathematical Sciences for making this PhD adventure a memorable one. I wish to sincerely thank Prof. Arkady Tsinober for his instructive criticism on the conceptual aspects of turbulence, as well as for his key suggestions on turbulence related literature. I am indebted to Martin Priego Wood for lending his time, interest and insight in several occasions during my research. My sincere thanks to Sylvain Laizet for providing me his Navier-Stokes solver and for his guidance through the code in my early stage; to Stuart Coleman for many enlightening discussions on several aspects; to the good computer wizards Dimitris Tasoulis and Nicos Pavlidis for making my life easier with the Linux kernel; and to Prof. James Brasseur, Prof. Lance Collins and Dr. Thirunavukkarasu Vaithianathan for useful discussions on their numerical algorithm for polymers.

I want to thank my friends, whose warmth and support is what kept me going many times these years. Nektarios Bampalas for imparting his romanticism about life; Andreas Mpentevis for always being a friend no matter the time and the distance; the “pareaki” back home for spending unforgettable times together; and her for always caring and supporting me.

Finally, its my deepest pride to thank here my family for their love and support. My journey has been their journey and this thesis is dedicated to them and to the honour of my grandfather Vassilios Dallas, who was encouraging me in this journey until the end of his life.

ITHAKA

As you set out for Ithaka
wish your trip is long,
full of adventure, full of discovery.
The Laestrygonas and the Cyclopas,
the wrathful Poseidona - don't let them scare you:
you'll never find such things on your way,
as long as you keep your thoughts raised high,
as long as rare excitement stirs your spirit and your body.
The Laestrygonas and the Cyclopas,
the wrathful Poseidona - you won't face them
unless you bring them along inside your soul,
unless your soul raises them before you.

Wish your trip is long.
Many the summer mornings when,
with what pleasure, what joy,
you enter harbours you're seeing for the first time;
may you stop at Phoenicians seaports
and get the finest wares,
mother of pearl and coral, amber and ebony
and sensual scents of every kind,
as many sensual perfumes as you can;
and may you visit many Egyptian cities,
to learn and keep on learning from their scholars.

Keep Ithaka always on your mind.
Arriving there is what you're destined for.
But don't hurry the journey at all.
Better if it lasts for years,
so that you're old when you cast your anchor in the island,
wealthy with all you've gained on the way,
not expecting any wealth from Ithaka.

Ithaka gave you the fine journey.
Without her you wouldn't have set out.
But she has nothing left to give you now.
And if you find her poor, Ithaka did not deceive you.
Wise as you now are, with such experience,
you have already understood what Ithakas mean.

Constantinos. P. Kavafis (1911)

Chapter 1

Introduction

1.1 Overview

Leonardo da Vinci was the first to recognise two states of fluid motion and made use of the term *la turbolenza* (Frisch, 1995; Tsinober, 2002). His half a millennium old drawings (see Fig. 1.1) illustrate what we call today *turbulence*. After the pioneering works of Leonard Euler, Claude-Louis Navier, George G. Stokes on the governing equations of fluid motion and that of Osborne Reynolds on the concept of critical Reynolds number, the dimensionless number which expresses the balance between the nonlinear and dissipative properties of the flow and denotes the onset of turbulence, a large quest begun for a theory of turbulence with the involvement of great physicists and mathematicians like Heisenberg, Kolmogorov, Onsager, Richardson and many more. However, despite much effort the problem is far from solved.

Turbulence is one of the most difficult, open problems in classical physics and is also related to one of the hardest open problems in mathematics, the millennium problem of Navier-Stokes equations, which are the equations that govern the viscous fluid motion. A proof on the uniqueness of solutions of the three dimensional Navier-Stokes equations or equivalently the proof of regularity of the solutions is still lacking (Doering and Gibbon, 1995). In other words, there is no proof that given a smooth initial velocity field, the Navier-Stokes equations can keep smooth solutions for time $t \rightarrow \infty$ and this does not stop the creation of finite time singularities, meaning breakdown of the Navier-Stokes equations as governing equation for a continuum field as the velocity field. A regularity proof is also important for the numerical

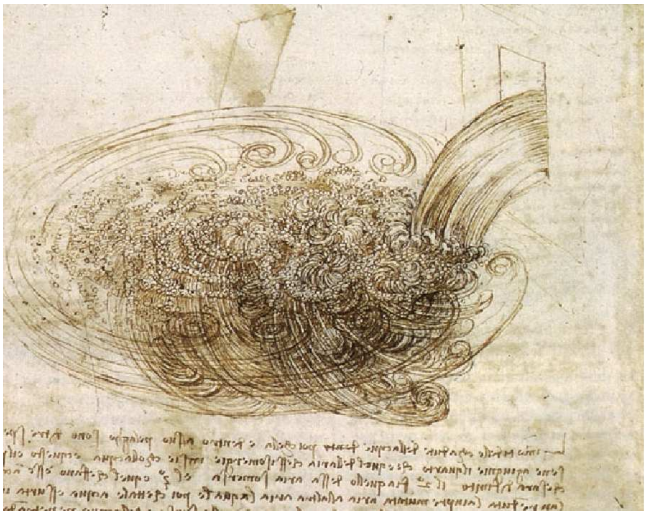

Figure 1.1: Studies of turbulence in water by Leonardo da Vinci. Courtesy Kemp (2004).

computations, since regularity is connected with the necessary resolution to capture the precise turbulence dynamics. The only theory that exists is Kolmogorov's for homogeneous, isotropic turbulence, which is phenomenological and is based on scaling and similarity arguments (Frisch, 1995). Therefore, rigour is far from achieved in turbulence theory.

Since Reynolds' work, the turbulent boundary layer has been a paradigm in the field of turbulence. Prandtl was the first to give a systematic account of the turbulent boundary layer (Oertel, 2004), followed by Schlichting (Schlichting and Gersten, 2000). Von Kármán obtained a logarithmic expression for the mean velocity profile, in an intermediate sublayer between the wall and the outer part of a boundary layer using similarity arguments (Tennekes and Lumley, 1972), which was a major result for wall-bounded turbulence. The importance of flow structure was highlighted by Kline et al. (1967) and Townsend (1976). Since then, the interaction between the flow structure and scaling properties of the wall-bounded turbulence has been the subject of major study. Over the past decade experimental measurements and numerical computations at Reynolds numbers much higher than before have focused on the form of the boundary-layer scaling, re-examining the basis of asymptotic scaling relationships on a debate between logarithmic and power-law scaling of the mean velocity profile and on whether this profile is universal for channel, pipe and boundary layer flows (McKeon, 2007).

Turbulent flow is not only the vibrations experienced during flight, it is the shape of the clouds and that of smoke rising from a cigarette, the flow of water and oil in pipes, the wake of a vehicle or a ship, the currents in rivers and oceans, the the solar and Earth's atmosphere, the formation of galaxies. Numerous practical applications of turbulence arise in aeronautics, plasma physics, chemical and nuclear engineering, cryogenic engineering, nonlinear optics, biological sciences, geophysics and meteorology. Therefore, turbulence is central to flow technology and the need for flow control and energy savings is vital for a vast range of applications.

In 1948, Toms (1948) was the first to realise that the addition of small amounts of long chain polymer molecules to wall-bounded turbulent flows can reduce drag drastically. Only, a few parts per million of polymer in solution can achieve up to 70% drag reduction. Although this phenomenon – while perhaps a possible candidate for the title of the "most difficult open problem in classical mechanics" or in physics, according to McComb (1992) – has been known for almost sixty years, the underlying mechanisms, through which the introduction of polymers alter the fluid's rheological behaviour in such a way that modify vortex structures and lead to drag reduction, have not yet been fully elucidated. Several conceptual models have been proposed for the phenomenon of polymer-induced drag reduction and all have been subjected to criticism. The two phenomenologies that are still under consideration, because some of their concepts find support from computational and experimental results, are the time-criterion/coil-stretch transition by Lumley (1969, 1973) and the elastic theory of Tabor and de Gennes (1986); De Gennes (1990). Both theories, however, are extremely conjectural and somewhat qualitative, failing to explain the dynamics of drag reduction by polymers in wall-bounded turbulence.

A result of major significance in polymer drag reduction of wall-bounded turbulent flows was obtained by Virk et al. (1967); Virk (1975). They observed that the mean velocity profile has an universal asymptotic limit independent of the Newtonian solvent, the nature of the polymer additives and flow geometry (Virk, 1975; Virk et al., 1997; Benzi et al., 2005). This asymptotic limit is called the Maximum Drag Reduction (MDR) or Virk's asymptote, where the flow does not relaminarise and velocity fluctuations reach a self-sustaining state. The existence of this asymptote indicates that drag reduction is not a purely viscous effect (De Gennes, 1990; Sreenivasan and White, 2000). However, no generally accepted theory has been provided to explain adequately the MDR law and its universality.

This study addresses two cornerstones in turbulence theory of wall-bounded turbulence. One is on the recent issues raised for the mean velocity profile (McKeon, 2007) that were mentioned above and its relation to the multiscale flow structure of wall-bounded turbulence. The other is on the conceptual aspects of polymer-turbulence interactions in viscoelastic turbulence and polymer-induced drag reduction (White and Mungal, 2008). The thesis is organised as follows. A brief introduction on the classical theory of hydrodynamic wall-bounded turbulence is given in chapter 2 including some of the necessary terminology and machinery that was employed in this work. Chapter 3 focuses on the mean flow profile and its relation to the underlying flow topology in turbulent channel flow, applying the concept of stagnation points of the fluctuating velocity field. This approach with the aid of Direct Numerical Simulations (DNS) led to a novel phenomenology for the scaling of the mean velocity gradient.

The classical phenomenology of hydrodynamic turbulence is not obeyed by wall-bounded turbulent flows with active additives, such as polymer molecules that have a feedback on the flow field. Therefore, a background introduction on the theory of polymeric fluids and their modelling is included in chapter 4, reviewing also the relevant phenomenologies of drag reduction by polymers. Then, chapter 5 provides details on the current state in DNS of viscoelastic turbulence and the present numerical method to solve the governing equations for the polymer molecules, which was applied here for the first time in a wall-bounded flow, validating it with an analytical solution. The statistics collected by DNS of viscoelastic turbulent channel flow are presented in chapter 6, where an enhanced conceptual mechanism is proposed for the phenomenon of polymer-induced drag reduction and important indications are revealed on the polymer dynamics and the conservation of turbulence at maximum drag reduction. In the end, the most important results presented in this thesis are outlined, emphasizing their implications and further views are suggested under which aspects this research could be advanced (see chapter 7).

Chapter 2

Hydrodynamic wall-bounded turbulence: a brief introduction

A brief introduction on the basic concepts and phenomenology of the classical theory of hydrodynamic wall-bounded turbulence is given in this chapter before moving to some further results on the mean flow of turbulent channel flow. The aim here is to introduce, for the sake of self-consistency, some of the necessary terms and concepts that will be used later in the thesis. The chapter starts with the description of Navier-Stokes equations for an incompressible flow and the phenomenon of anomalous dissipation in the asymptotic limit of vanishing viscosity, which is of fundamental importance in turbulent flows (see section 2.1). The basic statistical decomposition of the flow field by Reynolds, the Reynolds stress tensor and the balance between production and dissipation rate of turbulent kinetic energy are introduced in section 2.2. Then, section 2.3 presents the theory behind turbulent channel flow and the classical intermediate asymptotics for the mean velocity profile. This section also includes some analogies that exist between the relevant phenomenologies of homogeneous and wall-bounded turbulence. Concepts on structural and topological aspects of turbulent flows are outlined in section 2.4 with more emphasis on the critical points in turbulent flows, which are the essential ingredients for some results in this thesis.

2.1 Conservation Laws

The fundamental equations of fluid mechanics are derived from three basic principles: (*i*) mass conservation, (*ii*) Newton's second law: the rate of change of momentum of a portion of the fluid equals the forces applied to it and (*iii*) energy balance. In detail, the conservation of mass per unit volume manifests itself as the *continuity equation*

$$D_t\rho + \rho\boldsymbol{\nabla}\cdot\boldsymbol{u} = 0 \tag{2.1}$$

and Newton's second law of motion as Cauchy's equation (Ottino, 1989)

$$D_t u_i = \frac{1}{\rho}\partial_{x_j}\sigma_{ij} + f_i \tag{2.2}$$

where $\boldsymbol{u}(\boldsymbol{x},t)$ is the velocity vector of a fluid element located in position $\boldsymbol{x}$ at time t in the Euclidean space $\mathbb{R}^3$, $\rho(\boldsymbol{x},t)$ is the fluid density, $\sigma_{ij}(\boldsymbol{x},t)$ is the stress tensor and f_i embodies any external force, such as gravity, etc. The fundamental kinematic principle is contained in the notion of the operator $D_t \equiv \partial_t + (\boldsymbol{u}\cdot\boldsymbol{\nabla})$, which is called the *material* or *Lagrangian* derivative that represents the rate of change with respect to an observer moving with the fluid. It can be easily derived for a fluid particle using the chain rule of differentiation. Eq. (2.2) is valid for any continuous medium but for a Newtonian fluid, the stress tensor is assumed to be isotropic and a linear function of the strain rate tensor $S_{ij} \equiv 1/2(\partial_{x_j}u_i + \partial_{x_i}u_j)$, i.e. the deviation of the fluid motion from a rigid body motion. So, it is found (Aris, 1962; Batchelor, 1967) that

$$\sigma_{ij} = -p\delta_{ij} + \mu\left[(\partial_{x_j}u_i + \partial_{x_i}u_j) - \frac{2}{3}\partial_k u_k\delta_{ij}\right] \tag{2.3}$$

where p is the hydrodynamic pressure, μ the constant uniform dynamic viscosity of the fluid and δ_{ij} is the Kronecker delta*. Hence, from Eq. (2.2) one can now obtain, using expression (2.3) for the stress tensor, the general form of the *Navier-Stokes equations*

$$D_t\boldsymbol{u} = -\frac{1}{\rho}\boldsymbol{\nabla}p + \nu\left[\boldsymbol{\Delta u} + \frac{1}{3}\boldsymbol{\nabla}(\boldsymbol{\nabla}\cdot\boldsymbol{u})\right] + \boldsymbol{f} \tag{2.4}$$

where the material parameter $\nu = \mu/\rho$ is the fluid's kinematic viscosity and $\boldsymbol{\Delta} \equiv \boldsymbol{\nabla}^2$ is the Laplacian operator.

*δ_{ij} is equal to 1 if $i = j$ and 0 otherwise.

This study considers incompressible fluids, that is, the mass density is constant following the fluid, viz. $D_t\rho = 0$. If the fluid is homogeneous, i.e. $\rho = const$ in space, it follows that the flow is incompressible if and only if ρ is constant in time. Physically, this constraint restricts applicability to problems where velocities much smaller than the speed of sound are considered (Doering and Gibbon, 1995). Mathematically, the kinematic condition of incompressibility can be deduced from continuity equation (2.1) imposing the velocity field to be solenoidal, i.e. $\boldsymbol{\nabla} \cdot \boldsymbol{u} = 0$. An analogous interpretation of incompressibility comes from Euler's lemma (Aris, 1962; Chorin and Marsden, 1979)

$$\partial_t J = (\boldsymbol{\nabla} \cdot \boldsymbol{u}) J \Rightarrow \partial_t \ln J = \boldsymbol{\nabla} \cdot \boldsymbol{u} \tag{2.5}$$

where $J = \frac{\mathrm{d}V}{\mathrm{d}V_o}$ is essentially the Jacobian and here represents the expansion or dilatation of a volume element. Thus, incompressibility is equivalent to $J \equiv 1$, which implies $\boldsymbol{\nabla} \cdot \boldsymbol{u} = 0$ through Eq. (2.5).

Primarily, the dynamics of the spatiotemporal velocity variations of an incompressible Newtonian fluid are determined by the Navier-Stokes equations, supplemented by the divergence free condition

$$\begin{gathered} \partial_t \boldsymbol{u} + (\boldsymbol{u} \cdot \boldsymbol{\nabla})\boldsymbol{u} = -\frac{1}{\rho}\boldsymbol{\nabla} p + \nu \boldsymbol{\Delta} \boldsymbol{u} + \boldsymbol{f} \\ \boldsymbol{\nabla} \cdot \boldsymbol{u} = 0 \end{gathered} \tag{2.6}$$

with the velocity vector field satisfying the periodic and/or no-slip boundary conditions

$$\boldsymbol{u}|_{\partial\Omega} = 0. \tag{2.7}$$

A brief description of the different terms of the equations is given below:

- $(\boldsymbol{u} \cdot \boldsymbol{\nabla})\boldsymbol{u}$ is the inertial or convective term responsible for the advection of the velocity field and the sweeping of small scales by the larger ones in turbulent flows. Physically, this sweeping couples any given small scale of motion to all the larger scales. Moreover, this quadratic nonlinearity accounts for the local interscale energy transfer and the generation of small scale fluctuations from larger ones until viscosity dominates.

- $-\boldsymbol{\nabla} p/\rho$ is the pressure gradient term, which is dimensionally equivalent to

$(\boldsymbol{u}\cdot\boldsymbol{\nabla})\boldsymbol{u}$. This term is also nonlinear in the velocity with the pressure being determined at any given point by the velocity field everywhere. Mathematically, this effect can be seen through a Poisson equation by taking the diverge of Eq. (2.6) and imposing the solenoidal nature of the velocity field

$$\boldsymbol{\Delta}p = -\rho\boldsymbol{\nabla}\cdot(\boldsymbol{u}\cdot\boldsymbol{\nabla}\boldsymbol{u}) = -\rho\partial_{x_j}u_i\partial_{x_i}u_j. \tag{2.8}$$

The satisfaction of the Poisson equation is a necessary and sufficient condition for the flow to remain incompressible. The inversion of the Laplacian in Eq. (2.8), which involves an integral operator over all space[†], gives the pressure field as a non-local functional of the instantaneous flow configuration. Theoretically, the Navier-Stokes equations at the incompressible limit propagate information through pressure waves that travel infinitely fast with velocity fluctuations being instantaneously correlated over long ranges (Doering and Gibbon, 1995).

- $\nu\boldsymbol{\Delta}\boldsymbol{u}$ is the viscous diffusion term, which distinguishes incompressible Navier-Stokes equations from incompressible Euler equations for an ideal fluid. It is introduced by the linear coupling between stress and rate of strain. Its net effect is to dissipate kinetic energy of the flow and convert it into heat.

The set of parameters in the Navier-Stokes equations (2.6) can be reduced by introducing dimensionless variables. In such a case, the Reynolds number is the only dimensionless parameter in the equations given by the expression

$$\mathcal{R}e = \frac{u_\ell \ell}{\nu} \tag{2.9}$$

where u_ℓ and ℓ being respectively a characteristic velocity and length scale of the flow, respectively. $\mathcal{R}e$ was introduced by Osborne Reynolds (1883), who showed that transition between laminar and turbulent flow occurs when Reynolds number reaches a critical value. The Reynolds number plays a fundamental role in turbulence because it expresses the relative strength of inertial forces to viscous forces, i.e.

$$\frac{(\boldsymbol{u}\cdot\boldsymbol{\nabla})\boldsymbol{u}}{\nu\boldsymbol{\Delta}\boldsymbol{u}} \propto \frac{u_\ell \ell}{\nu}. \tag{2.10}$$

[†] $\boldsymbol{\Delta}^{-1} \equiv \boldsymbol{\nabla}^{-2} = \int_\Omega G(\boldsymbol{x},\boldsymbol{r})\mathrm{d}^3 r$, where $G(\boldsymbol{x},\boldsymbol{r})$ is the Green's function for the three-dimensional Laplacian operator depending on boundary conditions imposed on domain Ω (Arfken and Weber, 2000).

It can also be interpreted as a measure of the nonlinearity of Navier-Stokes equations with fully developed turbulence achieved at high enough $\mathcal{R}e$ and the inertial term playing a dominant role in the dynamics.

The kinetic energy per unit mass in the fluid is

$$\mathcal{E} \equiv \int_\Omega \frac{1}{2}|\boldsymbol{u}|^2 \mathrm{d}^3x \tag{2.11}$$

integrated over a bounded domain $\Omega \subset \mathbb{R}^3$, with rigid boundary $\partial\Omega$. Then the evolution equation of energy can be derived by taking the time derivative of kinetic energy and using Navier-Stokes equations, viz.

$$\begin{aligned}\frac{\mathrm{d}\mathcal{E}}{\mathrm{d}t} &= \int \boldsymbol{u}\cdot\partial_t\boldsymbol{u}\mathrm{d}^3x \\ &= -\int \boldsymbol{u}\cdot\left[(\boldsymbol{u}\cdot\boldsymbol{\nabla})\boldsymbol{u} + \frac{1}{\rho}\boldsymbol{\nabla}p - \nu\boldsymbol{\Delta}\boldsymbol{u} - \boldsymbol{f}\right]\mathrm{d}^3x.\end{aligned} \tag{2.12}$$

Now treating each term separately and using the fact that $\boldsymbol{\nabla}\cdot\boldsymbol{u} = 0$, it yields that

$$\boldsymbol{u}\cdot(\boldsymbol{u}\cdot\boldsymbol{\nabla})\boldsymbol{u} = \frac{1}{2}\boldsymbol{u}\cdot\boldsymbol{\nabla}|\boldsymbol{u}|^2 = \frac{1}{2}\boldsymbol{\nabla}\cdot(\boldsymbol{u}|\boldsymbol{u}|^2), \tag{2.13}$$

$$\frac{1}{\rho}\boldsymbol{u}\cdot\boldsymbol{\nabla}p = \frac{1}{\rho}\boldsymbol{\nabla}\cdot(\boldsymbol{u}p) \tag{2.14}$$

and

$$-\nu\boldsymbol{u}\cdot(\boldsymbol{\Delta}\boldsymbol{u}) = \nu\boldsymbol{u}\cdot\boldsymbol{\nabla}\times\boldsymbol{\omega} = \nu|\boldsymbol{\omega}|^2 - \nu\boldsymbol{\nabla}\cdot(\boldsymbol{u}\times\boldsymbol{\omega}) \tag{2.15}$$

where $\boldsymbol{\omega} \equiv \boldsymbol{\nabla}\times\boldsymbol{u}$ is the vorticity vector. Then, gathering the above equations and applying the divergence theorem as well as the periodic and/or no-slip boundary conditions (Eq. (2.7)), one finds

$$\begin{aligned}\frac{\mathrm{d}\mathcal{E}}{\mathrm{d}t} &= \int \boldsymbol{\nabla}\cdot\left[-\frac{1}{2}\boldsymbol{u}|\boldsymbol{u}|^2 - \frac{1}{\rho}\boldsymbol{u}p + \nu(\boldsymbol{u}\times\boldsymbol{\omega})\right] - \nu|\boldsymbol{\omega}|^2 + \boldsymbol{u}\cdot\boldsymbol{f}\mathrm{d}^3x \\ &= \int\left[-\frac{1}{2}\rho\boldsymbol{u}|\boldsymbol{u}|^2 - \frac{1}{\rho}\boldsymbol{u}p + \nu(\boldsymbol{u}\times\boldsymbol{\omega})\right]\cdot\boldsymbol{n}\mathrm{d}^2x - \nu\int|\boldsymbol{\omega}|^2\mathrm{d}^3x + \int\boldsymbol{u}\cdot\boldsymbol{f}\mathrm{d}^3x \\ &= -2\nu\varpi + \int\boldsymbol{u}\cdot\boldsymbol{f}\mathrm{d}^3x\end{aligned} \tag{2.16}$$

where $\varpi \equiv \int \frac{1}{2}|\boldsymbol{\omega}|^2\mathrm{d}^3x$ is the enstrophy per unit mass.

It is important to state here that real viscous dissipation manifests itself through the viscous part of the stress tensor, i.e. $\sigma_{ij}^{(v)} = 2\rho\nu S_{ij}$, essentially the strain rate and not from enstrophy, which typically represents solid rotation of the fluid (Tennekes and Lumley, 1972; Frisch, 1995; Tsinober, 2002). It can be shown that using the incompressibility condition and the fact that the integral of the divergence vanishes for periodic and/or no-slip boundaries where necessary, then

$$\begin{aligned}
-\nu \int \boldsymbol{u} \cdot (\boldsymbol{\Delta u}) \mathrm{d}^3x &= -\frac{1}{\rho} \int u_i \partial_{x_j} \sigma_{ij}^{(v)} \mathrm{d}^3x \\
&= -\frac{1}{\rho} \int \partial_{x_j} u_i \sigma_{ij}^{(v)} \mathrm{d}^3x + 2\nu \int S_{ij} S_{ij} \mathrm{d}^3x \\
&= 2\nu \int S_{ij} S_{ij} \mathrm{d}^3x \\
&= \nu \int \partial_{x_j} u_i \partial_{x_j} u_i + \partial_{x_j} u_i \partial_{x_i} u_j \mathrm{d}^3x \\
&= \nu \int \partial_{x_j} u_i \partial_{x_j} u_i \mathrm{d}^3x + \nu \int \partial_{x_j} (u_i \partial_{x_i} u_j) - u_i \partial_{x_j} \partial_{x_i} u_j \mathrm{d}^3x \\
&= \nu \int |\boldsymbol{\nabla u}|^2 \mathrm{d}^3x
\end{aligned} \tag{2.17}$$

and

$$\begin{aligned}
\nu \int |\boldsymbol{\omega}|^2 \mathrm{d}^3x &= \nu \int \epsilon_{ijk} \epsilon_{ilm} \partial_{x_j} u_k \partial_{x_l} u_m \mathrm{d}^3x \\
&= \nu \int (\delta_{jl}\delta_{km} - \delta_{jm}\delta_{kl}) \partial_{x_j} u_k \partial_{x_l} u_m \mathrm{d}^3x \\
&= \nu \int \partial_{x_j} u_k \partial_{x_j} u_k - \partial_{x_j} u_k \partial_{x_k} u_j \mathrm{d}^3x \\
&= \nu \int |\boldsymbol{\nabla u}|^2 \mathrm{d}^3x
\end{aligned} \tag{2.18}$$

where ϵ_{ijk} is the Levi-Civita symbol[‡]. Ultimately, in this particular case the following expression holds for the viscous dissipation rate per unit mass

$$\tilde{\varepsilon} \equiv 2\nu \int S_{ij} S_{ij} \mathrm{d}^3x = \nu \int |\boldsymbol{\omega}|^2 \mathrm{d}^3x. \tag{2.19}$$

In the absence of external forcing and for $\nu = 0$, where the incompressible Euler

[‡] ϵ_{ijk} is 1 if (i, j, k) is an even permutation of $(1, 2, 3)$, -1 if it is an odd permutation and 0 if any index is repeated.

equations are recovered, Eq. (2.16) implies that the kinetic energy is conserved. Note though that in the limit $\nu \to 0$, the energy dissipation rate does not vanish but reaches some finite value (Frisch, 1995),

$$\lim_{\nu \to 0} 2\nu\varpi = \tilde{\varepsilon}. \tag{2.20}$$

This implies that as $\nu \to 0$ the enstrophy must grow as $\varpi \propto \nu^{-1}$ to compensate the decreasing viscosity. This unbounded growth of enstrophy is the physical origin of the so called *dissipation anomaly* in three-dimensional turbulence. This behaviour in the limit $\mathcal{R}e \to \infty$ is a consequence of the vortex stretching mechanism that produces extreme velocity gradients (Doering and Gibbon, 1995; Frisch, 1995).

2.2 Reynolds equations

The random spatiotemporal variation of the turbulent flow field renders the statistical approach imperative. The classical approach to turbulence theory to extract the relevant mean physical quantities is *Reynolds decomposition* (Tennekes and Lumley, 1972; Pope, 2000), where the basic idea is to decompose the turbulent velocity vector field into a mean and a fluctuating part

$$\boldsymbol{u} = \langle \boldsymbol{u} \rangle + \boldsymbol{u}' \tag{2.21}$$

with $\langle \boldsymbol{u} \rangle$ the time averaged component of the velocity field,

$$\langle \boldsymbol{u} \rangle = \lim_{T \to \infty} \frac{1}{T} \int_0^T \boldsymbol{u}(\boldsymbol{x}, t) \mathrm{d}t \tag{2.22}$$

and $\boldsymbol{u}'$ the time-dependent fluctuating part with zero mean by definition, viz.

$$\langle \boldsymbol{u}' \rangle \equiv 0. \tag{2.23}$$

Supposing that the time averages of temporal derivatives vanish and time averages commute with spatial derivatives, one can derive the *Reynolds equations*

$$\langle \boldsymbol{u} \rangle \cdot \boldsymbol{\nabla} \langle \boldsymbol{u} \rangle = -\frac{1}{\rho} \boldsymbol{\nabla} \langle p \rangle + \nu \boldsymbol{\Delta} \langle \boldsymbol{u} \rangle - \partial_{x_j} \left\langle u_i' u_j' \right\rangle + \boldsymbol{f}, \tag{2.24}$$

$$\boldsymbol{\nabla} \cdot \langle \boldsymbol{u} \rangle = 0. \tag{2.25}$$

Note that turbulence gives rise to an additional stress driving the mean flow $\sigma_{ij}^{(t)} \equiv -\rho \left\langle u_i' u_j' \right\rangle$, called the *Reynolds stress* tensor (Tennekes and Lumley, 1972; Pope, 2000) due to the nonlinearity of the inertial term, since averages of products give

$$\begin{aligned} \langle u_i u_j \rangle &= \left\langle (\langle u_i \rangle + u_i')(\langle u_j \rangle + u_j') \right\rangle \\ &= \langle u_i \rangle \langle u_j \rangle + \left\langle u_i' u_j' \right\rangle + \left\langle \langle u_i \rangle u_j' \right\rangle + \langle \langle u_j \rangle u_i' \rangle \\ &= \langle u_i \rangle \langle u_j \rangle + \left\langle u_i' u_j' \right\rangle . \end{aligned} \tag{2.26}$$

The Reynolds stress is an extra unknown to the problem and a stationary equation for the correlation $\left\langle u_i' u_j' \right\rangle$ may be supplied. However, this equation will involve higher order correlations as unknowns, such as $\left\langle u_i' u_j' u_k' \right\rangle$. The problem continues as one goes to higher order correlations and the hierarchy never closes. This is the nature of the so called *turbulence closure problem* (Tennekes and Lumley, 1972; Pope, 2000).

The balance equation for the mean kinetic energy of the turbulent velocity fluctuations $E \equiv \frac{1}{2} \langle |\boldsymbol{u}'|^2 \rangle = \frac{1}{2} \langle u_i' u_i' \rangle$ provides further insight into the dynamics of turbulent motion. This equation can be obtained through the governing equation for the Reynolds stress tensor, which can be derived from

$$\left\langle u_j' \mathcal{N}(u_i) + u_i' \mathcal{N}(u_j) \right\rangle = 0 \tag{2.27}$$

and using the Reynolds decomposition, where $\mathcal{N}(u_i)$ denotes the Navier-Stokes operator, viz.

$$\mathcal{N}(u_i) \equiv \partial_t u_i + u_j \partial_{x_j} u_i + \frac{1}{\rho} \partial_{x_i} p - \nu \partial_{x_j} \partial_{x_j} u_i. \tag{2.28}$$

Then, setting $i = j$ in the Reynolds stress equations, the turbulent kinetic energy balance follows

$$\langle u_j \rangle \, \partial_{x_j} E = -\partial_{x_j} \left(\frac{1}{\rho} \left\langle u_j' p' \right\rangle + \frac{1}{2} \left\langle u_i' u_j' u_j' \right\rangle - 2\nu \left\langle u_i' s_{ij} \right\rangle \right) + \mathcal{P} - \varepsilon \tag{2.29}$$

where $\frac{1}{\rho} \partial_{x_j} \left\langle u_j' p' \right\rangle$ represents the pressure gradient work, $\frac{1}{2} \partial_{x_j} \left\langle u_i' u_j' u_j' \right\rangle$ denotes transport by turbulent velocity fluctuations, $2\nu \partial_{x_j} \left\langle u_i' s_{ij} \right\rangle$ stands for transport by viscous

stresses, the production rate of turbulent kinetic energy is defined by

$$\mathcal{P} \equiv -\left\langle u_i' u_j' \right\rangle \partial_{x_j} \left\langle u_i \right\rangle \tag{2.30}$$

and the viscous energy dissipation rate due to turbulent fluctuating velocity gradients is

$$\varepsilon \equiv 2\nu \left\langle s_{ij} s_{ij} \right\rangle \tag{2.31}$$

with $s_{ij} \equiv 1/2(\partial_{x_j} u_i' + \partial_{x_i} u_j')$, the fluctuating strain rate.

In a statistically stationary and homogeneous turbulent shear flow (never homogeneous near a wall) the integrated over space Eq. (2.29), using the divergence theorem along with periodic boundary conditions by homogeneity, reduces to

$$-\int \left\langle u_i' u_j' \right\rangle \partial_{x_j} \left\langle u_i \right\rangle \mathrm{d}^3 x \simeq \int 2\nu \left\langle s_{ij} s_{ij} \right\rangle \mathrm{d}^3 x \tag{2.32}$$

stating that the rate of generation of turbulent energy by Reynolds stresses balances the rate of viscous dissipation (Tennekes and Lumley, 1972; Davidson, 2004). This is true in wall-bounded shear flows only in an intermediate region, away from the wall and the core of the flow.

2.3 Wall-bounded turbulent channel flow

The presence of a solid boundary in turbulent shear flows imposes the obvious constraint that the viscosity enforces the velocity of the fluid to be zero at a stationary solid surface (no-slip condition, see Eq. (2.7)), even when $\nu \to 0$ (Tennekes and Lumley, 1972). This viscous constraint gives rise to viscous characteristic scales that will be defined later in this section. The geometry of turbulent flows in channels and pipes with parallel walls prohibits the continuing growth of the boundary layer thickness, eventually becoming statistically independent of the downstream direction x. This is a major difference with external wall-bounded flows, i.e. boundary-layer flows, that avoids extra complications to the problem. This study focuses on turbulent flows in channels, so the theoretical analysis here is simplified.

Consider a turbulent flow of an incompressible fluid between two smooth parallel plates separated by a distance 2δ. The plates are long enough $L_x/\delta \gg 1$ and have a large aspect ratio $L_z/\delta \gg 1$ so that the flow is statistically independent of the x and z

directions (see Fig. 2.1), with periodic boundary conditions applied for $\boldsymbol{u} \equiv (u, v, w)$ in these directions assuming flow homogeneity. No-slip boundary conditions are applied to the bottom and top walls, respectively, i.e.

$$\boldsymbol{u}|_{y=0} = \boldsymbol{u}|_{y=2\delta} = 0. \tag{2.33}$$

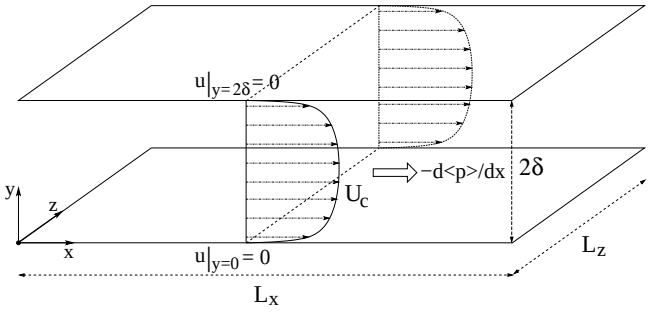

Figure 2.1: Channel flow geometry.

The mean flow is in the x direction, with the mean velocity varying in the wall-normal direction, y and it is also assumed that the flow is statistically stationary. In this case the mean continuity equation (2.25) deduces to $\frac{\mathrm{d}}{\mathrm{d}y}\langle v\rangle = 0$, which implies $\langle v\rangle = 0$ applying the no-slip condition at both walls. Thus, taking into account that the mean velocity field is $\langle \boldsymbol{u}\rangle = (\langle u(y)\rangle, 0, 0)$, the mean momentum equation (2.24), ignoring any external forces, yields

$$0 = -\frac{1}{\rho}\frac{\partial \langle p\rangle}{\partial x} - \frac{\mathrm{d}}{\mathrm{d}y}\langle uv\rangle + \nu\frac{\mathrm{d}^2\langle u\rangle}{\mathrm{d}y^2} \tag{2.34}$$

and

$$0 = -\frac{1}{\rho}\frac{\partial \langle p\rangle}{\partial y} - \frac{\mathrm{d}}{\mathrm{d}y}\left\langle v^2\right\rangle \tag{2.35}$$

where the Reynolds shear stress is essentially denoted as $\langle uv\rangle$ from here onwards, avoiding for convenience the primes that indicate fluctuating quantities.

Integration of Eq. (2.35) gives $p_w = \langle p\rangle + \rho\langle v^2\rangle$, where $p_w \equiv \langle p(x, 0, 0)\rangle$ and

$$\frac{\partial \langle p\rangle}{\partial x} = \frac{\mathrm{d}p_w}{\mathrm{d}x} \tag{2.36}$$

because $\langle v^2\rangle$ is independent of x, stating that the mean axial pressure gradient is

constant across the flow. Then, the axial mean-momentum equation becomes

$$\frac{\mathrm{d}\sigma_{12}}{\mathrm{d}y} = \frac{\mathrm{d}p_w}{\mathrm{d}x} = -\frac{\sigma_w}{\delta} \tag{2.37}$$

where the total shear stress is

$$\sigma_{12}(y) = \rho\nu\frac{\mathrm{d}\langle u\rangle}{\mathrm{d}y} - \rho\langle uv\rangle\,. \tag{2.38}$$

The balance of forces (2.37) is constant because σ_{12} is a function of y only and p_w, a function of x only, where $-\sigma_w/\delta$ is a positive constant that characterises the magnitude of the drop in pressure between the entrance and the exit of the channel that drives the mean flow. Moreover, integrating Eq. (2.37) with respect to y, it can be deduced that the total shear stress varies linearly with the distance from the wall

$$\sigma_{12}(y) = \sigma_w\left(1 - \frac{y}{\delta}\right) \tag{2.39}$$

with a fixed constant of integration, since the flow is symmetric about the $y = \delta$ plane. In this case, the wall shear stress is defined as the total shear stress at the wall

$$\sigma_w \equiv \sigma_{12}(0) = \rho\nu\frac{\mathrm{d}\langle u\rangle}{\mathrm{d}y} \tag{2.40}$$

where the Reynolds stress is zero satisfying the no-slip boundary condition. Note that the above analysis reveals that a flow in a channel or pipe can be defined by ρ, ν, δ and $\mathrm{d}p_w/\mathrm{d}x$ with the mean flow as unknown or imposing a $\langle u\rangle$ with the pressure gradient as unknown.

The important parameters in the near-wall region are the viscosity ν and the wall shear stress σ_w, which promote viscous characteristic scales such as the skin friction velocity $u_\tau \equiv \sqrt{\sigma_w/\rho}$ and the viscous length scale or wall unit $\delta_\nu \equiv \nu/u_\tau$. The Reynolds number that characterises the flow and is based on the viscous scales is called the friction Reynolds number and is defined by

$$\mathcal{R}e_\tau \equiv \frac{u_\tau\delta}{\nu} = \frac{\delta}{\delta_\nu}. \tag{2.41}$$

Now Eq. (2.39) can be rewritten as

$$\nu \frac{\mathrm{d}\langle u \rangle}{\mathrm{d}y} - \langle uv \rangle = u_\tau^2 \left(1 - \frac{y}{\delta}\right) \tag{2.42}$$

where $u_\tau^2 = -\frac{\delta}{\rho}\frac{\mathrm{d}p_w}{\mathrm{d}x}$ and in terms of the viscous scales it becomes

$$\frac{\mathrm{d}}{\mathrm{d}y_+} U_+ - \frac{\langle uv \rangle}{u_\tau^2} = 1 - \frac{y_+}{\mathcal{R}e_\tau} \tag{2.43}$$

where $U_+ \equiv \langle u \rangle / u_\tau$ and $y_+ \equiv y/\delta_\nu$, which is similar to a local Reynolds number and in principle its magnitude determines the relative importance of viscous and turbulent processes.

2.3.1 The mean velocity profile

The determination of the mean velocity profile proceeds with $\mathrm{d}\langle u \rangle / \mathrm{d}y$ rather than just with $\langle u \rangle$ since limiting similarity laws need to be constructed for the different regions in the flow, as will be shown. The mean velocity at any distance from the wall depends on the situation in the immediate vicinity of the wall, as opposed to the mean velocity gradient, prohibiting the limit of $y/\delta_\nu \to \infty$ (Barenblatt, 1996). This statement will become clearer as the analysis is pursued.

The mean velocity gradient can depend on u_τ, y and two similarity parameters in the following way

$$\frac{\mathrm{d}\langle u \rangle}{\mathrm{d}y} = \frac{u_\tau}{y} \Phi \left(\frac{y}{\delta_\nu}, \frac{y}{\delta}\right) \tag{2.44}$$

where Φ is a universal non-dimensional function, assuming complete similarity (Barenblatt, 1996), with δ_ν and δ the important length scales in the immediate vicinity of the wall and the channel centreline, respectively. The viscous scales dominate as the wall is approached (inner layer), so the asymptotic limit $y/\delta \to 0$ is true, whereas close to the centreline of the channel (outer layer) Φ becomes independent of ν and then $y/\delta_\nu \to \infty$ is valid. Therefore,

$$\Phi \left(\frac{y}{\delta_\nu}, \frac{y}{\delta}\right) = \begin{cases} \Phi_\mathrm{I} \left(\frac{y}{\delta_\nu}\right), & \text{for } y/\delta \to 0 \\ \Phi_\mathrm{O} \left(\frac{y}{\delta}\right), & \text{for } y/\delta_\nu \to \infty. \end{cases} \tag{2.45}$$

When $\mathcal{R}e_\tau \gg 1$ but $y/\delta_\nu \sim \mathcal{O}(1)$, Eq. (2.44) can be written for the inner layer as $\frac{\mathrm{d}}{\mathrm{d}y_+}U_+ = \frac{1}{y_+}\Phi_\mathrm{I}(y_+)$ and its integral leads to

$$U_+ = f_w(y_+) \tag{2.46}$$

where $f_w(y_+) = \int_0^{y_+} \frac{1}{r}\Phi_\mathrm{I}(r)\mathrm{d}r$. This is the *law of the wall*, which states that U_+ depends exclusively on y_+ for $y/\delta \to 0$, according to Prandtl's hypothesis (Prandtl, 1925). Under the above conditions the integral of Eq. (2.43) reduces to an exact relation by neglecting the Reynolds shear stress near the wall,

$$U_+ = y_+. \tag{2.47}$$

This region at the vicinity of the wall where the velocity profile is linear is called the *viscous sublayer*.

At high enough $\mathcal{R}e_\tau$ it should be possible to find an intermediate region $\delta_\nu \ll y \ll \delta$ between the inner and outer layer, if $y/\delta_\nu \propto \mathcal{R}e_\tau^\gamma$ and then $y/\delta \propto \mathcal{R}e_\tau^{\gamma-1}$ such that limits $y/\delta_\nu \to \infty$ and $y/\delta \to 0$ are satisfied simultaneously for $0 < \gamma < 1$ (Tennekes and Lumley, 1972). If this region exists, δ_ν is presumably too small to control the dynamics of the flow and δ is too large to be effective, so that the distance y is the only relevant length. In this case,

$$\frac{y}{u_\tau}\frac{\mathrm{d}\langle u\rangle}{\mathrm{d}y} = \Phi_\mathrm{I}\left(\frac{y}{\delta_\nu}\right) = \Phi_\mathrm{O}\left(\frac{y}{\delta}\right) = \frac{1}{\kappa} \tag{2.48}$$

where κ is the so called von Kármán[§] constant, usually taking the value $\kappa \simeq 0.41$ (Pope, 2000). Integration of Eq. (2.48) normalised with viscous scales gives the *logarithmic* or *von Kármán law* in the region $\delta_\nu \ll y \ll \delta$

$$U_+ = \frac{1}{\kappa}\ln y_+ + B \tag{2.49}$$

where $B \simeq 5.2$ is the intercept constant. Moreover, in this intermediate region,

[§]von Kármán (1930) was the first to derive the logarithmic velocity profile using similarity arguments.

combining Eqs. (2.48) and (2.42) yields

$$\frac{1}{\kappa y_+} - \frac{\langle uv \rangle}{u_\tau^2} = 1 - \frac{y}{\delta} \tag{2.50}$$

which implies

$$-\langle uv \rangle / u_\tau^2 \to 1 \tag{2.51}$$

as $y/\delta \to 0$ and $y/\delta_\nu \to \infty$. Consequently, the Reynolds stress is approximately constant in the region $\delta_\nu \ll y \ll \delta$, which is called either the *log-law region* or *inertial sublayer* because of the absence of local viscous effects, as it is clear from Eq. (2.50) for $y_+ \gg 1$. Deviations from Eq. (2.49) are small even close to the centreline of the channel. However, the above arguments leading to the log-law are not applicable in this so called core region. The law for the core region, called the *velocity-defect law* (Pope, 2000), can be derived by taking the limit $y/\delta_\nu \to \infty$ in Eq. (2.44) and integrating between y and δ.

An alternative argument for the mean velocity profile in the intermediate region $\delta_\nu \ll y \ll \delta$ at high enough Reynolds numbers has also been proposed (Barenblatt, 1996). Assuming incomplete similarity with respect to y/δ_ν, Eq. (2.44) reduces to

$$\frac{\mathrm{d}\langle u \rangle}{\mathrm{d}y} = \frac{u_\tau}{y} \left(\frac{y}{\delta_\nu} \right)^\alpha \Phi \left(\frac{y}{\delta} \right) \tag{2.52}$$

where Φ is non-universal and α is also assumed to depend on y/δ. Then, integration of Eq. (2.52) normalised with viscous scales gives the *power law* in the region $\delta_\nu \ll y \ll \delta$

$$U_+ = \Phi \left(\mathcal{R}e_\tau \right) y_+^{\alpha(\mathcal{R}e_\tau)} \tag{2.53}$$

assuming, in agreement with experiments, that the constant of integration is zero (Barenblatt, 1996).

Note that the mean flow profile of turbulent boundary layers is very widely taken to incorporate the extensive log-law region Eq. (2.49) for a very broad range of turbulent wall-bounded flows. However, renewed interest and new measurements over the past ten to fifteen years have led to debates (*i*) on the form of the mean velocity profile, i.e. log-law or power-law with very weak power exponent, (*ii*) on its scalings with Reynolds number and (*iii*) on its dependence or independence on overall flow geometry (McKeon, 2007). Fittings of new mean flow data with a log-law

lead to a variety of values for the von Kármán constant κ. The classically accepted $\kappa \simeq 0.41$ value (Pope, 2000) has been replaced with as low as $1/e$ [¶] for channel flows (Zanoun et al., 2003), as high as 0.43 for pipe flows (Zagarola and Smits, 1998), which was corrected afterwards to 0.42 (McKeon et al., 2004) and $\kappa \simeq 0.38$ for zero-pressure-gradient boundary layer flows (Nagib and Chauhan, 2008). In view of this non-universality, the von Kármán constant is renamed the von Kármán coefficient (Nagib and Chauhan, 2008). These issues are discussed in detail in chapter 3.

2.3.2 Analogies between homogeneous and wall-bounded turbulence

The spectral structure of homogeneous turbulence is in close analogy to the spatial structure of wall-bounded shear flows. The phenomenology of Richardson's turbulent cascade for homogeneous, isotropic turbulence (HIT) in view of Kolmogorov's 1941 theory (Frisch, 1995), based on scaling and similarity arguments, indicates three different range of scales for $\mathcal{R}e \gg 1$. These are:

- the *energy containing range* where the forcing injects energy to the large scales and the spectral dynamics are independent of viscosity, just like the dynamics in the core region of a turbulent channel flow.

- The *inertial range* where the time scale required for the energy transfer from an eddy of size ℓ is much shorter than the time to dissipate energy contained in the same eddy due to viscous diffusion, basically $\tau_\ell \ll \tau_\ell^{diff}$. Therefore, the energy is transferred to smaller scales in this range. The similarity hypothesis governing the link between large and small scale description leads to the closely related concepts of inertial range in homogeneous turbulence and inertial sublayer of wall-bounded shear flows. The logarithmic velocity profile in the inertial sublayer is one of the major landmarks in wall-bounded turbulence theory, as the 2/3 law of Kolmogorov (Kolmogorov, 1941; Batchelor, 1982; Frisch, 1995) in the inertial range of HIT.

- The *dissipation range* where viscous effects dominate and energy dissipation overcomes the transfer stopping the cascade of the turbulent spectrum, much

[¶] e denotes here the irrational number 2.71828, which is defined as $e = \lim_{n\to\infty} \left(1 + \frac{1}{n}\right)^n$

like viscosity prevails the viscous sublayer of wall-bounded turbulence inducing a drain for momentum.

In the inertial range of a statistically steady state homogeneous turbulent flow as $\mathcal{R}e \to \infty$, the energy flux $\Pi(\ell)$ is constant and is roughly equal to the energy dissipation rate ε, viz.

$$\varepsilon \simeq \Pi(\ell) \propto \frac{E(\ell)}{\tau_\ell} \propto \frac{u_\ell^3}{\ell} \tag{2.54}$$

where the eddy turnover time based on dimensional analysis is $\tau_\ell \propto \ell/u_\ell$, which is the time required to transfer energy from an eddy of size ℓ and rms velocity fluctuation u_ℓ to smaller eddies. So now, the Kolmogorov scaling in the inertial range can be determined for the characteristic velocity and time scale

$$u_\ell \propto \varepsilon^{1/3}\ell^{1/3} \tag{2.55}$$

$$\tau_\ell \propto \varepsilon^{-1/3}\ell^{2/3}. \tag{2.56}$$

The inertial range extends down to scales comparable to the Taylor scale (Taylor, 1935; Batchelor, 1982)

$$\lambda^2 \equiv \frac{\frac{1}{3}\left\langle|\boldsymbol{u}|^2\right\rangle}{\left\langle|\boldsymbol{\omega}|^2\right\rangle} = \frac{\nu}{3}\frac{2E}{\varepsilon} \propto \ell^2\mathcal{R}e^{-1} \tag{2.57}$$

where $\boldsymbol{u}$ and $\boldsymbol{\omega}$ are rms fluctuating quantities. At the bottom of the inertial range viscosity becomes relevant and the typical viscous diffusion time scale $\tau_\ell^{diff} \propto \ell^2/\nu$ is comparable to the eddy turnover time (2.56), so $\tau_\ell^{diff} \propto \tau_\ell$ implies

$$\eta \propto \left(\frac{\nu^3}{\varepsilon}\right)^{1/4} \propto \ell\mathcal{R}e^{-3/4} \tag{2.58}$$

where η is the Kolmogorov dissipation length scale. According to Frisch (1995), the range of scales comparable to or less than η is called the dissipation range. Here comes the shortcoming of phenomenology that does not predict numerical constants and also the fact that rigour in turbulence theory is far from achieved (Doering and Gibbon, 1995).

Similarly, in the inertial range of a turbulent channel flow for $\mathcal{R}e_\tau \to \infty$, the production of turbulent kinetic energy is mainly balanced by the rate of viscous

dissipation locally (Townsend, 1961), so Eq. (2.32) becomes

$$\varepsilon \simeq \mathcal{P} = -\langle uv \rangle \frac{\mathrm{d}\langle u \rangle}{\mathrm{d}y} \propto \frac{u_\tau^3}{y} \tag{2.59}$$

since $-\langle uv \rangle \simeq u_\tau^2$ and $\frac{\mathrm{d}}{\mathrm{d}y}\langle u \rangle \propto u_\tau / y$. Thus, in this context, the Kolmogorov microscale will be a function of the distance y from the wall according to

$$\eta(y) \propto \left(\frac{\nu^3}{\varepsilon}\right)^{1/4} \propto \delta_\nu^{3/4} y^{1/4} \tag{2.60}$$

using Eq. (2.59) and the fact that $\delta_\nu = \nu / u_\tau$. Therefore, $\eta(y) \geq \delta_\nu$, in fact Pope (2000) finds that $\eta(0) \simeq 1.5\delta_\nu$ based on DNS computations.

2.4 Structure and topology of fluid flow

Even though turbulence consists of a multitude of eddies of many different sizes, there have been works since early 1960s showing that the transport properties of most turbulent shear flows are dominated by mainly large scale organised vortex motions with varying shape and strength depending on flow geometry and history. Such organised vortex motions are called coherent structures. Their notion was first articulated by Liepmann (1952). Since then, several studies (Cantwell, 1981; Robinson, 1991) carried out trying to identify the structure of turbulence with the aim of explaining important physical mechanisms and relate it with statistical quantities and their scaling properties.

Townsend (1976) studied thoroughly the structure of turbulent shear flows through statistical methods. He proposed an *attached eddy* hypothesis for boundary layer coherent motions, which is a conceptual model of a double-cone roller eddy that gave fairly accurate reproduction of two-point correlation functions and turbulence intensity profiles. In particular, he considered velocity fluctuations, originating from the remote, core eddies, which make little contribution to the Reynolds stresses but the slow sweeping of these so called *inactive motions* emerges as a random modulation of the mean flow (Townsend, 1961; Bradshaw, 1967). This have interesting consequences, such as casting doubt over the assumed universality of the von Kármán's constant but also that $E \equiv \frac{1}{2}\langle |\boldsymbol{u}'|^2 \rangle$ does not scale with u_τ^2 in the limit of $\mathcal{R}e_\tau \to \infty$.

A reason is that velocity fluctuations from inactive motions will influence turbulent kinetic energy, which will then depend on the channel half-width δ (Davidson, 2004).

Moreover, Perry and Chong (1982); Perry et al. (1986) inspired by Townsend's attached eddy hypothesis and the flow visualisations of Head and Bandyopadhyay (1981), they represented a turbulent boundary layer by a geometrical hierarchy of Λ-shaped vortices. Using the Biot-Savart law (Saffman, 1995) in conjunction with this hierarchy of such vortices, they were able to faithfully reproduce the mean velocity profile, Reynolds shear stress, velocity fluctuations and spectra, supporting the idea of hairpin vortices as the dynamically dominant boundary layer structure. A refinement to their model for better quantitative agreement with the Reynolds stresses included two basic types of eddy structure geometries interpreted as 'wall' and 'wake structures' (Perry and Marusic, 1995).

One of the major problems in turbulence research is unambiguously defining the multiscale structure of the flow. Flow visualisations by Kline et al. (1967) remain the primary motivation for much of the work on structure of wall-bounded turbulence being carried on today. Coherent structures have been mainly identified through visualisations of turbulent flows. Such an approach is subjective, inevitably leading to controversy over the nature and significance of the structures (Tsinober, 2002). Several alternative eduction techniques have been proposed over the years, like the Karhunen-Loéve decomposition (Holmes et al., 1998) and many more vortex identification criteria (Chakraborty et al., 2005; Pope, 2000). Even with the aid of sophisticated statistical techniques it is difficult of making sense of structures in three-dimensional stochastic fields. An approach, however, that provides a well-defined and unambiguous language to describe eddying motions and flow patterns is the framework of critical point concepts from bifurcation theory (Glendinning, 1994; Ottino, 1989), which was studied extensively by Perry and Chong (1987) and it is briefly outlined in the next section.

2.4.1 Critical point concepts

The analysis of the topology of a flow serves to provide an understanding of the critical points, which are the salient features of a flow pattern. Critical or stagnation

points are defined as points where the streamline slope is indeterminate and

$$\boldsymbol{u}(\boldsymbol{x}, t) \equiv 0 \tag{2.61}$$

relative to a frame of reference. Quite often the qualitative features of the flow can be almost completely described once the critical points of the flow field have been identified and classified. The velocity field can be expanded in a Taylor series about the critical point and the result can be used to gain valuable information about the local flow geometry (Perry and Chong, 1987; Oertel, 2004). Asymptotically exact solutions of the Navier-Stokes and continuity equations can be derived close to the critical points and these give a number of standard flow patterns presented in the figures below for two and three dimensional flows.

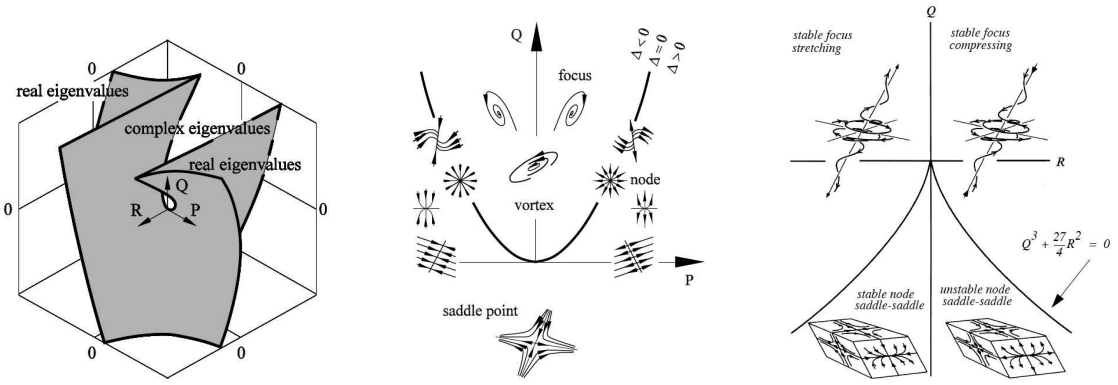

(a) Real and complex eigenvalues of $\boldsymbol{\nabla u}$

(b) 2D flows - eigenvectors of the critical points for R = 0

(c) 3D incompressible flows - eigenvectors of the critical points for P = 0

Figure 2.2: PQR classification of critical points. Courtesy Oertel (2004).

The classification of critical points for a given flow field can be obtained by calculating the eigenvalues λ_i of the velocity gradient tensor, i.e.

$$\det[\boldsymbol{\nabla u} - \lambda_i \boldsymbol{I}] = 0 \Rightarrow \lambda_i^3 + P\lambda_i^2 + Q\lambda_i + R = 0 \tag{2.62}$$

where the invariants of $\boldsymbol{\nabla u}$ are

$$\begin{aligned} P &= -tr(\boldsymbol{\nabla u}) = -(\lambda_1 + \lambda_2 + \lambda_3) \\ Q &= \frac{1}{2}[P^2 - tr((\boldsymbol{\nabla u})^2)] = \lambda_1\lambda_2 + \lambda_2\lambda_3 + \lambda_3\lambda_1 \\ R &= -\det(\boldsymbol{\nabla u}) = -\lambda_1\lambda_2\lambda_3. \end{aligned} \tag{2.63}$$

The value of the discriminant

$$\Delta = 27R^2 + (4P^2 - 18Q)PR + (4Q - P^2)Q^2 \tag{2.64}$$

provides a general classification initially for the solutions of the cubic equation (2.62) (see Fig. 2.2). For two-dimensional flows there are only two invariants of the velocity gradient tensor, so $R = 0$ from definition and if the velocity vector field is solenoidal then $P = 0$ for either dimension. The flow patterns consist of nodes, saddles, foci and combinations thereof depending on the eigenvalues of $\boldsymbol{\nabla u}$ with some degenerate special cases, such as vortices, sources and sinks.

Dávila and Vassilicos (2003) take the critical point concepts further by introducing statistics of stagnation points. They noted that each component of the velocity vector field $\boldsymbol{u}(\boldsymbol{x}, t)$ has an instantaneous zero-crossing surface in d-dimensions. The intersections of these zero-crossing surfaces are of course the points where $\boldsymbol{u}(\boldsymbol{x}, t) = 0$. However, the streamlines and stagnation points are frame dependent. It is crucial to identify the appropriate frame where stagnation points and their statistics are Galilean invariant so that they can be related to statistical observables of a turbulent flow. This frame of reference is $\langle \boldsymbol{u} \rangle = 0$. Therefore, stagnation points can be defined in the right frame in the following statistical sense

$$\boldsymbol{u}'(\boldsymbol{x}, t) \equiv \boldsymbol{u}(\boldsymbol{x}, t) - \langle \boldsymbol{u} \rangle = 0 \tag{2.65}$$

where the fluctuating velocity field preserves its Galilean invariance unlike in the above definition Eq. (2.61). Moreover, these d number of surfaces may have a fractal dimension (Dávila and Vassilicos, 2003; Ruelle, 1992), which can be estimated, based on the rule of thumb of fractal geometry that the co-dimension of intersections of surfaces is the sum of the co-dimensions of the intersecting surfaces (Falconer, 1990),

viz.

$$d - D_s = d(d - D) \Rightarrow D_s \equiv d[D - (d - 1)] \tag{2.66}$$

where D_s is the fractal dimension of the set of stagnation points and D is the fractal dimension of each zero-crossing surface of the individual component of the fluctuating velocity vector field, viz. $u'(\boldsymbol{x}, t) = v'(\boldsymbol{x}, t) = w'(\boldsymbol{x}, t) = 0$, which can be the same for each surface only under the assumption of isotropy. Then, one can determine the $\boldsymbol{u}'(\boldsymbol{x}, t) = 0$ points in an instantaneous turbulent velocity field and further obtain their multiscale spatial distribution (Dávila and Vassilicos, 2003).

This framework of multiscale flow topology using stagnation points has been applied in HIT indicating that it is possible to find relations between bulk flow statistics and the underlying topology of the fluctuating velocity field. In particular, Goto and Vassilicos (2009) related the dissipation constant $C_\varepsilon = \varepsilon\ell/u_\ell^3$ to the number density of stagnation points and were able to take into account the non-universality of C_ε by their formula. Stagnation points have also proved useful for understanding particle pair diffusion in two-dimensional turbulence (Goto and Vassilicos, 2004; Salazar and Collins, 2009). In the next chapter, this framework is developed for wall-bounded turbulence that advances a new picture by relating key statistical quantities, such as the mean flow profile, to the structure of stagnation points in turbulent channel flow.

Chapter 3

Stagnation point structure and mean flow profile of turbulent channel flow

This chapter presents a phenomenology based on the underlying topology of the fluctuating velocity field that relates the mean flow profile and the dissipation rate of kinetic energy to the multiscale structure of stagnation points of the velocity fluctuations in flavour of section 2.4. This novel approach is validated with the aid of DNS of various fully developed incompressible turbulent channel flows and proposes a resulting new starting point for a new intermediate asymptotic analysis of the mean flow profile of turbulent channel/pipe flows. The chapter is organised as follows. Section 3.1 describes the DNS of turbulent channel flows performed for this study and section 3.2 presents some of the conventional statistics which are obtained from these computations. Section 3.3 introduces the stagnation point approach and its application to turbulent channel flows. Sections 3.4 and 3.5 expound the phenomenology and the mean flow properties implied by the results, which were obtained from the application of this approach to DNS considered in this study. Finally, some analysis of the highest Reynolds number DNS channel flow data (Hoyas and Jiménez, 2006) currently available is presented in section 3.6 before summarising in section 3.7.

3.1 DNS of turbulent channel flow

Consider the following dimensionless variables, which are based on the channel half-width δ, the fluid density ρ and the centreline velocity of a fully developed laminar Poiseuille flow $U_c \equiv \frac{3}{2}U_b$, where $U_b \equiv \frac{1}{\delta}\int_0^\delta \langle u \rangle \, \mathrm{d}y$ is the bulk velocity of the flow

$$\frac{\boldsymbol{x}}{\delta} \rightarrow \boldsymbol{x}, \quad \frac{tU_c}{\delta} \rightarrow t, \quad \frac{\boldsymbol{u}}{U_c} \rightarrow \boldsymbol{u}, \quad \frac{p}{\rho U_c^2} \rightarrow p. \tag{3.1}$$

Then the non-dimensional incompressible Navier-Stokes equations in Cartesian co-ordinates are given by

$$\begin{gathered} \boldsymbol{\nabla} \cdot \boldsymbol{u} = 0 \\ \partial_t \boldsymbol{u} + \frac{1}{2}\left[\boldsymbol{\nabla}(\boldsymbol{u} \otimes \boldsymbol{u}) + (\boldsymbol{u} \cdot \boldsymbol{\nabla})\boldsymbol{u}\right] = -\boldsymbol{\nabla} p + \frac{1}{\mathcal{R}e_c}\boldsymbol{\Delta}\boldsymbol{u} \end{gathered} \tag{3.2}$$

where $\otimes$ is the tensor or Kronecker product and $\mathcal{R}e_c \equiv U_c\delta/\nu$ is the Reynolds number based on the centreline velocity and the channel's half-width.

In this study, the code of Laizet and Lamballais (2009) is employed where Eq. (3.2) are numerically integrated with a fractional step method using a three-stage third-order Runge-Kutta scheme and spatial derivatives are estimated using sixth-order compact finite-difference schemes. The fractional step method projects the velocity vector field to a solenoidal velocity field solving the Poisson pressure equation in Fourier space with a staggered grid for the pressure field (Laizet and Lamballais, 2009; Wilhelmson and Ericksen, 1977). The staggered grid for the pressure was used for numerical stability purposes and the skew-symmetric form of the nonlinear term in the Navier-Stokes equations (3.2) was implemented to allow reduction of aliasing errors while remaining energy conserving for the particular spatial discretisation (Kravchenko and Moin, 1997). A grid stretching technique maps an equally spaced co-ordinate in the computational space to a non-equally spaced co-ordinate in the physical space, in order to be able to use Fourier transforms in the inhomogeneous wall-normal direction (Cain et al., 1984; Avital et al., 2000). Further details on the numerical aspects of the code are provided in appendix A.

Incompressible channel flow turbulence was simulated in a rectangular box (see Fig. 2.1) with periodic boundary conditions for $\boldsymbol{u} \equiv (u, v, w)$ in the x and z homogeneous directions, and either no-slip boundary conditions at the walls Eq. (2.33)

or borrowed from studies of flow control schemes aimed at drag reduction (Xu et al., 2007; Min et al., 2006) (see below). The mean flow is in the x direction, i.e. $\langle \boldsymbol{u} \rangle = (\langle u(y) \rangle, 0, 0)$, where in this study the angle brackets denote averages in time and space (x and z directions)

$$\langle\ \rangle \equiv \lim_{T\to\infty} \lim_{L_x\to\infty} \lim_{L_z\to\infty} \frac{1}{TL_xL_z} \int_0^T \int_0^{L_x} \int_0^{L_z} \mathrm{d}z\mathrm{d}x\mathrm{d}t \tag{3.3}$$

except when, in section 3.3 stagnation points of $\boldsymbol{u}' = \boldsymbol{u} - \langle \boldsymbol{u} \rangle = 0$ are sought, in which case the average $\langle \boldsymbol{u} \rangle$ is only over space. The bulk velocity U_b in the x direction was kept at the same constant value at all times by adjusting the mean pressure gradient $-\mathrm{d}\langle p \rangle / \mathrm{d}x$ at each time step. The choice of U_b is made in accordance with Dean's formula $\mathcal{R}e_\tau \simeq 0.119\mathcal{R}e_c^{7/8}$ (Dean, 1978; Lesieur, 1997) for a given choice of $\mathcal{R}e_\tau$.

Different near-wall forcings and boundary conditions were applied at the walls so as to demonstrate how the stagnation point approach accounts for the way that different wall actuations modify the mean flow profile. Specifically, the following three control schemes were considered:

(*i*) $\boldsymbol{u} = \boldsymbol{0}$ at the walls with forcing $\boldsymbol{f}(y) = (-A\sin(2\pi y/\Lambda)H(\Lambda - y), 0, 0)$ near the $y = 0$ wall and similar forcing near the $y = 2\delta$ wall (Xu et al., 2007) where H is the Heaviside function, $A = 0.16U_c^2/\delta \simeq u_\tau^2/\delta_\nu$ and $\Lambda = 11\delta_\nu$ (case A1 in Table 3.1). The forcings are applied to the Navier-Stokes momentum equations (3.2). This scheme corresponds to a steady wall-parallel forcing localised within eleven wall units from the walls and uniform in the direction parallel to them. This force field averages to zero if integrated across the channel; it decelerates the flow closest to the wall but accelerates it in the immediately adjacent thin region.

(*ii*) $\boldsymbol{u} = (0, a\cos(\alpha(x - ct)), 0)$ at the wall (Min et al., 2006) with $a/U_c = 0.05$, $\alpha/\delta = 0.5$ and $c = -2U_c$ (case A2 in Table 3.1). This boundary condition corresponds to a blowing-suction travelling wave on the wall.

(*iii*) $\boldsymbol{u} = \boldsymbol{0}$ at the walls and $v(x, y_d, z, t)$ replaced by $-v(x, y_d, z, t)$ at all (x, z) points (Choi et al., 1994) on the planes $y_d = 10\delta_\nu$ and $y_d = 2\delta - 10\delta_\nu$ (case A3 in Table 3.1). This corresponds to a computational control scheme whereby the normal velocity at a distance y_d from the walls is made to change sign at every time step.

Table 3.1 provides the numerical parameters of the various cases performed, such as the number of grid points $N_x \times N_y \times N_z$ and the domain size $L_x \times L_y \times L_z$, where subscripts here denote the three Cartesian co-ordinates (see Fig. 2.1). With

the exception of the highest Reynolds number DNS channel flow data (Hoyas and Jiménez, 2006) which is analysed towards the end of this chapter, the Reynolds numbers considered here range between low to moderate, though, of course, always large enough for the flow to be turbulent. The highest Reynolds number DNS data (Hoyas and Jiménez, 2006) in terms of $\mathcal{R}e_\tau$ correspond to $\mathcal{R}e_\tau \simeq 950$ and 2000. The Reynolds numbers of the DNS data created for this study range between $\mathcal{R}e_\tau \simeq 110$ and 400 (see Table 3.1). This is too low for a direct assessment of the log-law but appears to be sufficient for the new approach to turbulent mean flow profiles which is proposed here based on stagnation points of the fluctuating velocity field.

Case	**Forcing**	$\boldsymbol{\mathcal{R}e_c}$	$\boldsymbol{\mathcal{R}e_\tau}$	$\boldsymbol{L_x \times L_y \times L_z}$	$\boldsymbol{N_x \times N_y \times N_z}$
A	No	4250	179	$4\pi\delta \times 2\delta \times 4\pi\delta/3$	$200 \times 129 \times 200$
A1	Yes	4250	114.4	$4\pi\delta \times 2\delta \times 4\pi\delta/3$	$200 \times 129 \times 200$
A2	Yes	4250	222.3	$4\pi\delta \times 2\delta \times 4\pi\delta/3$	$200 \times 129 \times 200$
A3	Yes	4250	141.6	$4\pi\delta \times 2\delta \times 4\pi\delta/3$	$200 \times 129 \times 200$
B	No	2400	109.5	$4\pi\delta \times 2\delta \times 2\pi\delta$	$100 \times 65 \times 100$
C	No	10400	392.6	$2\pi\delta \times 2\delta \times \pi\delta$	$256 \times 257 \times 256$

Table 3.1: Parameters for the DNS of turbulent channel flow. The term "Forcing" refers to wall or near-wall actuations.

The following procedure was applied for the DNS of the various turbulent channel flows of Table 3.1. The initialisation for some of the computations consisted of a laminar Poiseuille velocity profile with white noise (Papoulis, 1991; Press et al., 1996) added to all the velocity components. For others, an interpolated turbulent field was used as initial condition for faster convergence to the fully developed state, when a turbulent flow field was available. In all cases, the computations were marched sufficiently far in time, while their statistics were monitored for successive time intervals until the flow became fully developed. After reaching a statistically steady state, statistics were collected for several decades of through-flow time scales L_x/U_b. All the non-forced computations were validated against previously published databases for the corresponding $\mathcal{R}e_\tau$ cases (Moser et al., 1999; Iwamoto et al., 2002; Hu et al., 2006). Moreover, a validation for turbulent channel flow of the particular code compared with spectral and second-order finite-difference schemes can be found in Laizet and Lamballais (2009). Note that the total shear stress balance Eq. (2.42) holds for all y in all cases except for the forced case A1 where it holds for $\Lambda < y < 2\delta - \Lambda$.

3.2 Conventional DNS results

When $\mathcal{R}e_\tau \gg 1$ one might expect an intermediate region $\delta_\nu \ll y \ll \delta$ where production balances dissipation locally (Townsend, 1961), i.e. $-\langle uv \rangle \frac{\mathrm{d}}{\mathrm{d}y} \langle u \rangle \simeq \varepsilon$. The idea of such an intermediate region is supported by the DNS results (see Fig. 3.1) which suggest that

$$B_2 \equiv \mathcal{P}/\varepsilon = -\langle uv \rangle \frac{\mathrm{d}}{\mathrm{d}y} \langle u \rangle / \varepsilon \tag{3.4}$$

tends to 1 as $\mathcal{R}e_\tau \to \infty$ in this intermediate region. The recent paper by Brouwers (2007) proves this asymptotic result by assuming, however, that the mean flow has a logarithmic shape in the intermediate region and using similarity theory. In particular, Brouwers' analytic result includes some relative error terms in the production and the dissipation of turbulent kinetic energy of $\mathcal{O}(y/\delta)$, which vanish as $\mathcal{R}e_\tau \to \infty$ (Brouwers, 2007). Moreover, this region where this approximate balance holds increases as $\mathcal{R}e_\tau$ increases. The slight discrepancy away from $B_2 \simeq 1$ at these moderate Reynolds numbers is well known and agrees with other previously published DNS results (Pope, 2000).

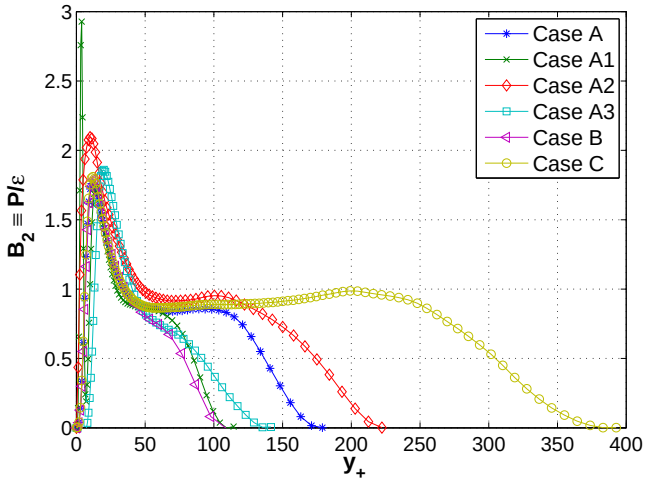

Figure 3.1: Profile of the production to dissipation ratio. Note the existence of an approximate equilibrium layer which grows with $\mathcal{R}e_\tau$ and where production approximately balances dissipation.

In this intermediate region, Eq. (2.42) implies $-\langle uv \rangle \simeq u_\tau^2$ as $y/\delta \to 0$ and $y/\delta_\nu \to \infty$, assuming that $\frac{\mathrm{d}}{\mathrm{d}\ln y_+} U_+$ does not increase faster than y_+^α with $\alpha \geq 1$ in

this limit. It then follows that in this intermediate equilibrium region,

$$\varepsilon \simeq \frac{u_\tau^3}{\kappa y} \text{ implies } \frac{\mathrm{d}\,\langle u\rangle}{\mathrm{d}y} \simeq \frac{u_\tau}{\kappa y} \tag{3.5}$$

as $\mathcal{R}e_\tau \gg 1$, where κ is the von Kármán coefficient (see also section 2.3). At finite Reynolds numbers the expression for the mean shear in Eq. (3.5) should be replaced by $\frac{\mathrm{d}\langle u\rangle}{\mathrm{d}y} \simeq \frac{B_2}{B_3}\frac{u_\tau}{\kappa y}$ where

$$B_3 \equiv \frac{-\langle uv\rangle}{u_\tau^2}. \tag{3.6}$$

Note that even though B_2 and B_3 may tend to 1 as $\mathcal{R}e_\tau \gg 1$, they are definitely different from 1 and even functions of y_+ and y/δ at finite values of $\mathcal{R}e_\tau$.

The mean flow profiles show clear impacts of the control schemes on the mean flow (see Fig. 3.2). For the various control schemes considered at the same $\mathcal{R}e_c = 4250$, the skin friction decreases as a result of both case A1 and A3 but increases when the control scheme A2 is applied (see Table 3.1). This observation agrees with Fig. 3.2 where mean flow values for cases A1 and A3 are higher than for case A (no control scheme), and mean flow values are lower for case A2 than for case A.

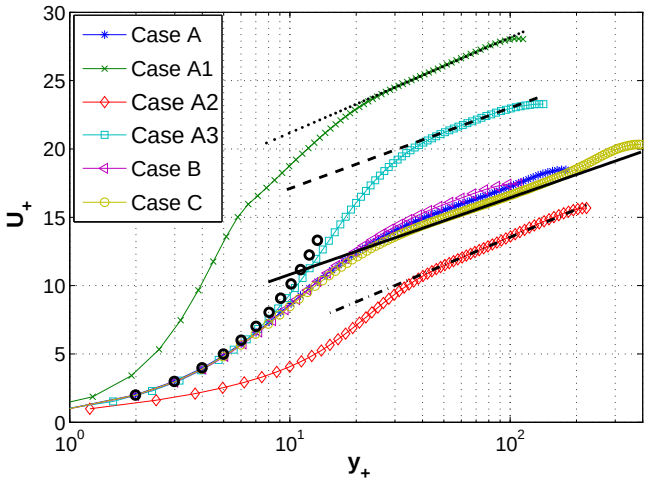

Figure 3.2: Mean velocity profiles. For comparison best log-law fits are also plotted. ○: $U_+ = y_+$, ⋯: $U_+ = \frac{1}{0.33}\log y_+ + 14.2$, −·− : $U_+ = \frac{1}{0.34}\log y_+ + 0.0$, - - -: $U_+ = \frac{1}{0.39}\log y_+ + 11.2$, ——: $U_+ = \frac{1}{0.41}\log y_+ + 5.2$.

With reference to the log-law scaling Eq. (2.49), which results from integration of Eq. (2.48) if $1/\kappa$ is independent of y, the coefficient $y\frac{\mathrm{d}}{\mathrm{d}y}U_+$ and $B \equiv U_+ -$

$\left(y\frac{\mathrm{d}}{\mathrm{d}y}U_+\right)\log y_+$ are plotted with respect to y_+ in Figs. 3.3 and 3.4, respectively, for all the six different DNS cases of Table 3.1. Note that $y\frac{\mathrm{d}}{\mathrm{d}y}U_+$ is usually referred to as $1/\kappa$ but is in fact $B_2/(B_3\kappa)$ in the present context where κ is defined by the dissipation expression in Eq. (3.5). It is only if B_2 and B_3 both equal 1 in the equilibrium layer, as may be the case when $\mathcal{R}e_\tau \gg 1$, that $\frac{\mathrm{d}}{\mathrm{d}y}\langle u\rangle \simeq \frac{B_2}{B_3}\frac{u_\tau}{\kappa y}$ yields $\frac{\mathrm{d}}{\mathrm{d}y}\langle u\rangle \simeq \frac{u_\tau}{\kappa y}$ and that $y\frac{\mathrm{d}}{\mathrm{d}y}U_+$ becomes $1/\kappa$ in the equilibrium layer.

The values of B are affected by the various control schemes (see Fig. 3.4) in a way consistent with the observations made two paragraphs earlier (higher values of B for cases A1 and A3 than for A and lower for case A2). However, it is hard to conclude on the validity of the log-law from these results and in particular from the plot in Fig. 3.3 which clearly shows a significant dependence on near-wall conditions, $\mathcal{R}e_\tau$ and y_+. It may be that the log-law is not valid at all or it may be that the log-law is not valid unless the Reynolds number is sufficiently high, definitely higher than the Reynolds numbers of the simulations considered in this study.

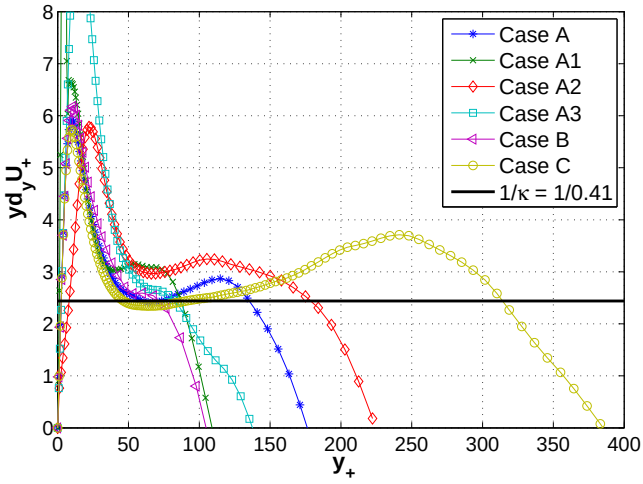

Figure 3.3: The inverse von Kármán coefficient $\equiv y\frac{\mathrm{d}}{\mathrm{d}y}U_+$ versus y_+. Taking the definition of κ to be given by the left-hand expression in Eq. (3.5) it is really $B_2/(B_3\kappa)$ which is plotted against y_+. The effects of the various near-wall actuations are significant.

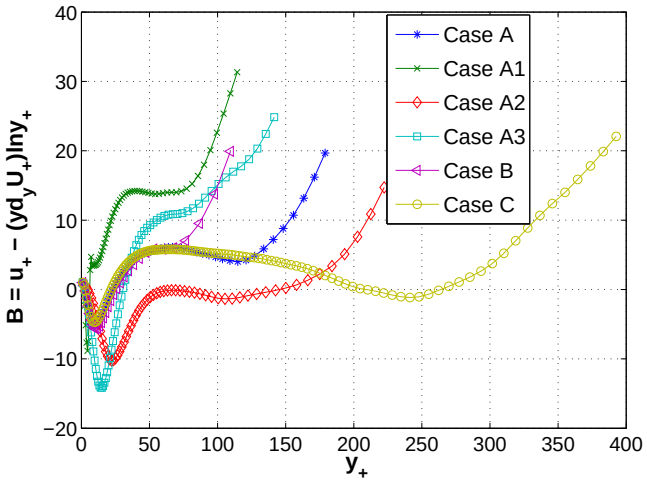

Figure 3.4: $B \equiv U_+ - \left(y\frac{\mathrm{d}}{\mathrm{d}y}U_+\right)\log y_+$ as function of y_+ for the six different DNS cases in Table 3.1.

3.3 The stagnation point approach

As this DNS study of the mean flow expression in Eq. (3.5) does not yield clear results, it is chosen instead to investigate the validity of the dissipation expression in Eq. (3.5). For this the stagnation point approach is employed (see section 2.4.1) which has shown recently how the number density of stagnation points in high Reynolds number homogeneous, isotropic turbulence (HIT) determines salient properties of turbulent pair diffusion (Goto and Vassilicos, 2004; Salazar and Collins, 2009) and kinetic energy dissipation rate per unit mass (Mazellier and Vassilicos, 2008; Goto and Vassilicos, 2009). In particular, a generalised Rice theorem was recently proved (Goto and Vassilicos, 2009) for high Reynolds number HIT which states that *the Taylor microscale is proportional to the average distance between neighboring stagnation points*. This average distance is defined as the $-1/d$ power of the number density of stagnation points which are points in the d-dimensional space of the flow where the turbulent fluctuating velocity is zero.

The generalised Rice theorem (Goto and Vassilicos, 2009) for high Reynolds number HIT holds under two main assumptions: (*i*) statistical independence between large and small scales and (*ii*) absence of small-scale intermittency Reynolds number effects. Note that there is no assumption of Gaussianity in the latter assumption. Instead it is assumed that the probability density functions (*pdf*) of the velocity com-

ponents and the velocity derivatives are independent of Reynolds number and can be scaled with u' and $\langle(\partial_x u')^2\rangle^{1/2}$, respectively. The *pdf* of velocity derivatives is also required to decay fast enough at infinity. Now, the question which arises in the context of the present work is whether this theorem also holds in some region of turbulent channel flows.

To obtain some insight into this question by DNS, stagnation points of the turbulent fluctuation velocity field are considered $\boldsymbol{u}' \equiv \boldsymbol{u} - \langle \boldsymbol{u} \rangle = 0$, i.e. points where all components of the velocity fluctuations around the local mean flow are zero. A three-dimensional plot of these points for an instant in time in the DNS channel is presented in Fig. 3.5 just for $0 \leq y_+ \leq \mathcal{R}e_\tau$ due to symmetry of the flow. A fourth-order Lagrangian interpolation and the Newton-Raphson method is used to locate these points. Details on how to find these points are provided in appendix B.

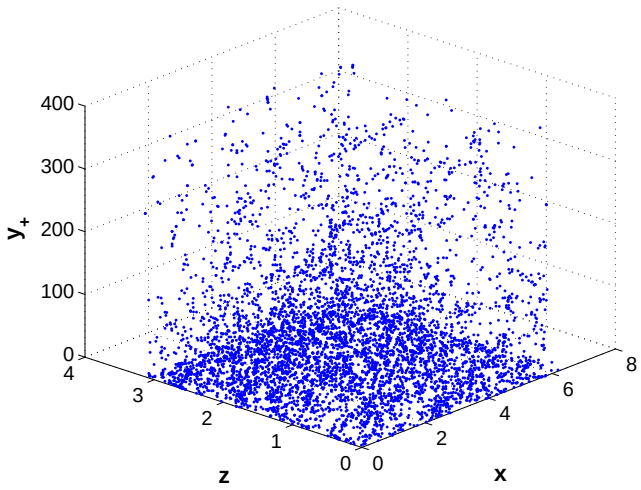

Figure 3.5: Points where $\boldsymbol{u}' \equiv \boldsymbol{u} - \langle \boldsymbol{u} \rangle = 0$ for case C at a given instant in time.

$N_s(y_+)$ is defined as the total number of these stagnation points in a thin slab parallel to and at a distance y from the channel's wall. The dimensions of this slab are $L_x \times \delta_y \times L_z$ with slab thickness $\delta_y \propto \delta_\nu$. The average distance between stagnation points at a height y from the wall is

$$\ell_s \equiv \sqrt{\frac{L_x L_z}{N_s}} \tag{3.7}$$

and a Taylor microscale $\lambda(y)$ can be defined as (see also section 2.3.2)

$$\lambda(y)^2 \equiv \frac{\nu}{3}\frac{2E(y)}{\varepsilon(y)} \tag{3.8}$$

where $E(y) = \frac{1}{2}\langle|\boldsymbol{u}'|^2\rangle$ and $\varepsilon(y) = 2\nu\langle s_{ij}s_{ij}\rangle$ with s_{ij} the fluctuating velocity's strain rate tensor. The question raised is whether a region of turbulent channel flow exists for $\mathcal{R}e_\tau \gg 1$ where

$$\lambda(y) = B_1\ell_s(y) \tag{3.9}$$

with B_1 independent of y and Reynolds number. The answer provided by DNS is that B_1 is indeed approximately constant over an intermediate range $\delta_\nu \ll y \lesssim \delta$, but not perfectly so, as the plots in Fig. 3.6 attest to. It is worth noting that this constancy of B_1 appears to be better defined for cases A, B and C where there is no wall or near-wall actuation (see Fig. 3.6b). Hence, a small discrepancy away from $B_1 = Const$ may be achieved as a result of those different wall-forcings (see Fig. 3.6c). However, part of the even smaller discrepancy in cases A, B and C might be accountable to neglected small-scale intermittency effects (Kolmogorov, 1962) which, in the case of high Reynolds number HIT, are known to manifest themselves as a weak Reynolds number dependence on B_1 (Mazellier and Vassilicos, 2008). In the case of wall-bounded turbulence, small-scale intermittency effects could therefore manifest themselves as a weak dependence of B_1 on local Reynolds number y_+. However, this refinement is not considered in this study.

Combining Eqs. (3.7)-(3.9), one can write

$$\varepsilon = \frac{\nu}{3}\frac{2E}{\lambda^2} = \frac{\nu}{3}\frac{2E}{B_1^2\ell_s^2} = \frac{\nu}{3}\frac{2E}{B_1^2L_xL_z}N_s = \frac{\nu}{3}\frac{2E}{B_1^2}\delta_\nu n_s \tag{3.10}$$

where the number density of stagnation points $n_s \equiv N_s/(L_xL_z\delta_\nu)$ was introduced. Combining this last equation with Eq. (3.4) and using $\frac{\mathrm{d}}{\mathrm{d}y}\langle u\rangle = \frac{u_\tau}{\kappa y}$ as well as $C \equiv -\frac{2E}{3\langle uv\rangle}$, then

$$n_s = \frac{C_s}{\delta_\nu^3}y_+^{-1} \tag{3.11}$$

where C_s is given by

$$C_s = \frac{B_1^2}{\kappa B_2 C}. \tag{3.12}$$

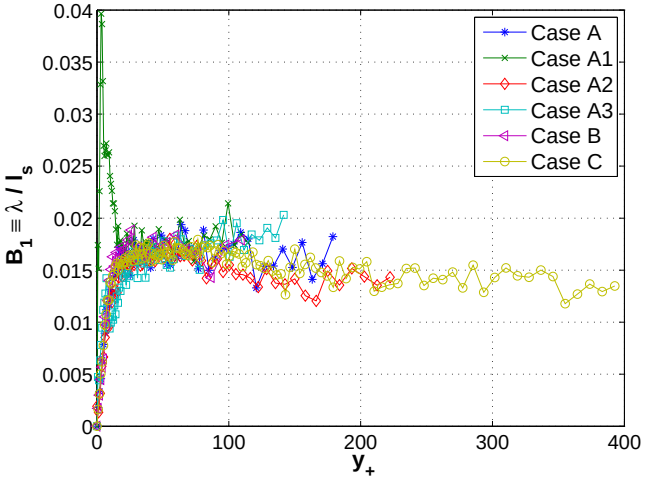

(a) B_1 as function of y_+

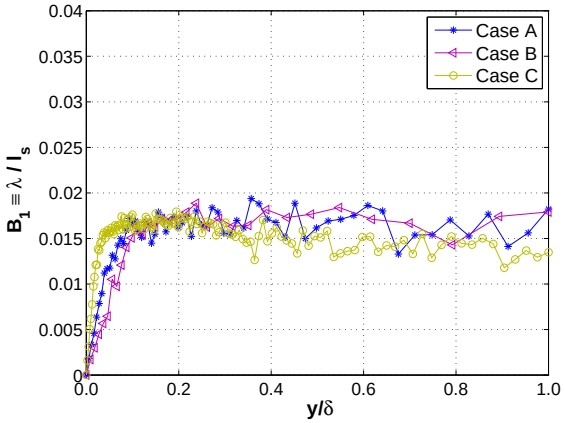

(b) B_1 as function of y/δ with no wall-forcings

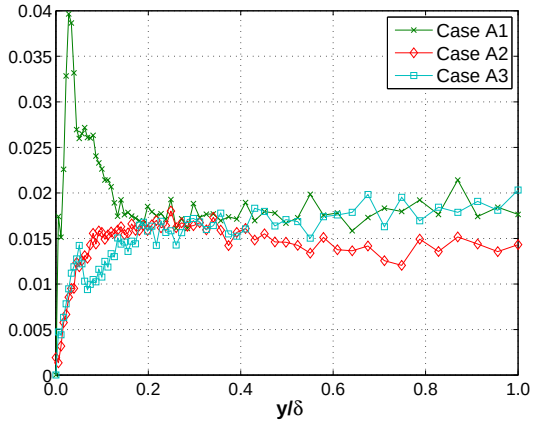

(c) B_1 as function of y/δ with wall-forcings

Figure 3.6: Support for the generalised Rice theorem as a meaningful approximation in turbulent channel flows with various Reynolds numbers and different wall actuations (see Table 3.1).

The classical claims (Pope, 2000) are that the empirical constants $\kappa \simeq 0.4$, $C \simeq 2$ and $B_2 \simeq 1$ in the intermediate range $1 \ll y_+ \ll \mathcal{R}e_\tau$ at high enough $\mathcal{R}e_\tau$. These claims therefore imply that C_s should also be a constant in that same range and limit provided B_1 is. Whilst, as it was shown, B_1 is not too far from being constant in the range $\delta_\nu \ll y \lesssim \delta$, κ and C are significantly far from constant in this range for the Reynolds numbers under consideration (see Fig. 3.3 and Fig. 3.7). Even so, the DNS evidence (see Fig. 3.8) suggests that C_s tends to a constant within $\delta_\nu \ll y \lesssim \delta$ as $\mathcal{R}e_\tau$ increases. Remarkably, this condition on $\mathcal{R}e_\tau$ for the constancies of C_s and B_1

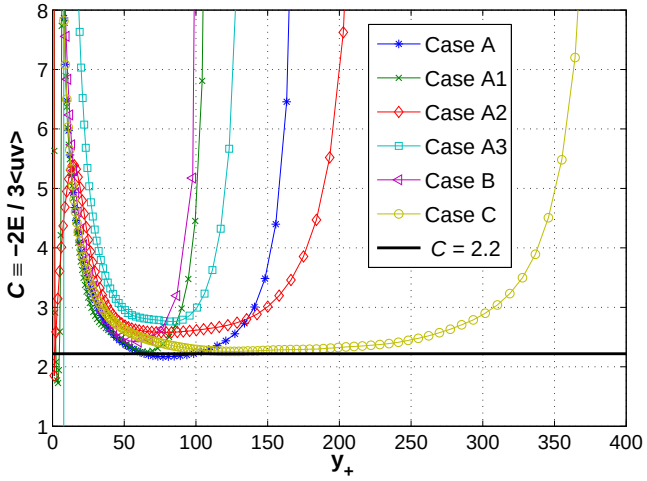

Figure 3.7: C with respect to y_+ for various Reynolds numbers and different wall-actuations (see Table 3.1).

seems to require as little as $\mathcal{R}e_\tau$ exceeding a few hundred. It is equally remarkable that the calculation of N_s, which underpins B_1 and C_s, has involved an average over a number of time-samples that is two orders of magnitude smaller than for the time average required to statistically converge $\langle u \rangle$, $\langle uv \rangle$, E and ε.

The constancy of C_s in the range $\delta_\nu \ll y \lesssim \delta$ implies that the number density of stagnation points decreases with distance from the wall obeying the power-law $n_s \propto y_+^{-1}$ in that range. This is in qualitative agreement with Fig. 3.5 which shows the stagnation points to be increasingly dense as the wall is approached. It should be noted that this power-law appears to be better defined for cases A, B and C where there is no wall or near-wall actuation (see Fig. 3.8b). On the other hand, the different wall-forcings modify the stagnation point structure of the flow and this is manifested as a discrepancy away from $C_s = Const$ (see Fig. 3.8c).

The constant C_s can be interpreted as representing the number of turbulent velocity stagnation points within a cube of side-length equal to a few multiples of δ_ν (see Eq. (3.11)) placed where y equals a few multiples of $10\delta_\nu$ as seen in Fig. (3.8a). This is the lower end of the range where the -1 power-law is valid, i.e. $n_s \propto y_+^{-1}$, and seems to be where the upper edge of the buffer layer is usually claimed to lie (Pope, 2000).

Equation (3.11) and consequently Eq. (3.12) have been derived by assuming well-defined constant values of κ, B_2, C and B_1. However, the DNS results show that, at

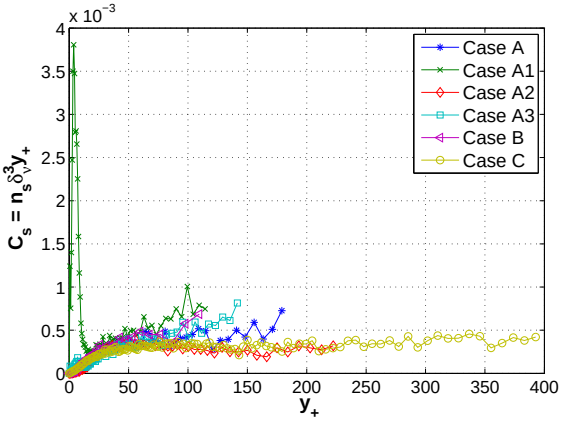

(a) C_s as function of y_+

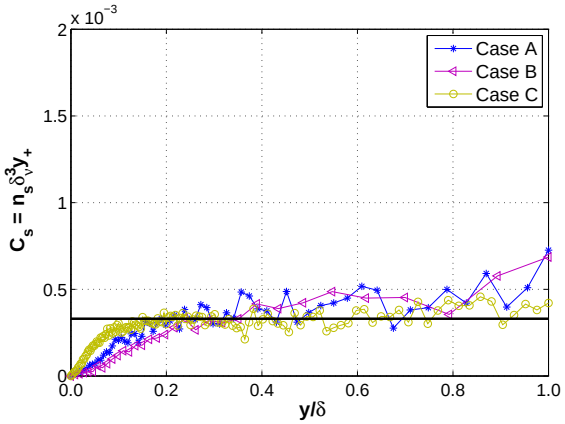

(b) C_s as function of y/δ with no wall-forcings

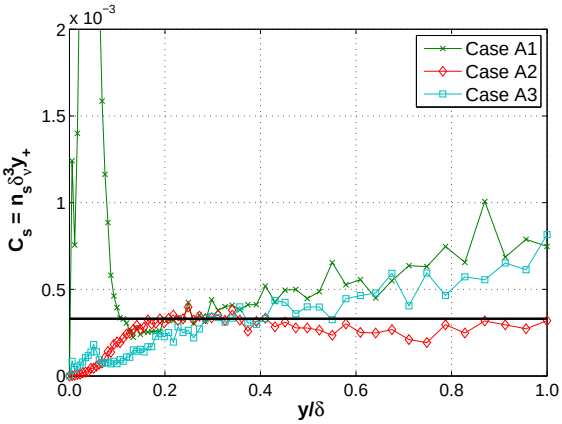

(c) C_s as function of y/δ with wall-forcings

Figure 3.8: Normalised number of turbulent velocity stagnation points for various Reynolds numbers and different wall-actuations (see Table 3.1).

the Reynolds numbers considered, B_1 and C_s are indeed constant but κ, B_2 and C are clearly not. Equations (3.9) and (3.11) with constant dimensionless values of B_1 and C_s seem to be more broadly valid than the assumptions under which Eq. (3.11) has been derived. Therefore, in the next section the phenomenology behind the new Eqs. (3.9) and (3.11) and the constant values of B_1 and C_s is explored in the range $\delta_\nu \ll y \lesssim \delta$. Moreover, section 3.5 goes one step further where the consequences of the constancies of B_1 and C_s on the mean flow profile are derived without assuming well-defined constant values of κ, B_2 and C.

3.4 Phenomenology

One interpretation of the constancy of B_1 can be obtained by considering the eddy turnover time τ which is defined by $\tau \equiv E/\varepsilon$ (see also section 2.3.2). Combined with Eq. (3.8), one obtains $\tau = 3\lambda^2/2\nu$. Using Eq. (3.9), $B_1 = Const$ is then equivalent to

$$\tau \propto \frac{\ell_s^2}{\nu} \tag{3.13}$$

which indicates that in the equilibrium layer, the time it takes for viscous diffusion to spread over neighbouring stagnation points is the same proportion of the eddy turnover time at all locations and all Reynolds numbers. In high Reynolds number turbulence, the turnover time is also the time it takes for the energy to cascade to the smallest scales.

For an interpretation of the constancy of C_s note first that Eq. (3.11) and $\ell_s = \sqrt{\frac{L_x L_z}{N_s}} = (n_s \delta_\nu)^{-1/2}$ imply $\ell_s^2 = C_s^{-1} \delta_\nu y$. From Eqs. (3.8) and (3.9) it then follows that

$$\varepsilon = \frac{2}{3} \frac{E u_\tau}{\kappa_s y} \tag{3.14}$$

with

$$\kappa_s \equiv \frac{B_1^2}{C_s}. \tag{3.15}$$

The meaning of C_s and B_1 constant is therefore, using Eq. (3.14), that the eddy turnover time $\tau = E/\varepsilon$ is proportional to y/u_τ throughout the range where they are constant. The constant of proportionality is $3\kappa_s/2$ where κ_s is determined by the stagnation point coefficients B_1 and C_s and is constant if they are constant. κ_s is referred to as the stagnation point von Kármán coefficient.

Note that, in the present context, Eq. (3.14) replaces the usual $\varepsilon = u_\tau^3/\kappa y$ (Pope, 2000), and that these two equations reduce to the same one only if and where $E \propto u_\tau^2$ independently of y_+ and $\mathcal{R}e_\tau$.

3.5 The mean flow profile in the equilibrium layer

In this section the consequences of the constancies of B_1 and C_s on the mean flow profile are spelt out. In the equilibrium layer the expectation is that $B_2 \to 1$ in the limit $\mathcal{R}e_\tau \to \infty$. This means that $-\langle uv \rangle \frac{\mathrm{d}}{\mathrm{d}y} \langle u \rangle = B_2 \varepsilon$ may be replaced by

$-\langle uv\rangle \frac{\mathrm{d}}{\mathrm{d}y}\langle u\rangle \simeq \varepsilon$ in the equilibrium layer. The constancy of B_1 and C_s in this same limit implies a constant $\kappa_s = B_1^2/C_s$ in $\varepsilon = \frac{2}{3}E_+\frac{u_\tau^3}{\kappa_s y}$ where $E_+ \equiv E/u_\tau^2$. It then follows that $-\langle uv\rangle \frac{\mathrm{d}}{\mathrm{d}y}\langle u\rangle \simeq \varepsilon = \frac{2}{3}E_+\frac{u_\tau^3}{\kappa_s y}$. In turbulent channel/pipe flows where one can have some mathematical confidence that, as $\mathcal{R}e_\tau \to \infty$, $-\langle uv\rangle \to u_\tau^2$ in an intermediate layer $\delta_\nu \ll y \ll \delta$, it yields

$$\frac{\mathrm{d}\langle u\rangle}{\mathrm{d}y} \simeq \frac{2}{3}E_+\frac{u_\tau}{\kappa_s y} \tag{3.16}$$

in that same layer and limit. At finite Reynolds numbers this new equation (3.16) should be replaced by $\frac{\mathrm{d}}{\mathrm{d}y}\langle u\rangle \simeq \frac{2}{3}\frac{B_2}{B_3}E_+\frac{u_\tau}{\kappa_s y}$ and account should be taken of the fact that B_2, B_3 and κ_s all have their own, potentially different, rates of convergence towards their high Reynolds number asymptotic constant values.

An important step taken in deriving both Eqs. (3.5) and (3.16) has been the high Reynolds number local energy balance $\mathcal{P} \simeq \varepsilon$ in the equilibrium layer. In terms of the classical assumption $\varepsilon \simeq u_\tau^3/\kappa y$, Eq. (3.4) implies that $\mathcal{P}y/u_\tau^3 \simeq B_2/\kappa$ which should be constant in the equilibrium layer as a result of this local energy balance between production and dissipation of turbulent kinetic energy. On the other hand, the new Eq. (3.14) along with Eq. (3.4) gives $\frac{3}{2}\mathcal{P}y/(E_+u_\tau^3) \simeq B_2/\kappa_s$ which implies that B_2/κ_s should be constant in the equilibrium layer rather than B_2/κ due to the balance between $\mathcal{P}$ and ε. Notice that the main difference here is the presence of E in Eq. (3.14). DNS results for $\mathcal{P}y/u_\tau^3$ and $\frac{3}{2}\mathcal{P}y/(E_+u_\tau^3)$ are plotted against y_+ in Figs. 3.9a and 3.9b, respectively. It is clear that the collapse between the different Reynolds number and wall-actuation data is far worse and the y-dependence in the equilibrium layer far stronger for B_2/κ than for B_2/κ_s. These DNS results are for Reynolds numbers which are not very large; yet the high-Reynolds number constancy of B_2/κ_s in the equilibrium layer seems already not exceedingly far from being reached (see Fig. 3.9b) whereas no such indication is shown in the plot of B_2/κ (see Fig. 3.9a).

From Eq. (3.16), a direct plot of $\frac{3}{2}\frac{y}{E_+u_\tau}\frac{\mathrm{d}}{\mathrm{d}y}\langle u\rangle$ should give $1/\kappa_s$ in the equilibrium layer when $\mathcal{R}e_\tau \to \infty$ and $B_2/(B_3\kappa_s)$ in that layer at finite Reynolds numbers. Fig. 3.10 presents this plot for each of the cases in Table 3.1. Notice that $B_2/(B_3\kappa_s)$ does not compare favourably with the plots of $\frac{y}{u_\tau}\frac{\mathrm{d}}{\mathrm{d}y}\langle u\rangle$, effectively plots of $B_2/(B_3\kappa)$, in Fig. 3.3. However, this does not mean that in the limit $\mathcal{R}e_\tau \to \infty$, Eq. (3.5) is better than Eq. (3.16) in the equilibrium layer. The facts that C_s and B_1 are approximately

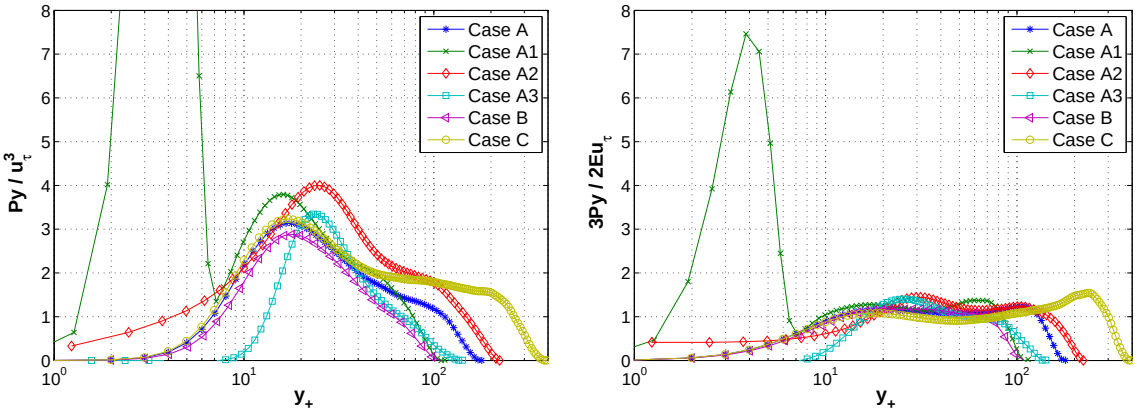

(a) $\mathcal{P}y/u_\tau^3$ versus y_+. This is the same as B_2/κ versus y_+ because of Eq. (3.5) and $\mathcal{P} = B_2\varepsilon$.

(b) $\frac{3}{2}\mathcal{P}y/(E_+u_\tau^3)$ versus y_+. This is the same as B_2/κ_s versus y_+ because of Eq. (3.14) and $\mathcal{P} = B_2\varepsilon$.

Figure 3.9: Linear-log plots of (a) B_2/κ and (b) B_2/κ_s as functions of y_+ for various Reynolds numbers and different wall-actuations (see Table 3.1).

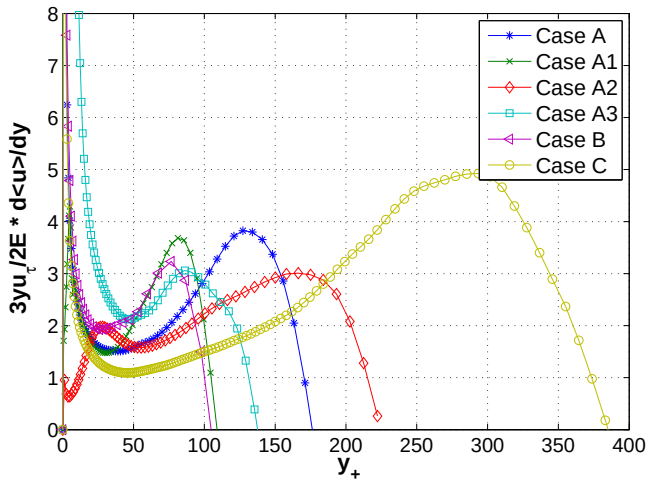

Figure 3.10: Plot $\frac{3}{2}\frac{y}{E_+u_\tau}\frac{\mathrm{d}}{\mathrm{d}y}\langle u\rangle$ with respect to y_+ for various Reynolds numbers and different wall actuations (see Table 3.1). This is effectively plot of $B_2/(B_3\kappa_s)$ to be compared with the similarly plotted $B_2/(B_3\kappa)$ in Fig. 3.3.

constant in the range $\delta_\nu \ll y \lesssim \delta$ and that B_2/κ is much less collapsed and less constant along y than B_2/κ_s at Reynolds numbers of Table 3.1 (compare either Fig. 3.9a with Fig. 3.9b or Fig. 3.11a with Fig. 3.11b. Fig. 3.11 are just linear-linear replots of Fig. 3.9 for easier comparison with Fig. 3.3.) suggest that the strong y and $\mathcal{R}e_\tau$ dependencies of B_3 partly cancel those of B_2/κ at those Reynolds numbers. As

the Reynolds number is increased to the point where B_3 reaches its asymptotic value 1 then this cancellation will either disappear if B_2/κ does not tend to a constant or will remain if it does. In the specific context of the present stagnation point approach, the choice between these two scenarios will depend on the high-Reynolds number scalings of the kinetic energy E.

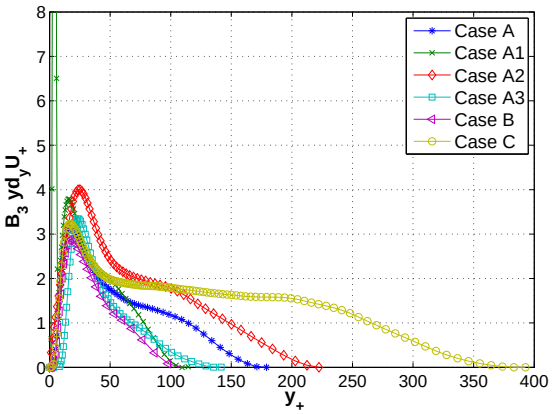

(a) $B_3 \frac{y}{u_\tau} \frac{\mathrm{d}}{\mathrm{d}y} \langle u \rangle$ versus y_+. Essentially a linear-linear replot of Fig. 3.9a

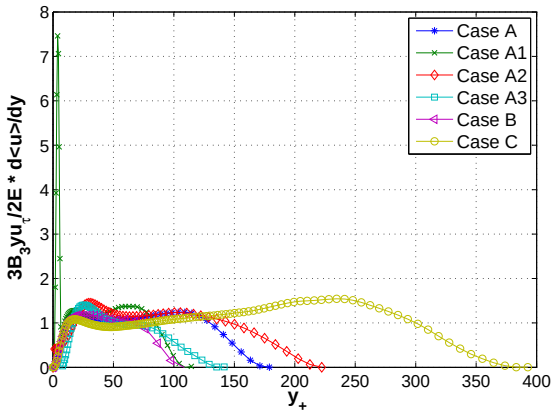

(b) $\frac{3}{2} B_3 \frac{y}{E_+ u_\tau} \frac{\mathrm{d}}{\mathrm{d}y} \langle u \rangle$ versus y_+. Essentially a linear-linear replot of Fig. 3.9b.

Figure 3.11: Linear-linear plots of compensated (a) B_2/κ and (b) B_2/κ_s as functions of y_+ for various Reynolds numbers and different wall-actuations (see Table 3.1).

According to classical similarity scalings, as $\mathcal{R}e_\tau \to \infty$, $E \propto u_\tau^2$ independently of y, δ and ν in the equilibrium range $\delta_\nu \ll y \ll \delta$. If this is true, then Eq. (3.5) and the log-law are recovered from Eqs. (3.14) and (3.16) with a von Kármán coefficient $\kappa \propto \kappa_s$. This discussion naturally leads to the non-universality of measured von Kármán coefficients (Nagib and Chauhan, 2008), which is now commented on before moving to the analysis of some of the highest Reynolds number DNS data currently available. So, if $E \propto u_\tau^2$ at high Reynolds numbers and the log-law holds as a consequence of Eq. (3.16), then, because of Eq. (3.15), the von Kármán coefficient will have to be proportional to B_1^2 and inversely proportional to C_s, the number of stagnation points within a volume δ_ν^3 at the upper edge of the buffer layer. There is no *a priori* reason to expect B_1 and C_s to be the same in turbulent channel and pipe flows, for example. Hence, there is no *a priori* reason for the von Kármán coefficient to be the same in different such flows either.

On the other hand, Townsend's idea of inactive motions (see section 2.4 and Bradshaw (1967)) would suggest that E does not scale as u_τ^2 in the equilibrium layer

when $\mathcal{R}e_\tau \to \infty$. Then, Eq. (3.16) does not yield Eq. (3.5) and $B_2/(B_3\kappa)$ does not tend to a constant in the high Reynolds number limit. Therefore, in the case where the log-law does not hold because of the effect that inactive motions have on E_+ in Eq. (3.16), data fitted by a log-law may yield different von Kármán coefficients both as a result of $\kappa_s = B_1^2/C_s$ but also as a result of fitting mismatches.

In conclusion, whatever the scalings of E_+, one can expect measured values of the von Kármán coefficient to be non-universal as has indeed been recently reported by Nagib and Chauhan (2008).

3.6 High Reynolds number DNS data

Some of the above results and conclusions are now tested on a set of data which includes the highest Reynolds number channel flow computations currently available (Hoyas and Jiménez, 2006), i.e. $\mathcal{R}e_\tau = 2000$. This set also includes data for $\mathcal{R}e_\tau = 950$ (Hoyas and Jiménez, 2006) and case C, the highest Reynolds number DNS of Table 3.1, i.e. $\mathcal{R}e_\tau = 395$. Plots of $\frac{3}{2}\frac{y}{E_+ u_\tau}\frac{\mathrm{d}}{\mathrm{d}y}\langle u\rangle = B_2/(B_3\kappa_s)$ (see Fig. 3.12) and $\frac{y}{u_\tau}\frac{\mathrm{d}}{\mathrm{d}y}\langle u\rangle = B_2/(B_3\kappa)$ (see Fig. 3.13) as well as $\frac{3}{2}B_3\frac{y}{E_+ u_\tau}\frac{\mathrm{d}}{\mathrm{d}y}\langle u\rangle = B_2/\kappa_s$ (see Fig. 3.14) and $B_3\frac{y}{u_\tau}\frac{\mathrm{d}}{\mathrm{d}y}\langle u\rangle = B_2/\kappa$ (see Fig. 3.15) are presented below.

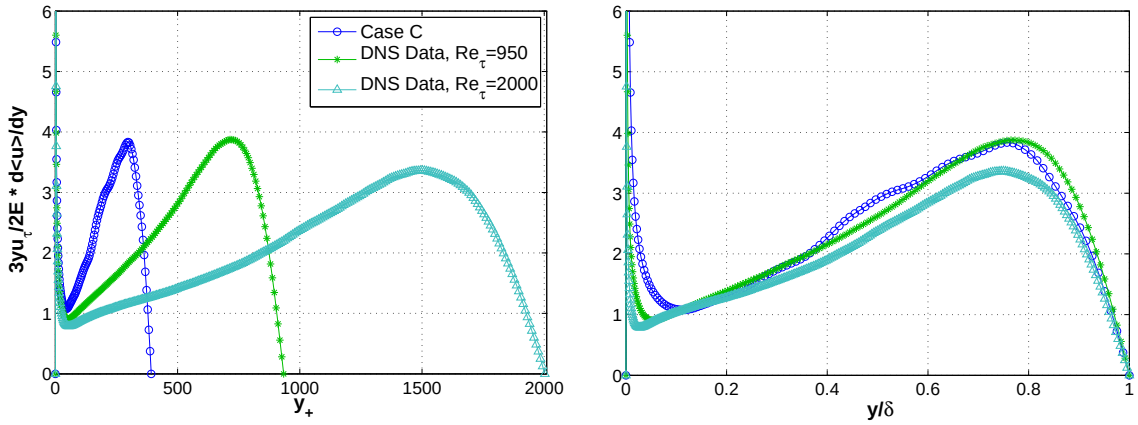

(a) Effectively $\frac{B_2}{B_3\kappa_s}$ versus y_+ (b) Effectively $\frac{B_2}{B_3\kappa_s}$ versus y/δ

Figure 3.12: Plots of $\frac{3}{2}\frac{y}{E_+ u_\tau}\frac{\mathrm{d}}{\mathrm{d}y}\langle u\rangle$ as function of (a) y_+ and (b) y/δ. DNS of turbulent channel flows without wall actuations. The $\mathcal{R}e_\tau = 950$ and 2000 data are from Hoyas and Jiménez (2006).

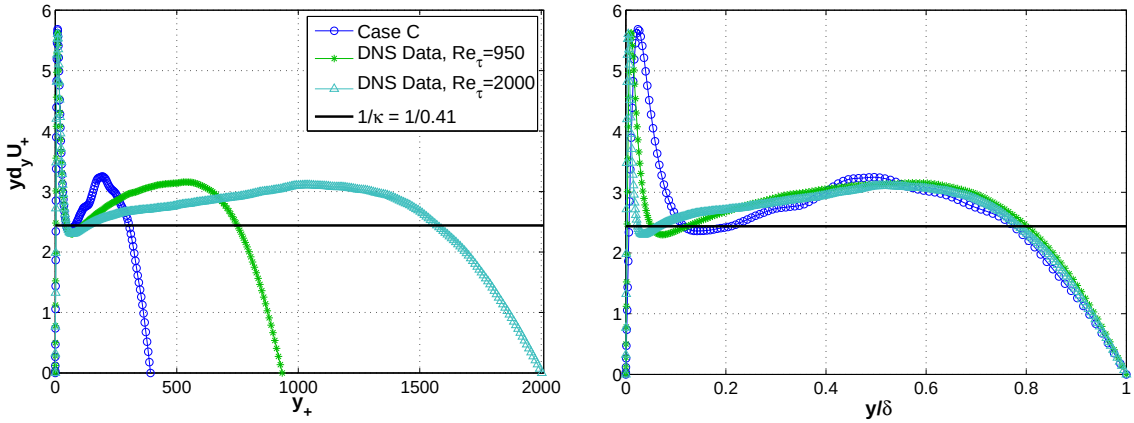

(a) Effectively $\frac{B_2}{B_3\kappa}$ versus y_+ (b) Effectively $\frac{B_2}{B_3\kappa}$ versus y/δ

Figure 3.13: Plots of $\frac{y}{u_\tau}\frac{\mathrm{d}}{\mathrm{d}y}\langle u\rangle$ as function of (a) y_+ and (b) y/δ. DNS of turbulent channel flows without wall actuations. The $\mathcal{R}e_\tau = 950$ and 2000 data are from Hoyas and Jiménez (2006).

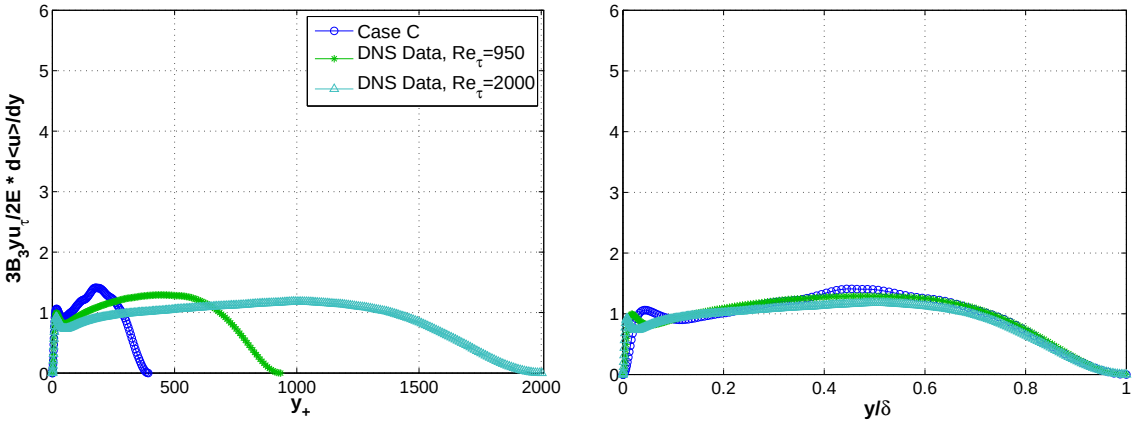

(a) Effectively $\frac{B_2}{\kappa_s}$ versus y_+ (b) Effectively $\frac{B_2}{\kappa_s}$ versus y/δ

Figure 3.14: Plots of $\frac{3}{2}B_3\frac{y}{E_+u_\tau}\frac{\mathrm{d}}{\mathrm{d}y}\langle u\rangle$ as function of (a) y_+ and (b) y/δ. DNS of turbulent channel flows without wall actuations. The $\mathcal{R}e_\tau = 950$ and 2000 data are from Hoyas and Jiménez (2006).

These high Reynolds number results support and extend the claims made in the previous section, i.e. B_2/κ_s appears to have the least departures from constancy in the intermediate range, better than $B_2/(B_3\kappa)$ which is however better than $B_2/(B_3\kappa_s)$. The variations of B_2/κ are offset by those of B_3 (see also Fig. 3.16) which explains why $B_2/(B_3\kappa)$ looks better than $B_2/(B_3\kappa_s)$. The situation re-

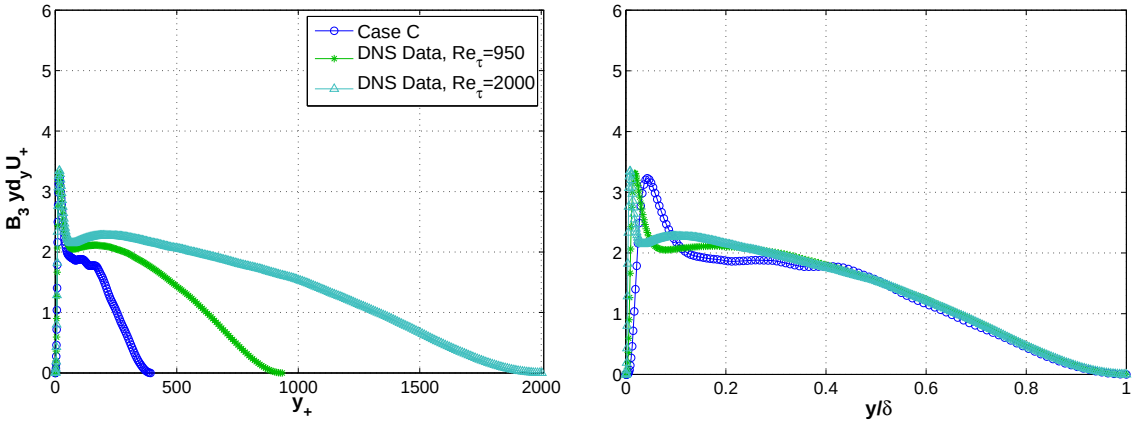

(a) Effectively $\frac{B_2}{\kappa}$ versus y_+ (b) Effectively $\frac{B_2}{\kappa}$ versus y/δ

Figure 3.15: Plots of $B_3 \frac{y}{u_\tau} \frac{\mathrm{d}}{\mathrm{d}y} \langle u \rangle$ as function of (a) y_+ and (b) y/δ. DNS of turbulent channel flows without wall actuations. The $\mathcal{R}e_\tau = 950$ and 2000 data are from Hoyas and Jiménez (2006).

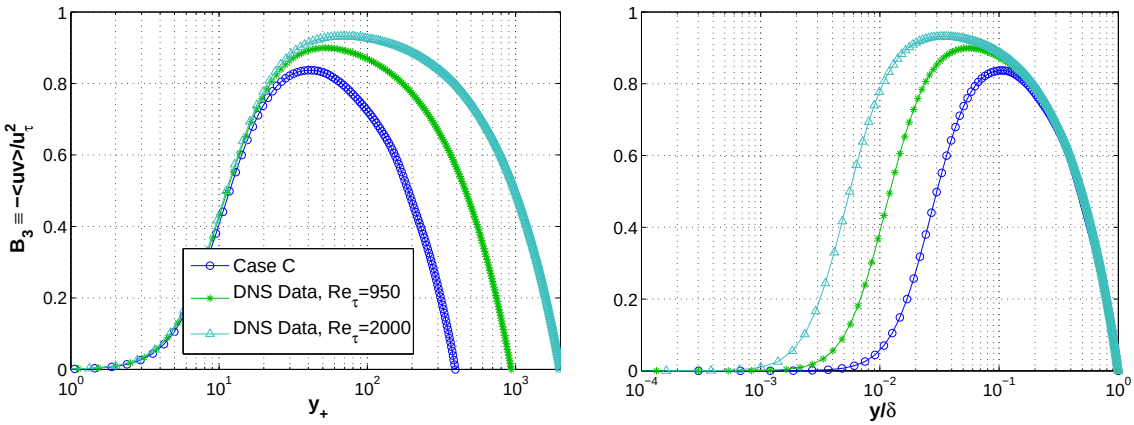

(a) (b)

Figure 3.16: Plots of $B_3 \equiv -\langle uv \rangle / u_\tau^2$ as function of (a) y_+ and (b) y/δ. DNS of turbulent channel flows without wall actuations. The $\mathcal{R}e_\tau = 950$ and 2000 data are from Hoyas and Jiménez (2006).

mains therefore identical to the one that was encountered with the lower Reynolds number simulations in the previous section. It is necessary that $\mathcal{R}e_\tau \gg 2000$ to come close to the asymptotic value $B_3 \to 1$ in an intermediate layer (see Fig. 3.16), as already shown by experimental measurements spanning an ever wider Reynolds number range in Nagib and Chauhan (2008).

The classical similarity scaling $E \propto u_\tau^2$ for $\mathcal{R}e_\tau \gg 1$ is not obvious even at this high Reynolds numbers data of very laborious DNS (see Fig. 3.18a). Thus, Eq. (3.16) suggests that power-laws cannot be ruled out. Alternative forms for the mean flow profile at high Reynolds numbers have also been proposed in the literature (see section 2.3.1 and Barenblatt (1996); George (2007)) and in Fig. 3.17 the suggestion of a power-law form is assessed. The high Reynolds number data used here appears to give significant support to such a power-law form with power exponent $n \equiv \frac{y}{U_+}\frac{\mathrm{d}}{\mathrm{d}y}U_+ \simeq 2/15$, i.e. $\frac{\mathrm{d}}{\mathrm{d}y_+}U_+ \propto y_+^{-(1+2/15)}$ in the intermediate layer. On

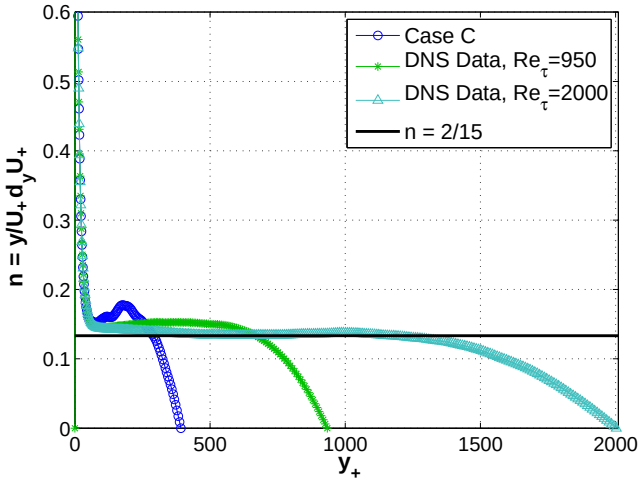

Figure 3.17: Power law mean velocity profile: $n = \frac{y}{U_+}\frac{\mathrm{d}}{\mathrm{d}y}U_+$ plotted against y_+. DNS of turbulent channel flows without wall actuations. The $\mathcal{R}e_\tau = 950$ and 2000 data are from Hoyas and Jiménez (2006).

the basis of Eq. (3.16), this result suggests that E_+ has a power-law dependence on y_+ in that same layer. Indeed, combining Eq. (3.16) in its finite Reynolds number form, i.e. $\frac{\mathrm{d}}{\mathrm{d}y}\langle u\rangle \simeq \frac{2}{3}\frac{B_2}{B_3}E_+\frac{u_\tau}{\kappa_s y}$, with $\frac{\mathrm{d}}{\mathrm{d}y_+}U_+ \simeq \frac{B_4}{\kappa_s}y_+^{-(1+2/15)}$ yields $E_+ y_+^{2/15}\frac{B_2}{B_3} \simeq \frac{3}{2}B_4$, i.e. a constant value of $E_+ y_+^{2/15}B_2/B_3$ in the equilibrium layer if B_4 is constant in that layer. Figure 3.18b supports this conclusion though with a constant value of $E_+ y_+^{2/15}B_2/B_3$ which appears to increase slowly with Reynolds number. This Reynolds number dependence may be intrinsic to E_+ resulting, perhaps, from Townsend's attached eddy hypothesis.

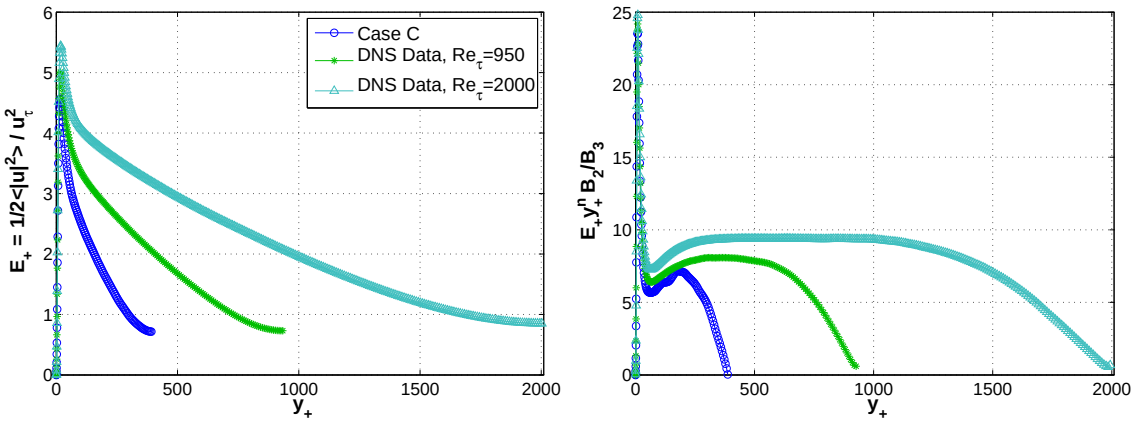

(a) $E_+ = \frac{1}{2}\frac{\langle |\boldsymbol{u}|^2 \rangle}{u_\tau^2}$ versus y_+

(b) $E_+ y_+^n \frac{B_2}{B_3}$ versus y_+

Figure 3.18: Plots of (a) E_+ and (b) $E_+ y_+^n \frac{B_2}{B_3}$ with $n = \frac{2}{15}$ as functions of y_+ for DNS of turbulent channel flows without wall actuations. The $\mathcal{R}e_\tau = 950$ and 2000 are from Hoyas and Jiménez (2006).

3.7 Summary

On the basis of various DNS of turbulent channel flows and the framework of multiscale flow topology, using stagnation points, the following picture is proposed. (*i*) At a height y from either wall, the Taylor microscale λ is proportional to the average distance ℓ_s between stagnation points of the fluctuating velocity field, i.e. $\lambda(y) = B_1 \ell_s(y)$ with B_1 constant, for $\delta_\nu \ll y \lesssim \delta$, where the wall unit δ_ν is defined as the ratio of kinematic viscosity ν to skin friction velocity u_τ and δ is the channel's half width. (*ii*) The number density n_s of stagnation points varies with height according to $n_s = \frac{C_s}{\delta_\nu^3} y_+^{-1}$ where y_+ and C_s is constant in the range $\delta_\nu \ll y \lesssim \delta$. (*iii*) In that same range, the kinetic energy dissipation rate per unit mass, $\epsilon = \frac{2}{3} E_+ \frac{u_\tau^3}{\kappa_s y}$ where $\kappa_s = B_1^2/C_s$ is the stagnation point von Kármán coefficient. (*iv*) In the limit of exceedingly large $\mathcal{R}e_\tau$, large enough for the Reynolds stress $-\langle uv \rangle$ to equal u_τ^2 in the range $\delta_\nu \ll y \ll \delta$, and assuming that production of turbulent kinetic energy balances dissipation locally in that range and limit, the normalised mean velocity U_+ obeys $\frac{\mathrm{d}}{\mathrm{d}y} U_+ \simeq \frac{2}{3}\frac{E_+}{\kappa_s y}$ in that same range. (*v*) It follows that the von Kármán coefficient κ is a meaningful and well-defined coefficient and the log-law holds in turbulent channel/pipe flows only if E_+ is independent of y_+ and $\mathcal{R}e_\tau$ in that range, in which case $\kappa \propto \kappa_s$. (*vi*) In support of $\frac{\mathrm{d}}{\mathrm{d}y} U_+ \simeq \frac{2}{3}\frac{E_+}{\kappa_s y}$, DNS data of turbulent channel

flows which include the highest currently available values of $\mathcal{R}e_\tau$ are best fitted by $E_+ \simeq \frac{2}{3}B_4 y_+^{-2/15}$ and $\frac{\mathrm{d}}{\mathrm{d}y_+}U_+ \simeq \frac{B_4}{\kappa_s} y_+^{-1-2/15}$ with B_4 independent of y in $\delta_\nu \ll y \ll \delta$ if the significant departure from $-\langle uv \rangle \simeq u_\tau^2$ at these $\mathcal{R}e_\tau$ values is taken into account.

Chapter 4

Viscoelastic turbulence: a brief introduction

After giving a short introduction in classical hydrodynamic wall-bounded turbulence, the basics of polymeric fluids and the phenomenon of polymer drag reduction are presented in this chapter, before studying viscoelastic turbulence in a channel flow and the dynamics of polymer-turbulence interactions. Section 4.1 consists of the preliminaries on polymers and their dynamics in fluids. The derivation of the evolution equation for the elastic dumbbell, a classic mechanical model that represents the conformations of a polymer molecule, is described in section 4.2. This section starts with polymer kinetic theory as the basis and draws up a governing equation for a continuum field, leading eventually to the FENE-P model, a typical closure which has been employed frequently in numerical simulations to reproduce turbulent drag reduction of viscoelastic solutions. Here emphasis has given on the correct formulation of the FENE-P model, since there are several false formulations in the literature that improperly combine two different normalisations (Jin and Collins, 2007). In the end, section 4.3 provides an overview of polymer drag reduction and some of the most favourite candidate phenomenologies proposed during the years of research. It is notable to mention that by the year 1995 there were about 2500 papers on the subject (Procaccia et al., 2008). Detailed reviews on various aspects of polymer drag reduction are provided by Lumley (1969); Virk (1975); De Gennes (1990); McComb (1992); Gyr and Bewersdorff (1995); Sreenivasan and White (2000); Bismarck et al. (2008); White and Mungal (2008).

4.1 Polymer dynamics in fluids

A polymer molecule consists of a large number of identical units, the monomers, which are linked by chemical bonds forming a long chain. The typical number of monomers for PEO, i.e. Polyethylene oxide ($N \times [-CH_2-CH_2-O]$), one of the most commonly used polymers in drag reduction experiments, is $N \sim \mathcal{O}(10^4 - 10^6)$. This very large number of monomers induces many degrees of freedom but it was shown during years of research (Doi and Edwards, 1986; Bird et al., 1987; Larson, 1988) that the most important degree of freedom is the end-to-end distance, which corresponds to the largest characteristic time scale of a coil. The definition of the average time scale of a stretched coil to relax back to its equilibrium configuration, as a result of Brownian bombardment, has been given by Zimm (1956)

$$\tau_p \simeq \frac{\mu_s R_G^3}{\kappa_B T} \tag{4.1}$$

where μ_s is the solvent viscosity, R_G is the radius of gyration for a polymer at rest, κ_B is the Boltzmann constant and T is the solution temperature.

A polymer in solution is in a coiled state of spherical shape in a statistical sense, which corresponds to the average of all possible configurations. For linear flexible polymer molecules in good solvent at equilibrium, Flory's law (Flory, 1989) holds for the average coil size

$$R_G \simeq N^{3/5}\alpha \tag{4.2}$$

where α is the monomer length, with typical values of R_G ranging between $0.1-1\,\mu m$. The elongated shape of a stretched polymer in a fluid is characterised by its end-to-end distance $R \gg R_G$. Even R_{max}, the maximum polymer elongation, is much smaller than Kolmogorov viscous scale η, allowing one to consider the fluctuating velocity around a polymer in a turbulent flow, as homogeneous shear.

The relative strength between the relaxation of the polymer and stretching exerted by the flow is expressed by Weissenberg number, defined as

$$\mathcal{W}e \equiv \frac{\tau_p}{\tau_f} \tag{4.3}$$

where τ_f is a characteristic flow time scale. For $\mathcal{W}e \gg 1$, polymers become substantially elongated by the flow, as the coil relaxation is much slower than the stretching

flow time scale. This variation in the coil shape is named *coil-stretch transition*. In contrast, for $\mathcal{W}e \ll 1$ the polymer molecules remain passive in their coiled state.

The enormous number of degrees of freedom of each coil makes a polymer macromolecule an extraordinary complex system, whose dynamics depend on the conformations of the polymer molecules, i.e. orientation and degree of stretching of coils. The study of detailed motions of this complex system and their relations to the non-equilibrium properties would be prohibitive. Only after elimination of the fast relaxation processes of local motions in favour of stochastic noise, it is possible to study the dynamics of longer relaxation time scales (Öttinger, 1996), such as the end-to-end conformation, that are responsible for many physical properties of polymers in fluids, such as viscoelastic turbulence and polymer drag reduction. Thus, coarse-grained mechanical models, such as bead-rod-spring models, are very crucial in polymer kinetic theory (Doi and Edwards, 1986; Bird et al., 1987; Öttinger, 1996).

The concentration of polymers in a turbulent flow can be assumed to be well mixed and roughly homogeneous. So, for a consistent hydrodynamic description of dilute polymer solutions, where interactions between different polymer molecules are ignored, a field of polymers needs to be considered rather than individual coils. Consequently, in this study a continuum mechanical approach is preferable under these conditions, making mathematical and numerical treatments more tractable than for kinetic theories. Then, the governing equations for an incompressible fluid with polymers are given by the conservation of mass and momentum balance

$$\begin{aligned} \boldsymbol{\nabla} \cdot \boldsymbol{u} &= 0 \\ \rho D_t \boldsymbol{u} &= -\boldsymbol{\nabla} p + \boldsymbol{\nabla} \cdot \boldsymbol{\sigma} \end{aligned} \tag{4.4}$$

where $\boldsymbol{\sigma}$ is the total stress tensor. Here, the total stress is the sum of a Newtonian part $\boldsymbol{\sigma}^{(s)}$ due to the solvent and a non-Newtonian part $\boldsymbol{\sigma}^{(p)}$ due to the long-chain polymer molecules dissolved in the fluid according to

$$\boldsymbol{\sigma} = \boldsymbol{\sigma}^{(s)} + \boldsymbol{\sigma}^{(p)} = 2\beta\mu_0 \boldsymbol{s} + \boldsymbol{\sigma}^{(p)} \tag{4.5}$$

where $\beta \equiv \mu_s/\mu_0$ is the ratio of the solvent viscosity μ_s to the total zero-shear-rate viscosity of the solution μ_0 and $\boldsymbol{s}$ is the fluctuating strain rate tensor. The polymer stress tensor must be related to the flow field and to the polymer configuration. The

next section provides details on the dynamics of a mechanical model, a bead-spring model for dilute polymer solutions that captures the conformation of the end-to-end distance relaxation process of the entire molecule relating it to the stress tensor.

4.2 Elastic dumbbell model

Consider an elastic dumbbell immersed in a Newtonian fluid, consisting of two beads and a spring in between. The configuration of a dumbbell is represented by the end-to-end vector $\boldsymbol{Q}$ that specifies the length and direction of the dumbbell.

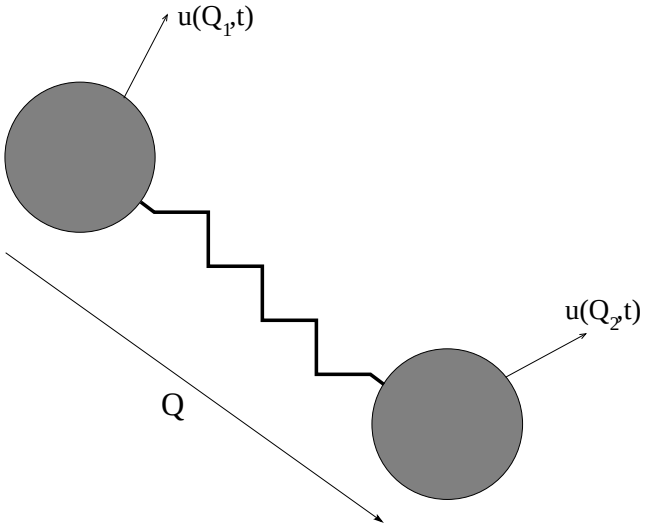

Figure 4.1: The elastic dumbbell model.

Following Bird et al. (1987), it is assumed that the velocity flow field $\boldsymbol{u}$ around the dumbbell is homogeneous, the hydrodynamic interactions, i.e. any effect of the beads on the flow, and external forces, such as gravity and inertia of the beads, are neglected because it can be shown that the centre of mass of a dumbbell moves with the local flow velocity. Hence, Newton's second law for the dumbbell takes the form

$$-\zeta\left(\frac{\mathrm{d}\boldsymbol{Q}}{\mathrm{d}t}-(\boldsymbol{Q}\cdot\boldsymbol{\nabla})\boldsymbol{u}\right)+\boldsymbol{F}_B+\boldsymbol{F}_S=0 \tag{4.6}$$

where the first term is the viscous drag force $\boldsymbol{F}_D$, resulting from the drag the solvent exerts on the beads, the second term a random Brownian force $\boldsymbol{F}_B$, due to the impact of solvent molecules on the beads and an elastic spring force $\boldsymbol{F}_S$, which is the result

of the dumbbell intramolecular potential. $\boldsymbol{F}_D$ is proportional to the discrepancy between the bead velocities $\mathrm{d}\boldsymbol{Q}/\mathrm{d}t$ and the relative flow velocities near the beads $(\boldsymbol{Q}\cdot\boldsymbol{\nabla})\boldsymbol{u}$. The constant of proportionality for the drag force is $\zeta = 6\pi\mu_s R_G$ according to Stokes' law, considering spherical beads.

Equation (4.6) combines macroscopic forces ($\boldsymbol{F}_D$) with microscopic forces ($\boldsymbol{F}_B$) and that is why it is of Langevin type. A Langevin equation is not solvable in the conventional deterministic sense because of the random Brownian term. However, one can seek the probability density function $\psi(\boldsymbol{Q},t)$ that a dumbbell has an end-to-end vector $\boldsymbol{Q}$ at some time t by considering an ensemble of dumbbells. Then, it is known (Chandrasekhar, 1943) that the Brownian force is equal to

$$\boldsymbol{F}_B = -\kappa_B T \frac{\partial}{\partial \boldsymbol{Q}} \ln\psi. \tag{4.7}$$

Hence, the Langevin equation (4.6) can be rewritten as

$$\frac{\mathrm{d}\boldsymbol{Q}}{\mathrm{d}t} = (\boldsymbol{Q}\cdot\boldsymbol{\nabla})\boldsymbol{u} - \frac{\kappa_B T}{\zeta}\frac{\partial}{\partial \boldsymbol{Q}}\ln\psi - \frac{1}{\zeta}\boldsymbol{F}_S \tag{4.8}$$

Now, multiplying Eq. (4.8) by ψ, differentiating with respect to $\boldsymbol{Q}$ and using the probability balance equation in $\mathbb{Q}$-space

$$\partial_t\psi + \frac{\partial}{\partial \boldsymbol{Q}}\cdot\boldsymbol{J}_p = 0 \tag{4.9}$$

which can be derived in a similar manner to continuity equation (2.1) in real space $\mathbb{R}^3$ (Larson, 1988), with $\boldsymbol{J}_p \equiv \frac{\mathrm{d}\boldsymbol{Q}}{\mathrm{d}t}\psi$ the probability flux vector, a diffusion or Smoluchowski equation can be obtained

$$\partial_t\psi + \frac{\partial}{\partial \boldsymbol{Q}}\cdot\left[(\boldsymbol{Q}\cdot\boldsymbol{\nabla})\boldsymbol{u}\psi - \frac{\kappa_B T}{\zeta}\frac{\partial\psi}{\partial \boldsymbol{Q}} - \frac{\psi}{\zeta}\boldsymbol{F}_S\right] = 0 \tag{4.10}$$

since $\psi\frac{\partial}{\partial \boldsymbol{Q}}\ln\psi = \psi\frac{1}{\psi}\frac{\partial\psi}{\partial \boldsymbol{Q}} = \frac{\partial\psi}{\partial \boldsymbol{Q}}$. Eventually, a Fokker-Planck equation can be derived for ψ

$$\partial_t\psi + (\boldsymbol{Q}\cdot\boldsymbol{\nabla})\boldsymbol{u}\cdot\frac{\partial\psi}{\partial \boldsymbol{Q}} - \frac{\kappa_B T}{\zeta}\frac{\partial^2\psi}{\partial \boldsymbol{Q}^2} - \frac{1}{\zeta}\frac{\partial}{\partial \boldsymbol{Q}}\cdot(\psi\boldsymbol{F}_S) = 0 \tag{4.11}$$

taking into account that

$$\begin{aligned}\frac{\partial}{\partial \boldsymbol{Q}} \cdot [(\boldsymbol{Q} \cdot \boldsymbol{\nabla})\boldsymbol{u}\psi] &= \partial_{Q_i}(Q_j \partial_{x_j} u_i)\psi + (Q_j \partial_{x_j} u_i)\partial_{Q_i}\psi \\ &= \delta_{ji}\partial_{x_j} u_i \psi + Q_j \partial_{Q_i}\partial_{x_j} u_i \psi + (Q_j \partial_{x_j} u_i)\partial_{Q_i}\psi \\ &= (\boldsymbol{\nabla} \cdot \boldsymbol{u})\psi + (\boldsymbol{Q} \cdot \boldsymbol{\nabla})\boldsymbol{u} \cdot \frac{\partial \psi}{\partial \boldsymbol{Q}} \\ &= (\boldsymbol{Q} \cdot \boldsymbol{\nabla})\boldsymbol{u} \cdot \frac{\partial \psi}{\partial \boldsymbol{Q}} \end{aligned} \tag{4.12}$$

A consistent hydrodynamic description in terms of the effects of the ensemble of polymers in solution is provided by a continuum approach. The fact that the most important degree of freedom for a single chain is the end-to-end distance makes the derivation of a constitutive equation for the conformation tensor imperative. The conformation tensor is the ensemble average of the dyadic product of the end-to-end vector of the polymer chain, viz. $\langle \boldsymbol{QQ} \rangle = \int\limits_{\mathbb{R}^3} \boldsymbol{QQ}\psi(\boldsymbol{Q}, t)\mathrm{d}^3 Q$. Multiplying Eq. (4.11) with $\boldsymbol{QQ}$, taking the ensemble average by integrating over $\mathbb{R}^3$ and using the divergence theorem and the fact that $\psi \to 0$ at maximum $|\boldsymbol{Q}|$ (Larson, 1988) gives

$$\partial_t \langle \boldsymbol{QQ} \rangle + (\boldsymbol{u} \cdot \boldsymbol{\nabla}) \langle \boldsymbol{QQ} \rangle = \langle \boldsymbol{QQ} \rangle \cdot \boldsymbol{\nabla}\boldsymbol{u} + \boldsymbol{\nabla}\boldsymbol{u}^\top \cdot \langle \boldsymbol{QQ} \rangle + \frac{2\kappa_B T}{\zeta}\boldsymbol{I} - \frac{2}{\zeta}\langle \boldsymbol{QF}_S \rangle \tag{4.13}$$

Ultimately, the left hand side of the evolution equation for the conformation tensor convects the dumbbells through the flow, the first two terms on the right hand side describe deformation by hydrodynamic forces, the third term refers to Brownian motion and the fourth term is the elastic retraction of the coil due to some spring force.

4.2.1 Finite Extensible Nonlinear Elastic model

The polymer stress tensor involves contributions from the motion of the beads and the intramolecular potential, i.e. the connecting spring in this particular case. Based on kinetic theory arguments, the Kramers expression for the stress can be derived (Bird et al., 1987; Öttinger, 1996), which relates the stress tensor $\boldsymbol{\sigma}^{(p)}$ to the ensemble average of the dyadic product $\boldsymbol{QF}_S$, viz.

$$\boldsymbol{\sigma}^{(p)} = -n_p \kappa_B T \boldsymbol{I} + n_p \langle \boldsymbol{QF}_S \rangle \tag{4.14}$$

where n_p is the number density of polymers per unit volume. The first term in Eq. (4.14) represents isotropic equilibrium and the second the deviation from this equilibrium because of intramolecular forces.

The spring force is a vital ingredient for the mean field representation of polymer dynamics through the stress tensor. A Hookean spring force provides infinite extensibility, whereas real polymers can get extended to their fully stretched length at most, unless degradation takes place. Hence, this linear spring-force law is a poor approximation for large polymer extensions. There are more realistic spring forces instead, like Warner's finite extensible nonlinear elastic (FENE) spring-force law (Warner, 1972)

$$\boldsymbol{F}_S = \frac{H\boldsymbol{Q}}{1 - Q^2/Q_0^2} \tag{4.15}$$

where H is the spring constant, $Q^2 = tr\boldsymbol{QQ}$ is the squared actual length of the polymer and $Q_0^2 \equiv b\kappa_B T/H$ is the maximum separation of the beads, with b, a dimensionless length parameter describing the finite extensibility of these springs. Values of b cannot be chosen arbitrarily. According to Öttinger (1996), the bond angles for a chain with a pure carbon backbone are known and one can obtain the estimate

$$b \approx \frac{N_C}{\sigma_{sf}^2 N} \tag{4.16}$$

where N_C is the number of carbon atoms in the backbone of the polymer macromolecule, σ_{sf} is an empirical steric factor and b is supposed to be a large number. Note that in the limit $b \to \infty$, the Hookean spring-force law is recovered, viz. $\boldsymbol{F}_S = H\boldsymbol{Q}$.

In this study, a modification of the FENE model is employed, called the FENE-P model (Bird et al., 1980), which is a closure for $\boldsymbol{\sigma}^p$ in terms of $\langle \boldsymbol{QQ} \rangle$ introduced through the Peterlin (1961) linearisation and comes in Warner's force as follows

$$\boldsymbol{F}_S = \frac{H\boldsymbol{Q}}{1 - \langle Q^2 \rangle / Q_0^2}. \tag{4.17}$$

Then, Kramers expression for the stress tensor Eq. (4.14) becomes

$$\boldsymbol{\sigma}^{(p)} = -n_p \kappa_B T \boldsymbol{I} + n_p \frac{\langle \boldsymbol{QQ} \rangle}{1 - \langle Q^2 \rangle / Q_0^2}. \tag{4.18}$$

According to Wedgewood and Bird (1988), the parameter $n_p\kappa_B T$ can be related to the viscosity ratio β, which is inversely proportional to the polymer concentration, through equation

$$\mu_p = (1-\beta)\mu_0 = n_p\kappa_B T\tau_p \frac{b}{b+3} \tag{4.19}$$

where μ_p is the intrinsic polymer viscosity and the relaxation time scale of the polymer can be given in terms of the model parameters as $\tau_p \equiv \zeta/2H$.

The dumbbell vector can be scaled with the equilibrium length $\sqrt{\kappa_B T/H}$, so that $\widetilde{\boldsymbol{Q}} = \boldsymbol{Q}/\sqrt{\kappa_B T/H}$ and the conformation tensor $\boldsymbol{C} = \langle \widetilde{\boldsymbol{Q}}\widetilde{\boldsymbol{Q}} \rangle$, which is symmetric and strictly positive definite*. At this point, Eq. (4.18) combined with Eq. (4.19) and using the definition of Q_0^2 implies

$$\boldsymbol{\sigma}^{(p)} = \frac{(1-\beta)\mu_0}{\tau_p}\frac{b+3}{b}\left(\frac{\boldsymbol{C}}{1-tr\boldsymbol{C}/b} - \boldsymbol{I}\right). \tag{4.20}$$

Moreover, it is preferred to normalise such that the equilibrium condition is defined as $\widetilde{\boldsymbol{C}}_{eq} = \boldsymbol{I}$ (Jin and Collins, 2007). So, after some algebra Eq. (4.20) entails

$$\boldsymbol{\sigma}^{(p)} = \frac{(1-\beta)\mu_0}{\widetilde{\tau}_p}\left(f(tr\widetilde{\boldsymbol{C}})\widetilde{\boldsymbol{C}} - \boldsymbol{I}\right) \tag{4.21}$$

with $\widetilde{\tau}_p = \frac{b}{b+3}\tau_p$, $\widetilde{\boldsymbol{C}} = \frac{b+3}{b}\boldsymbol{C}$ and the Peterlin function

$$f(tr\widetilde{\boldsymbol{C}}) = \frac{L_p^2 - 3}{L_p^2 - tr\widetilde{\boldsymbol{C}}} \tag{4.22}$$

where $L_p^2 = b+3$ is the length of the fully stretched polymer coil and $tr\widetilde{\boldsymbol{C}} \leq L_p^2$ preventing the dumbbell to reach each maximum extensibility, since as $tr\widetilde{\boldsymbol{C}} \to L_p^2$ the force required for further extension approaches infinity. Then, using Eq. (4.17) and based on this normalisation Eq. (4.13) can be rewritten as

$$\partial_t\widetilde{\boldsymbol{C}} + (\boldsymbol{u}\cdot\boldsymbol{\nabla})\widetilde{\boldsymbol{C}} = \widetilde{\boldsymbol{C}}\cdot\boldsymbol{\nabla}\boldsymbol{u} + \boldsymbol{\nabla}\boldsymbol{u}^\top\cdot\widetilde{\boldsymbol{C}} - \frac{1}{\widetilde{\tau}_p}(f\widetilde{\boldsymbol{C}} - \boldsymbol{I}). \tag{4.23}$$

Essentially, this evolution equation as well as Eqs. (4.4), (4.5) and (4.21) form a closed set of equations.

*A symmetric matrix $\boldsymbol{C}$ is *strictly positive definite* if $\boldsymbol{x}\boldsymbol{C}\boldsymbol{x}^\top > 0$, $\forall \boldsymbol{x} \neq 0$

The elastic potential energy per unit volume E_p stored by FENE-P dumbbells can now be specified using Eq. (4.17) as follows

$$\begin{aligned} E_p &= n_p \int \boldsymbol{F}_S(\boldsymbol{Q}) \mathrm{d}^3 Q \\ &= n_p \int \frac{H\boldsymbol{Q}}{1 - tr\left\langle \boldsymbol{QQ} \right\rangle / Q_0^2} \mathrm{d}^3 Q \\ &= -\frac{n_p H Q_0^2}{2} \int \frac{-2\boldsymbol{Q}/Q_0^2}{1 - tr\left\langle \boldsymbol{QQ} \right\rangle / Q_0^2} \mathrm{d}^3 Q \\ &= -\frac{n_p H Q_0^2}{2} \ln(1 - \left\langle Q^2 \right\rangle / Q_0) + E_{p_0} \\ &= \frac{n_p \kappa_B T b}{2} \ln(1 - tr\boldsymbol{C}/b)^{-1} + E_{p_0} \\ &= \frac{(1-\beta)\mu_0 (L_p^2 - 3)}{2\widetilde{\tau}_p} \ln(f(tr\widetilde{\boldsymbol{C}})) + E_{p_0} \end{aligned} \tag{4.24}$$

where E_{p_0} is a constant reference energy at equilibrium. After that, taking the time derivative of the elastic potential energy

$$\partial_t E_p = \frac{(1-\beta)\mu_0}{2\widetilde{\tau}_p}(L_p^2 - 3)\frac{1}{f}\frac{\partial f}{\partial \widetilde{C}_{ii}}\frac{\partial \widetilde{C}_{ii}}{\partial t} = \frac{(1-\beta)\mu_0}{2\widetilde{\tau}_p} f \frac{\partial \widetilde{C}_{ii}}{\partial t}, \tag{4.25}$$

using the trace of Eq. (4.23), viz.

$$\frac{\partial \widetilde{C}_{ii}}{\partial t} = 2\widetilde{C}_{ik}\partial_k u_i - \frac{1}{\tau_p}(f(\widetilde{C}_{kk})\widetilde{C}_{ii} - \delta_{ii}) \tag{4.26}$$

and similarly for the $\boldsymbol{\nabla} E_p$, one can derive the following balance equation for the elastic potential energy of FENE-P dumbbells

$$\partial_t E_p + \boldsymbol{u} \cdot \boldsymbol{\nabla} E_p = \boldsymbol{\sigma}^{(p)} \cdot \boldsymbol{\nabla} \boldsymbol{u} - \frac{1}{2\widetilde{\tau}_p} f(tr\widetilde{\boldsymbol{C}}) tr\boldsymbol{\sigma}^{(p)} \tag{4.27}$$

where E_p is produced by $\boldsymbol{\sigma}^{(p)} \cdot \boldsymbol{\nabla} \boldsymbol{u}$, dissipated by $\frac{1}{2\widetilde{\tau}_p} f(tr\widetilde{\boldsymbol{C}}) tr\boldsymbol{\sigma}^{(p)}$ and transported by $\boldsymbol{u} \cdot \boldsymbol{\nabla} E_p$.

The FENE-P model is the most widely used coarse-grained model that has successfully reproduced qualitatively the phenomenon of polymer drag reduction in DNS of various turbulent flows, such as channel flows (Sureshkumar et al., 1997; Dimitropoulos et al., 1998; De Angelis et al., 2002; Sibilla and Baron, 2002; Dubief et al.,

2004; Ptasinski et al., 2003; Li et al., 2006), boundary layers (Dimitropoulos et al., 2005, 2006) and homogeneous flows (De Angelis et al., 2005; Kalelkar et al., 2005; Perlekar et al., 2006; Vaithianathan et al., 2006). There have been several studies (Massah et al., 1993; Van Heel et al., 1998; Ilg et al., 2002; Zhou and Akhavan, 2003; Terrapon et al., 2004; Jin and Collins, 2007) comparing the performance of various more detailed polymer models with FENE-P to quantify the errors associated with its coarse-grained assumption of the polymer dynamics. Although there are cases in which the particular model does not capture the correct detailed physics, the overall performance, in terms of its prediction of average properties of the polymer-turbulence interaction, is close to more advanced models and experimental results.

4.3 Polymer drag reduction phenomenologies in turbulent flows

The phenomenon of drag, which is distinguished from viscous dissipation, should be discussed in the context of wall-bounded turbulent flows. The existence of a wall breaks homogeneity and together with the no-slip wall boundary condition it sets a momentum flux from the bulk to the wall, which is responsible for the drag. As was mentioned in section 2.3, the force necessary to drive the flow through a channel is a negative time-averaged mean pressure gradient along the length of the channel, $-\mathrm{d}\langle p\rangle/\mathrm{d}x$. Therefore, in this context the drag reduction can be defined as

$$\%DR \equiv \frac{-\frac{\mathrm{d}\langle p\rangle}{\mathrm{d}x} - \left(-\frac{\mathrm{d}\langle p\rangle}{\mathrm{d}x}\right)\Big|_0}{-\frac{\mathrm{d}\langle p\rangle}{\mathrm{d}x}\Big|_0} \cdot 100 = \frac{u_\tau^2 - u_\tau^2\big|_0}{u_\tau^2\big|_0} \cdot 100 = \left(\left(\frac{\mathcal{R}e_\tau}{\mathcal{R}e_{\tau 0}}\right)^2 - 1\right) \cdot 100 \quad (4.28)$$

where $u_\tau^2 = -\frac{\delta}{\rho}\frac{\mathrm{d}\langle p\rangle}{\mathrm{d}x}$ and quantities with and without subscript 0 refer to Newtonian[†]and viscoelastic fluid flow, respectively.

The addition of minute concentrations of long chain polymer molecules to wall-bounded turbulent flows can dramatically reduce frictional drag, as was discovered by Toms (1948), while performing experiments on the degradation of polymers. To rephrase this, a few parts per million by weight polymer are enough to reduce the

[†]Any departure from the Newtonian behaviour, i.e. $\sigma_{ij} \propto S_{ij}$, with some constant of proportionality independent of the rate of strain, should be called non-Newtonian.

force necessary to drive the flow through a channel by a factor of up to 70%. Turbulence is a multiscale phenomenon with a vast spectrum of spatial scales and therefore a very large number of degrees of freedom. Therefore, due to the fact that even $R_{max} \ll \eta$, one might anticipate that the small size polymers can only affect sub-Kolmogorov scale processes and that scales $\ell > \eta$ would remain unaffected. Surprisingly, the individual dynamics of the small polymer chains are able to fundamentally modify the large scale structures and statistics, as observed by the drag reduction effect.

Polymer drag reduction in wall-bounded turbulent flows induces higher mean velocities, implying changes in the von Kármán law (see Eq. (2.49)). The systematic experimental work by Warholic et al. (1999) classified flows at low drag reduction (LDR) and high drag reduction (HDR) regimes, based on the statistical trends of the turbulent velocity field. In particular, when $|\%DR| \lesssim 40$ (LDR), the mean velocity profile crosses over to a log-law with a higher value of the intercept constant B (see Eq. (2.49)), i.e. larger mean velocity, parallel to the von Kármán law (see Fig. 4.2), though for $40 < |\%DR| \lesssim 60$ (HDR), the slope of the log-region increases until it reaches the empirical maximum drag reduction (MDR) asymptotic limit. This mean velocity profile at MDR was discovered experimentally in pipe flow by Virk et al. (1967); Virk (1975) and it is called the *MDR* or *Virk's asymptote*. This asymptote has also been confirmed experimentally in channel flow by Warholic et al. (1999). Virk et al. (1967); Virk (1975) observed that the mean velocity profile is bounded between von Kármán's logarithmic law and this universal asymptotic state, which is independent of the Newtonian solvent, the characteristics of the polymer additives and the flow geometry, given by the empirical relation

$$U_+ = \frac{1}{\kappa_{\mathrm{v}}} \log y_+ + B_{\mathrm{v}} \tag{4.29}$$

where $\kappa_{\mathrm{v}}^{-1} \simeq 11.7$ and $B_{\mathrm{v}} \simeq -17$. On the other hand, the position of the cross-overs in the LDR and HDR regimes are not universal, because they depend on the polymer characteristics and the flow geometry.

Moreover, the rms streamwise velocity fluctuations u' show an increase at the peak at LDR, but a decrease at HDR, along with a continuous shift of this peak away from the wall throughout the drag reduction regimes. This shift represents the thickening of the elastic layer, which lies between the viscous and the logarithmic layer. The

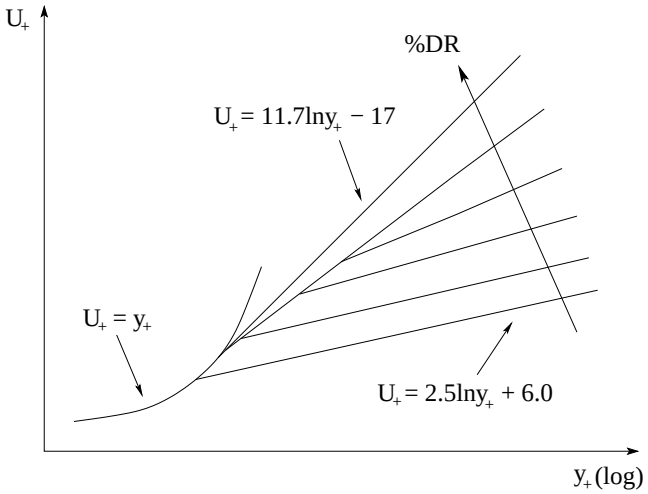

Figure 4.2: Mean velocity profiles at different drag reduction regimes.

wall-normal v' and spanwise w' velocity fluctuations decrease monotonically as well as the Reynolds shear stress $\langle uv \rangle$, and their peak shifts away from the wall, throughout the drag reduction regimes, with the polymer shear stress playing an increasingly important role in sustaining turbulence (White and Mungal, 2008). Warholic et al. (1999) report that turbulence is sustained entirely by the polymer stresses in the HDR and MDR regimes because of the complete attenuation of the Reynolds shear stress that they observe. This is controversial, as other studies (Ptasinski et al., 2003; Min et al., 2003a; Dubief et al., 2004) have observed that Reynolds stress remains finite even though it is strongly diminished at the HDR and MDR regime, which supports the idea that polymer stresses play a more significant role in the near-wall dynamics of the flow than the Reynolds shear stress.

The polymer drag reduction phenomenon has been known for almost sixty years and has attracted attention both from the fundamental and applied perspective, however, a theory for the action of the polymers and its effect on turbulent structures is still elusive (White and Mungal, 2008). A theory of polymer drag reduction should provide an explanation of the drag reduction onset, as well as the MDR law and its universality, which plays a significant fundamental role in understanding the phenomenon. Several theoretical concepts have been proposed but all have been subjected to criticism. The proposed theories mainly fall into two categories, that of viscous (Lumley, 1969; Procaccia et al., 2008) and that of elastic effects (Tabor and de Gennes, 1986; Joseph, 1990; Sreenivasan and White, 2000). The prin-

cipal phenomenology based on viscous explanation can be attributed to the *time-criterion/coil-stretch transition* by Lumley (1969, 1973), which basically claims that drag reduction occurs due to randomly coiled polymers that are fully stretched primarily in regions of high fluctuating strain rates, like the buffer layer, and therefore strongly enhance the elongational (intrinsic[‡]) viscosity. However, observations of drag reduction from polymer injection at the centre of a pipe, where wall effects are not important (McComb and Rabie, 1979; Bewersdorff, 1982, 1984), prompted Tabor and de Gennes (1986); De Gennes (1990) to develop the *elastic theory*, a 'cascade theory' for three-dimensional turbulence without any wall effect, where polymer effects at small scales are described by elasticity and not by viscosity.

Both phenomenologies are conjectural and somewhat qualitative, failing to faithfully reveal the whole picture, with none of them providing a satisfactory explanation for the MDR law. Only recently, Procaccia et al. (2008) presented a phenomenological theory based on Lumley's arguments and by making *ad hoc* assumptions were able to derive the mean velocity profile of Virk's asymptote through closure. The above mentioned phenomenologies appear to have merit due to the fact that some of their concepts find support by numerical and experimental studies. Thus, the subsequent sections analyse their theoretical arguments in further detail.

4.3.1 Time-criterion/Coil-stretch transition

Lumley argued in favour of polymer time scales and their interaction with turbulent fluctuations, in contrast to polymer length scales, based on experimental observations and he proposed the following time-criterion (Lumley, 1969, 1973). Drag reduction due to the onset of remarkable viscoelastic effects occurs in a dilute solution of flexible polymers when the relaxation time of a polymer coil τ_p exceeds a certain hydrodynamic time scale τ_f. In other words, the Weissenberg number has to be greater than one, viz.

$$\mathcal{W}e \equiv \frac{\tau_p}{\tau_f} > 1. \tag{4.30}$$

Whenever, this condition is satisfied the polymer molecules undergo abrupt complete stretching because of local strain rates (coil-stretch transition) (Lumley, 1969, 1973). This was suggested by Lumley based on the approximation that says; if the

[‡]Intrinsic viscosity is a measure of a solute's contribution to the viscosity of a solution.

mean square strain rate $\langle \boldsymbol{S}^2 \rangle$, weighted by the Lagrangian integral time scale $\mathcal{T}_\mathcal{L}$ of the strain rate representing a measure for the persistence of these regions, exceeds a critical value related to the inverse of polymer relaxation time, then the mean square molecular radius $\langle \boldsymbol{R}^2 \rangle$ grows exponentially,

$$\left\langle \boldsymbol{R}^2 \right\rangle \propto \exp\left((2 \left\langle \boldsymbol{S}^2 \right\rangle \mathcal{T}_\mathcal{L} - \frac{1}{\tau_p}) t \right). \tag{4.31}$$

Of course, this growth will be gradual as the individual molecule will contract and expand as it moves through low and high strain regions in the flow, respectively, but the expansion will eventually dominate according to Lumley (1973).

Lumley's picture for drag reduction is depicted in Fig. 4.3 below, with the distribution of wave number k as a function of the distance from the wall y. In a Newtonian turbulent channel flow, k_{min} is determined by the flow geometry and k_{max} by the Kolmogorov viscous limit[§]. Therefore, the eddies exist in the wave number range $\delta^{-1} \leq k < \eta^{-1}$, where δ is the channel half-height and η is the Kolmogorov viscous scale. However, according to Eq. (2.60), $k_{max} = \delta_\nu^{-3/4} y^{-1/4}$ based on Kolmogorov scaling. The geometric and Kolmogorov limits meet at about the edge of the viscous sublayer. In this way, Lumley (1969, 1973) assumed the viscous sublayer as passive, keeping the viscosity at its Newtonian value. He further conjectured that polymers increase the effective viscosity ν_{eff} in turbulent regions, as they go through coil-stretch transition implying a new viscous cut-off in the spectrum, parallel to the Kolmogorov limit $k'_{max} \propto y^{-1/4}$ (see bold-dashed line in Fig. 4.3), which depends on polymer concentration c. Thus, the net result is a thickening of the buffer layer, because of the reduced Reynolds stress that delays the curvature of the mean velocity profile, which is proportional to c and $\%DR$ (Lumley, 1973).

As soon as polymer is added into the flow, the viscous limit shifts and the whole effect occurs at arbitrary low c. Then, Lumley (1973) claims that the momentum transfer is unaltered, since above the new intersection point, the energy containing eddies are unaffected and so the slope of the mean velocity profile is preserved, attempting an interpretation of the LDR regime. As c increases further and the MDR law is approached, the increased ν_{eff} will reduce the average strain rates responsible for the coil-stretch transition, causing no further increase in the buffer layer thickness.

[§]If the assumption of homogeneity is reasonable and the classical picture of Kolmogorov (1941) is roughly valid for turbulent fluctuations at high $\mathcal{R}e_\tau$, away from the wall.

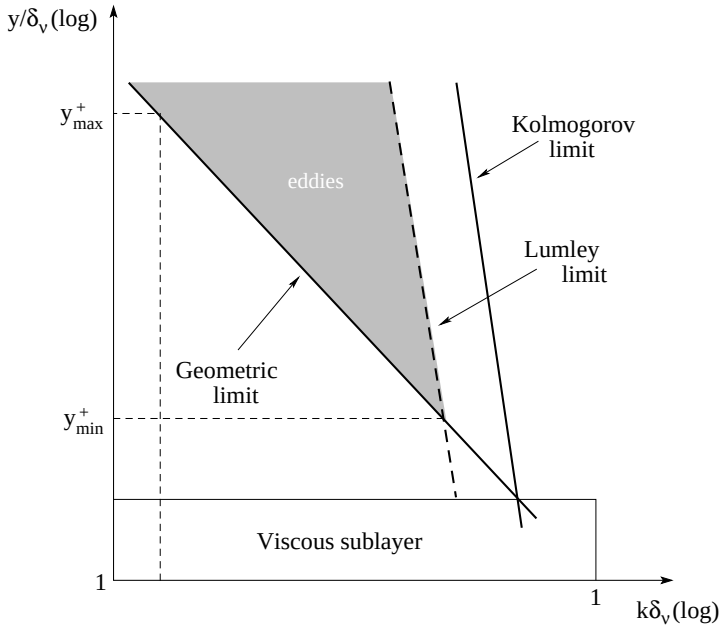

Figure 4.3: Lumley's picture of drag reduction - Distribution of wave vectors k at various distances y from the wall.

Therefore, drag reduction is set independent from polymer concentration, with a further increase in c just resulting in the same effective viscosity.

The limitations of Lumley's phenomenology appear first in the assumption of intrinsic viscosity enhancement due to highly stretched polymer molecules, which is dubious, as the space-time strain rate fluctuations near the wall, even though high, can only cause partial stretching of the coils according to Tabor and de Gennes (1986); Sreenivasan and White (2000). Secondly, the whole concept has been built on wall effects, as viscosity dominates near wall dynamics but, as was mentioned in section 4.3, there have been experiments demonstrating that polymer injection at the centre of a pipe can cause drag reduction before polymers reach the wall.

Procaccia et al. (2008) were able to formulate Lumley's conceptual ideas through scaling arguments and they were able to derive MDR as a marginal flow state of wall-bounded turbulence by (a) assuming that polymers never feed energy back to the flow, based on misleading computations¶. (b) They considered that coil-stretch transition produces a space dependent effective viscosity $\nu_{eff}(y)$ with a linear varia-

¶The computation of viscoelastic turbulence, using models such as FENE-P, is a whole issue that only recently was resolved and will be analysed further in chapter 5.

tion in y, and (c) they also closed the problem with a supplementary relation between Reynolds stress and turbulent kinetic energy $-\langle uv\rangle \propto \frac{1}{2}\langle|\boldsymbol{u}|^2\rangle$, that provided them with a linear system to solve, between the momentum and the energy balance at the asymptotic limit of $\mathcal{W}e \to \infty$. They were able to demonstrate that the space-dependent viscosity model, with linear variation with the distance y from the wall, produces drag reduction (De Angelis et al., 2004). The simplicity of this model is attractive for predictive purposes of polymer drag reduced flows.

4.3.2 Elastic theory: A 'cascade theory' for drag reduction

The elastic theory was essentially developed under the notion of a Richardson - Kolmogorov cascade (Frisch, 1995) and the assumption of flow homogeneity (Tabor and de Gennes, 1986). De Gennes (1990) made also a transposition of this 'cascade theory' to wall-bounded turbulence to compare with Lumley's picture. The basic premise of elastic theory is that flexible polymer molecules in a turbulent flow behave elastically at high frequencies. The starting point of the theory is basically Lumley's time-criterion, where polymer stretching takes place only when a time scale $\tau_{r^*} \equiv (r^{*2}/\epsilon)^{1/3}$ of an inertial range length scale r^*, determined by the average dissipation rate of turbulent kinetic energy ϵ, matches τ_p. Note that through the time-criterion, τ_{r^*} depends on the number of monomers (see Eq. (4.1)), i.e. on molecular weight but not on concentration. When the time-criterion is satisfied, coils are assumed to be stretched partially by eddies of length scales $r < r^*$, with polymer elongation obeying the scaling power law

$$\lambda\!\!\!^{-}(r) \propto \left(\frac{r^*}{r}\right)^n \tag{4.32}$$

where the exponent n depends on the dimensionality of stretching, i.e. 1 and 2 in two and three physical dimensions, respectively. In addition, it was argued (De Gennes, 1990) that the elastic energy is

$$E_p \propto G\lambda\!\!\!^{-}(r)^{5/2} \tag{4.33}$$

with $G = c\kappa_B T/N$ having dimensions of an elastic modulus and all other symbols are defined in section 4.1. Then, going towards smaller scales, a cut-off scale r^{**}

exists given by the elastic limit[‖]

$$G\lambda(r^{**})^{5/2} \simeq \rho u_{r^{**}}^2 \tag{4.34}$$

which is the balance between elastic and turbulent kinetic energy at scale r^{**}. So, in the finite range of length scales $r^{**} < r < r^*$, polymers undergo affine deformations without significant reaction on the flow. This range is called the *passive range*, in the sense that polymers will follow passively the fluid element and will deform according to the power law Eq. (4.32).

Turning now the elastic theory into wall-bounded turbulence (De Gennes, 1990; Sreenivasan and White, 2000) and using the time-criterion $(r^{*2}(y)/\epsilon)^{1/3} = \tau_p$ and the classical scaling $\epsilon \propto u_\tau^3/y$ for the intermediate region $\delta_\nu \ll y \ll \delta$, one gets

$$r^*(y) \propto \left(\frac{\tau_p^3 u_\tau^3}{y}\right)^{1/2} \tag{4.35}$$

where r^* is now a function of the distance from the wall y due to the flow inhomogeneity. There is also an elastic limit as a function of y by combining Eq. (4.32), (4.34) and (4.35),

$$r^{**}(y) \propto \left(\frac{G}{\rho u_\tau^2}\frac{y}{\tau_p u_\tau}\right)^{\alpha} \left(\frac{\tau_p^3 u_\tau^3}{y}\right)^{1/2} \tag{4.36}$$

where the exponent $\alpha = (5n/2+2/3)^{-1}$ also depends on the dimensionality of stretching, as already mentioned for the exponent n in Eq. (4.32). This is a unique result, with no counterpart in Lumley's theory, where drag reduction was expected at arbitrarily low polymer concentration. Here, this cut-off scale depends on concentration through G. The schematic in Fig. 4.4 represents de Gennes picture of drag reduction in wall-bounded turbulence and depicts this dependence on c with the bold-dashed line representing the elastic limit with a reversed sign slope.

For concentrations below a certain threshold c_o, the elastic limit intersects the geometrical limit at $y < \delta_\nu$, where no macroscopic effects are expected. The onset of these effects take place at $c = c_o$, whose scaling can be obtained by setting $r^{**}(\delta_\nu) = \delta_\nu$. In the regime, $c_o < c < c^*$ drag reduction is expected and it is supposed that dissipation is reduced. As c increases, %DR increases steadily along with the

[‖]A scenario of strongly stretched chains was also considered by De Gennes (1990), with the elastic limit occurring at full stretching, suspecting severe chemical degradation.

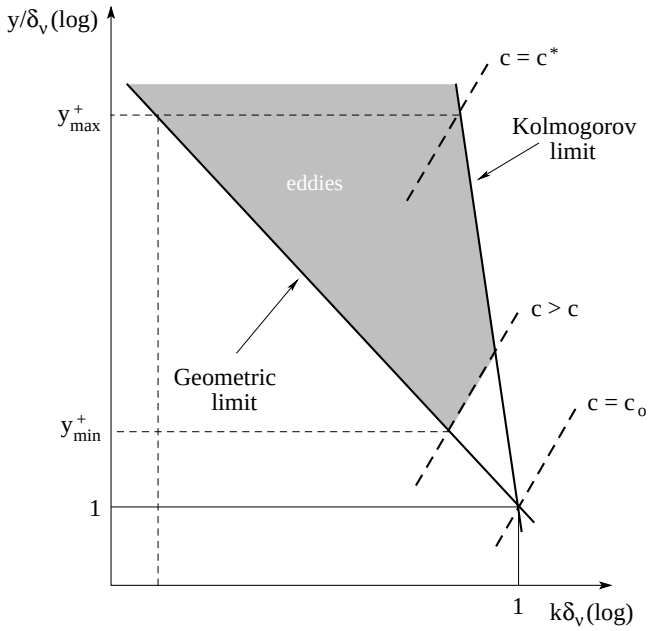

Figure 4.4: De Gennes' picture of drag reduction - Distribution of wave vectors k at various distances y from the wall.

buffer layer and the elastic limit shifts upwards (see Fig. 4.4). De Gennes (1990) argues that MDR occurs when $c = c^*$ (see Fig. 4.4), where neighbouring coils are in contact, so the concentration at this point can be specified as $c^* \simeq N/R_G^3$. In contrast, experimental data disputes this statement because concentrations below those needed for the overlap of polymer coils are observed to reach the MDR asymptote (Sreenivasan and White, 2000). Furthermore, it was claimed that the intersection of the elastic limit with the Kolmogorov limit when $c = c^*$ implies that the largest eddies do not satisfy anymore the time-criterion and therefore, $c > c^*$ will be less effective, giving in that way an explanation for the MDR law.

Even De Gennes (1990) himself mentions that his discussions are very conjectural, from the very beginning with a questionable existence of a power law for the elongation at different scales and with an unclear fate of the turbulent energy for scales $r < r^{**}$. Joseph (1990), however, speculates that scales below this cut-off behave elastically. Finally, Sreenivasan and White (2000) reconsidered the elastic theory, deriving some further scaling relations for the drag reduction onset and the MDR asymptote and compared them with experimental data. The conclusion, however, is that the elastic theory is tentative, as they also note and the issue is still open.

Chapter 5

Direct numerical simulation of viscoelastic turbulence

The recent development of numerical methods for viscoelastic turbulent flow computation has made it possible to investigate turbulent drag reduction in dilute polymer solutions using kinetic theory based models for polymer molecules. Here an overview of the existing methodologies to numerically solve the FENE-P model is given, emphasising the challenges and the need for high resolution shock capturing schemes (see section 5.1). With this in mind a state-of-the-art slope-limiter based method (Vaithianathan et al., 2006) was applied here to solve the FENE-P model with the aim of capturing the right magnitude of the polymer effect on the flow. Section 5.2 provides details on this high resolution scheme that was extended in this study to non-periodic boundary conditions and on the use of some effective linear algebra techniques, which led to the efficient numerical solution of the problem. In the end, this numerical method is validated with an analytical solution of the FENE-P model in section 5.3.

5.1 Overview

Numerical simulations allow a more detailed investigation of the mechanisms underlying the phenomenon of polymer drag reduction. The computationally demanding three-dimensional DNS makes a Lagrangian approach for the polymer prohibitive and also limits polymer models to simple representations (see section 4.1). A successful

model in turbulent drag reduction DNS studies is the FENE-P model, a constitutive equation in the Eulerian frame of reference (see Eqs. (4.22) and (4.23)), representing a conformation field of polymer macromolecules that have been modelled as elastic dumbbells (see section 4.2). This model is numerically solved in this work along with the Navier-Stokes equations to study turbulent drag reduction in a channel flow.

The conformation tensor $\boldsymbol{C}$ of the FENE-P model is a strictly positive definite (SPD) tensor, as already noted in section 4.2.1. It is well known that $\boldsymbol{C}$ should remain SPD as it evolves in time (Hulsen, 1990), otherwise, Hadamard instabilities* can grow due to the loss of the strictly positive definiteness of $\boldsymbol{C}$ by cumulative numerical errors that give rise to negative eigenvalues (Dupret and Marchal, 1986; Joseph and Saut, 1986). Until relatively recently, this was the main challenge for DNS of viscoelastic turbulence but Sureshkumar and Beris (1995), using spectral methods, introduced globally an artificial diffusion (GAD) term $\chi\partial_k\partial_k C_{ij}$ on the right hand side of Eq. (4.23), where χ is the dimensionless stress diffusivity, to overcome the Gibbs phenomenon (Peyret, 2002) and consequently Hadamard instabilities. On the other hand, Min et al. (2001) using finite differences, applied a second-order local artificial diffusion (LAD) term $\chi(\Delta x_k)^2\partial_k\partial_k C_{ij}$, where Δx_k is the local grid spacing in each k direction, only to locations where $\det(C_{ij}) < 0$. However, this is not a sufficient condition to guarantee the SPD property for the conformation tensor as it is discussed later in this chapter. Their reason for choosing a LAD rather than a GAD was based on visualisations showing more significant smearing of $\boldsymbol{C}$ gradients caused by GAD, which has also been confirmed from various investigators (Min et al., 2001; Dubief et al., 2005; Li et al., 2006).

In both methods the value of χ is not straightforward and its actual values are flow type dependent, so one has to conduct a parametric study on χ for each flow, otherwise numerical breakdowns are likely to occur (Sureshkumar and Beris, 1995; Min et al., 2001). Both approaches and slight variations thereof (Dubief et al., 2005; Li et al., 2006) continue to be in common use by most investigators. Note that generally, after several extensive parametric studies based on either GAD or LAD, only a few recent computational results (Li et al., 2006; Kim et al., 2007) are able

*Short wave instabilities, with growth rates which increase without bound as the wave length tends to zero. Such instabilities are a catastrophe for numerical analysis; the finer the grid, the worse the result. These instabilities arise in the study of an initial value problem for Laplace's equation. This is Hadamard's model of an ill-posed initial value problem (Joseph, 1990; Owens and Phillips, 2002).

to capture some of the salient features of the different drag reduction regimes (see section 4.3) observed experimentally. However, there are still a lot of divergent and misleading results (White and Mungal, 2008) because of the artificial term introduced in the governing equations.

The study by Jin and Collins (2007) stresses the fact that much finer grid resolutions are required to fully resolve the polymer field than for the velocity and pressure fields. Indeed, the hyperbolic nature of the FENE-P model Eq. (4.23) admits near discontinuities in the conformation and polymer stress fields (Joseph and Saut, 1986). Qualitatively similar problems occur with shock waves and their full resolution in gas dynamic compressible flows, which is not practical using finer grids. In this case, high resolution numerical schemes such as slope-limiter and Godunov-type methods (LeVeque, 2002) have proved successful at capturing the shock waves by accurately reproducing the Rankine-Hugoniot conditions across the discontinuity to ensure the correct propagation speed. Motivated by these schemes, Vaithianathan et al. (2006) adapted the second-order hyperbolic solver by Kurganov and Tadmor (2000), which guarantees that a positive scalar remains positive over all space, to satisfy the SPD property for the conformation tensor in the FENE-P model. It was demonstrated that this scheme dissipates less elastic energy than methods based on artificial diffusion, resulting in strong polymer-turbulence interactions (Vaithianathan et al., 2006). For this reason a modification of this method was developed in this present study to comply with non-periodic boundary conditions. The present peculiar discretisation scheme is described in section 5.2.1 along with some minor corrections to Vaithianathan et al. (2006) and further details on the numerical solution of the fully discretised form of the FENE-P model.

5.2 Numerical method

The set of parameters for the numerical solution of the governing equations for a turbulent channel flow with polymers is now reduced by introducing the following dimensionless variables

$$\frac{\boldsymbol{x}}{\delta} \rightarrow \boldsymbol{x}, \quad \frac{tU_c}{\delta} \rightarrow t, \quad \frac{\boldsymbol{u}}{U_c} \rightarrow \boldsymbol{u}, \quad \frac{p}{\rho U_c^2} \rightarrow p \tag{5.1}$$

given the channel half-width δ, the fluid density ρ and the centreline velocity of a fully developed laminar Poiseuille flow U_c. In these variables, the incompressible Navier-Stokes equations for a viscoelastic flow Eq. (4.4) become

$$\begin{aligned} \boldsymbol{\nabla}\cdot\boldsymbol{u} &= 0 \\ \partial_t\boldsymbol{u} + \frac{1}{2}\left[\boldsymbol{\nabla}(\boldsymbol{u}\otimes\boldsymbol{u}) + (\boldsymbol{u}\cdot\boldsymbol{\nabla})\boldsymbol{u}\right] &= -\boldsymbol{\nabla}p + \frac{\beta}{\mathcal{R}e_c}\boldsymbol{\Delta}\boldsymbol{u} + \boldsymbol{\nabla}\cdot\boldsymbol{\sigma}^{(p)} \end{aligned} \tag{5.2}$$

using the skew-symmetric form of the convection term (see appendix A.3), with the polymer stress tensor for FENE-P dumbbells Eqs. (4.21) and (4.22) turning to

$$\boldsymbol{\sigma}^{(p)} = \frac{1-\beta}{\mathcal{R}e_c\mathcal{W}e_c}\left(\frac{L_p^2-3}{L_p^2-tr\boldsymbol{C}}\boldsymbol{C}-\boldsymbol{I}\right) \tag{5.3}$$

where $\mathcal{R}e_c = U_c\delta/\nu$ and $We_c \equiv \tau_p U_c/\delta$ are the Reynolds and Weissenberg numbers, respectively, based on the centreline velocity and the channel's half-width. Moreover, non-dimensionalisation of the FENE-P model Eqs. (4.22) and (4.23) with the variables of Eq. (5.1) gives

$$\partial_t\boldsymbol{C} + (\boldsymbol{u}\cdot\boldsymbol{\nabla})\boldsymbol{C} = \boldsymbol{C}\cdot\boldsymbol{\nabla}\boldsymbol{u} + \boldsymbol{\nabla}\boldsymbol{u}^\top\cdot\boldsymbol{C} - \frac{1}{\mathcal{W}e_c}\left(\frac{L_p^2-3}{L_p^2-tr\boldsymbol{C}}\boldsymbol{C}-\boldsymbol{I}\right). \tag{5.4}$$

Note that the tilde symbol that denotes non-dimensional quantities (see section 4.2.1) has been dropped for convenience.

The next sections provide details only on the numerical aspects needed to compute these non-dimensional governing equations that differ from the treatment in Newtonian computations (see appendix A). The numerical method in appendix A was mostly maintained for Eqs. (5.2) apart from the time advancement (see section 5.2.2), which had to be changed because of the restrictive, for stability reasons, time discretisation of the FENE-P model. Note also that the polymer stress divergence in Eq. (5.2) and the velocity gradients in Eq. (5.4) were discretised with sixth-order compact finite difference schemes of Lele (1992) on a collocated grid (see appendix A.2). The gradient of the conformation tensor in the wall normal direction was evaluated using the grid stretching technique by Cain et al. (1984) and Avital et al. (2000) that maps an equally spaced co-ordinate in the computational space to a non-equally spaced co-ordinate in the physical space (see appendix A.6).

5.2.1 FENE-P solver

The numerical scheme developed by Vaithianathan et al. (2006) is based on the Kurganov and Tadmor (2000) scheme, as was mentioned in section 5.1. The main idea behind these high-resolution central schemes is the use of higher-order reconstructions, which enable the decrease of numerical dissipation so as to achieve higher resolution of shocks. In essence, they employ more precise information of the local propagation speeds. A key advantage of central schemes is that one avoids the intricate and time-consuming characteristic decompositions based on approximate Riemann solvers[†] (LeVeque, 2002). This is because these particular schemes realise the approximate solution in terms of its cell averages integrated over the Riemann fan (see Fig. 5.1).

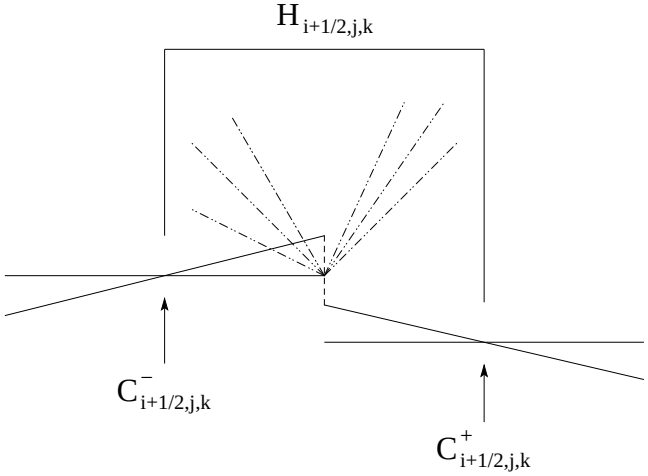

Figure 5.1: Central differencing approach – staggered integration over a local Riemann fan denoted by the dashed-double dotted lines.

Considering the discretisation of the convection term of the FENE-P model only in the x-direction, using the reconstruction illustrated in Fig. 5.1, the following second-order discretisation is obtained

$$\frac{\partial \boldsymbol{C}^n_{i,j,k}}{\partial x} = \frac{1}{\Delta x}(H^n_{i+1/2,j,k} - H^n_{i-1/2,j,k}) \tag{5.5}$$

[†]A numerical algorithm that solves the conservation law together with piecewise data having a single discontinuity

where

$$H^n_{i+1/2,j,k} = \frac{1}{2}u_{i+1/2,j,k}(\boldsymbol{C}^+_{i+1/2,j,k} + \boldsymbol{C}^-_{i+1/2,j,k}) - \frac{1}{2}|u_{i+1/2,j,k}|(\boldsymbol{C}^+_{i+1/2,j,k} - \boldsymbol{C}^-_{i+1/2,j,k}) \tag{5.6}$$

with

$$\boldsymbol{C}^{\pm}_{i+1/2,j,k} = \boldsymbol{C}^n_{i+1/2\pm1/2,j,k} \mp \frac{\Delta x}{2} \cdot \left.\frac{\partial \boldsymbol{C}}{\partial x}\right|^n_{i+1/2\pm1/2,j,k} \tag{5.7}$$

and

$$\left.\frac{\partial \boldsymbol{C}}{\partial x}\right|^n_{i,j,k} = \begin{cases} \frac{1}{\Delta x}(\boldsymbol{C}^n_{i+1,j,k} - \boldsymbol{C}^n_{i,j,k}) \\ \frac{1}{\Delta x}(\boldsymbol{C}^n_{i,j,k} - \boldsymbol{C}^n_{i-1,j,k}) \\ \frac{1}{2\Delta x}(\boldsymbol{C}^n_{i+1,j,k} - \boldsymbol{C}^n_{i-1,j,k}). \end{cases} \tag{5.8}$$

Similarly, Eqs. (5.6)-(5.8) can be rewritten for $H^n_{i-1/2,j,k}$. The appropriate choice of the derivative discretisation in Eq. (5.8) limits the slope so that the SPD property for $\boldsymbol{C}$ is satisfied. The SPD criterion for this choice is that all the eigenvalues of the conformation tensor should be positive, viz. $\lambda_i > 0$ and subsequently all its invariants (see Eqs. (2.63) replacing $\boldsymbol{\nabla u}$ with $\boldsymbol{C}$) should be positive for at least one of the discretisations. Note that just $\det(\boldsymbol{C}) > 0$, is not sufficient to guarantee the SPD property for the tensor (Strang, 1988). In case none of the options in Eq. (5.8) satisfy the criterion, then the derivative is set to zero reducing the scheme to first order locally in space. The proof for $\boldsymbol{C}$ being SPD using this numerical scheme can be found in Vaithianathan et al. (2006). The eigenvalues of the conformation tensor in this implementation are computed using Cardano's analytical solution (Press et al., 1996) for the cubic polynomial (see Eq. (2.62)) avoiding any complicated and time-consuming linear algebra matrix decompositions and inversions for just a 3×3 matrix. Ultimately, the advantage of this slope-limiter based method is that it adjusts in the vicinity of discontinuities so that the bounds on the eigenvalues cannot be violated, eliminating the instabilities that can arise in these types of calculations, without introducing a global stress diffusivity.

The complicated nature of the slope-limiting procedure raises difficulties in the case of wall boundaries for a channel flow computation, leading to loss of symmetry in the results. This had not been encountered by Vaithianathan et al. (2007), since they only considered periodic boundary conditions. So, the implementation

of the numerical method near the walls of the channel was modified for this study considering ghost nodes beyond the wall boundaries to keep the original formulation unaltered, preserving in that way the second-order accuracy at the boundaries. The values at the ghost nodes were linearly extrapolated from the interior solution (LeVeque, 2002), i.e.

$$\boldsymbol{C}^n_{i,j+1,k} = \boldsymbol{C}^n_{i,j,k} + (\boldsymbol{C}^n_{i,j,k} - \boldsymbol{C}^n_{i,j-1,k}) = 2\boldsymbol{C}^n_{i,j,k} - \boldsymbol{C}^n_{i,j-1,k}. \tag{5.9}$$

The time advancement is done simply using the forward Euler update, treating implicitly the stretching and the restoration term on the right hand side of Eq. (4.23) due to the potential finite extensibility of the polymer. Hence, the fully discretised form of the FENE-P model is

$$\begin{aligned}
\boldsymbol{C}^{n+1}_{i,j,k} = \boldsymbol{C}^n_{i,j,k} & \\
& - \frac{\Delta t}{\Delta x}(H^n_{i+1/2,j,k} - H^n_{i-1/2,j,k}) \\
& - \frac{\Delta t}{\Delta y_j}(H^n_{i,j+1/2,k} - H^n_{i,j-1/2,k}) \\
& - \frac{\Delta t}{\Delta z}(H^n_{i,j,k+1/2} - H^n_{i,j,k-1/2}) \\
& + \Delta t(\boldsymbol{C}^{n+1}_{i,j,k}\boldsymbol{\nabla}\boldsymbol{u}^n_{i,j,k} + \boldsymbol{\nabla}\boldsymbol{u}^{n^\top}_{i,j,k}\boldsymbol{C}^{n+1}_{i,j,k}) \\
& - \Delta t\left(\frac{1}{\mathcal{W}e_c} f(\boldsymbol{C}^{n+1}_{i,j,k})\boldsymbol{C}^{n+1}_{i,j,k} - \boldsymbol{I}\right)
\end{aligned} \tag{5.10}$$

with

$$\begin{aligned}
\boldsymbol{C}^n_{i,j,k} = \frac{1}{6}(&\boldsymbol{C}^-_{i+1/2,j,k} + \boldsymbol{C}^+_{i-1/2,j,k} \\
&+\boldsymbol{C}^-_{i,j+1/2,k} + \boldsymbol{C}^+_{i,j-1/2,k} \\
&+\boldsymbol{C}^-_{i,j,k+1/2} + \boldsymbol{C}^+_{i,j,k-1/2})
\end{aligned} \tag{5.11}$$

so that the convection term and the explicit term coming from the time derivative can be assembled in a convex sum

$$\boldsymbol{C}^* = \boldsymbol{C}^n_{i,j,k} + \frac{\partial \boldsymbol{C}^n_{i,j,k}}{\partial \boldsymbol{x}} = \sum_{l=1}^{N} s_l \boldsymbol{C}_l \tag{5.12}$$

where all coefficients $s_l \geq 0$ satisfy $\sum_{l=1}^{N} s_l = 1$, with $\boldsymbol{C}^*$ being SPD if the matrices $\boldsymbol{C}_l$ are SPD, ensuring the finite extensibility of the dumbbell, i.e. the trace of the conformation tensor is bounded $tr\boldsymbol{C} = \lambda_1 + \lambda_2 + \lambda_3 \leq L_P^2$ (Vaithianathan et al., 2006). The following CFL condition[‡] needs to be satisfied for the coefficients s_l to be non-negative

$$\text{CFL} = \max\left\{\frac{|u|}{\Delta x}, \frac{|v|}{\Delta y_{min}}, \frac{|w|}{\Delta z}\right\} \cdot \Delta t < \frac{1}{6} \tag{5.13}$$

and it also determines the time step Δt. Note that this CFL condition is more strict than the one for compact finite differences (Lele, 1992) used for Newtonian turbulence computations.

The numerical solution of Eq. (5.10) is carried out by first rewriting it in a Sylvester-Lyapunov form (Petersen and Pedersen, 2008), separating the implicit and explicit terms, i.e.

$$\boldsymbol{A}^\top \boldsymbol{X} + \boldsymbol{X}\boldsymbol{A} = \boldsymbol{B} \Rightarrow (\boldsymbol{I} \otimes \boldsymbol{A}^\top + \boldsymbol{A}^\top \otimes \boldsymbol{I})\boldsymbol{x} = \boldsymbol{b} \tag{5.14}$$

where $\boldsymbol{A} \equiv \frac{1}{2}[1 + f(\boldsymbol{C}_{i,j,k}^{n+1})\frac{\Delta t}{\mathcal{W}e_c}]\boldsymbol{I} - \Delta t \boldsymbol{\nabla}\boldsymbol{u}_{i,j,k}^n$, $\boldsymbol{X} \equiv \boldsymbol{C}_{i,j,k}^{n+1}$ and $\boldsymbol{B} \equiv \boldsymbol{C}^* + \frac{\Delta t}{\mathcal{W}e_c}\boldsymbol{I}$ are 3×3 matrices, $(\boldsymbol{I} \otimes \boldsymbol{A}^\top + \boldsymbol{A}^\top \otimes \boldsymbol{I})$ is a 9×9 matrix and $\boldsymbol{x} \equiv \text{vec}(\boldsymbol{X})$, $\boldsymbol{b} \equiv \text{vec}(\boldsymbol{B})$ are 9×1 vectors (see appendix C). The formula on the right hand side of Eq. (5.14) can be reduced from 9×9 to a 6×6 system of equations considering the symmetry of the conformation tensor. Note that Eq. (5.14) is nonlinear and can now be solved using conventional methods. In this study, the Newton-Raphson method for nonlinear systems was applied using the LU decomposition for the inversion of the Jacobian (Dennis and Schnabel, 1983; Press et al., 1996).

5.2.2 Time advancement

After obtaining the new update of the conformation tensor $\boldsymbol{C}_{i,j,k}^{n+1}$, the two-step (i.e. three time-level) second-order Adams-Bashforth/Trapezoidal scheme is used for the time integration of Eq. (5.2) through the following projection method (Peyret, 2002)

$$\frac{\boldsymbol{u}^* - \boldsymbol{u}^n}{\Delta t} = \frac{1}{2}(3\boldsymbol{F}^n - \boldsymbol{F}^{n-1}) + \frac{1}{2}(\boldsymbol{P}_{n+1}^* + \boldsymbol{P}^n) \tag{5.15}$$

[‡]Stability condition derived by Courant-Friedrichs-Lewy (Courant et al., 1967)

$$\frac{\boldsymbol{u}^{n+1} - \boldsymbol{u}^*}{\Delta t} = -\boldsymbol{\nabla}\tilde{p}^{n+1} \tag{5.16}$$

where

$$\boldsymbol{F} = -\frac{1}{2}\left[\boldsymbol{\nabla}(\boldsymbol{u}\otimes\boldsymbol{u}) + (\boldsymbol{u}\cdot\boldsymbol{\nabla})\boldsymbol{u}\right] + \frac{1}{\mathcal{R}e_c}\boldsymbol{\Delta u} \tag{5.17}$$

and

$$\boldsymbol{P} = \frac{1-\beta}{\mathcal{R}e_c\mathcal{W}e_c}\boldsymbol{\nabla}\cdot\left(\frac{L_p^2 - 3}{L_p^2 - tr\boldsymbol{C}}\boldsymbol{C} - \boldsymbol{I}\right) \tag{5.18}$$

with

$$\tilde{p}^{n+1} = \frac{1}{\Delta t}\int_{t_n}^{t_{n+1}} p\,dt. \tag{5.19}$$

The incompressibility condition $\boldsymbol{\nabla}\cdot\boldsymbol{u}^{n+1} = 0$ is verified by solving the Poisson equation

$$\boldsymbol{\nabla}\cdot\boldsymbol{\nabla}\tilde{p}^{n+1} = \frac{\boldsymbol{\nabla}\cdot\boldsymbol{u}^*}{\Delta t} \tag{5.20}$$

which is done in Fourier space (see appendix A.5). It is well known that these multistep methods are not self-starting and require a single-step method to provide the first time level (Peyret, 2002; LeVeque, 2007). In this study, explicit Euler was chosen for just the first iteration of these computations, viz. $\boldsymbol{u}^n = \boldsymbol{u}^{n-1} + \Delta t\boldsymbol{F}^{n-1}$.

5.3 Numerical validation with analytical solution

The numerical implementation of the FENE-P model is validated here by comparing the stationary numerical and analytical solution for a fully developed laminar Poiseuille flow between two parallel plates and velocity $\boldsymbol{u} = (1-(y-1)^2, 0, 0)\ \forall\, y \in [0,2]$. The stationary analytical solution of the FENE-P model for a steady unidirectional shear flow $\boldsymbol{u} = (U(y), 0, 0)$ can be easily obtained considering Eq. (5.4), which reduces to

$$0 = C_{i2}\partial_{x_2}u_i + C_{j2}\partial_{x_2}u_i - \frac{1}{\mathcal{W}e_c}(f(C_{kk})C_{ij} - \delta_{ij}) \tag{5.21}$$

where $f(C_{kk})$ is the Peterlin function (see Eq. (4.22)). Then, rewriting each component of the equation as follows taking into account the symmetry of C_{ij}

$$\begin{aligned} C_{11} &= \frac{1}{f(C_{kk})}\left(1+\frac{2\mathcal{W}e_c^2}{f^2(C_{kk})}\left(\frac{\mathrm{d}U}{\mathrm{d}y}\right)^2\right) \\ C_{12} &= \frac{\mathcal{W}e_c}{f^2(C_{kk})}\frac{\mathrm{d}U}{\mathrm{d}y} \\ C_{13} &= C_{23} = 0 \\ C_{22} &= C_{33} = \frac{1}{f(C_{kk})} \end{aligned} \tag{5.22}$$

and combining Eq. (4.22) with the trace C_{kk} determined by Eqs. (5.22), one gets

$$f(C_{kk}) = \frac{L_p^2-3}{L_p^2-C_{kk}} \Rightarrow L_p^2 f - \frac{2\mathcal{W}e_c^2}{f^2(C_{kk})}\left(\frac{\mathrm{d}U}{\mathrm{d}y}\right)^2 = L_p^2 \Rightarrow f^3 - f^2 - \Omega^2 = 0 \tag{5.23}$$

where $\Omega = \frac{\sqrt{2}\mathcal{W}e_c}{L_p}\frac{\mathrm{d}U}{\mathrm{d}y}$. The trigonometric solution (Birkhoff and Mac Lane, 1977) of this cubic polynomial is

$$f = \frac{2}{3}\cosh\frac{\phi}{3} + \frac{1}{3} \tag{5.24}$$

with $\phi = \cosh^{-1}\left(\frac{27}{2}\Omega^2+1\right)$. Ultimately, Eqs. (5.22) and (5.24) comprise the full analytical solution of the FENE-P model for any steady unidirectional flow with velocity $\boldsymbol{u} = (U(y),0,0)$. The required analytical solution for the fully developed laminar Poiseuille flow is determined by the velocity gradient, which in this case is $\mathrm{d}U/\mathrm{d}y = 2-2y \;\forall\, y \in [0,2]$.

The numerical parameters for the validation testcase are tabulated below and the velocity field was imposed to be $\boldsymbol{u} = (1-(y-1)^2,0,0) \;\forall\, y \in [0,2]$. The resolution in this laminar Poiseuille flow is important in the wall-normal direction y, so it was ensured that there are enough grid points to generate smooth profiles. The initial configuration of the conformation tensor was isotropic, i.e. $C_{ij} = \delta_{ij}$, which implies that the flow undergoes a transient for a certain time. The computation was marched far enough in time to obtain a fully developed steady state.

The numerical results are compared with the analytical solution in Figs. 5.2. In detail, both numerical and analytical profiles of the components of the conformation tensor are plotted together with the absolute error, defined by $error \equiv |C_{ij}^{anal} - C_{ij}^{num}|$,

$\mathcal{W}e_c$	L_p	$L_x \times L_y \times L_z$	$N_x \times N_y \times N_z$
5	120	$\pi\delta \times 2\delta \times \pi\delta$	$32 \times 65 \times 32$

Table 5.1: Parameters for the validation of the FENE-P model.

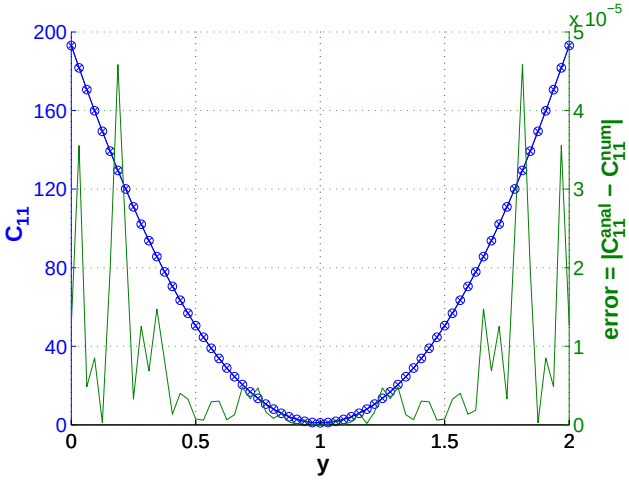

(a) C_{11} and its absolute error as functions of y

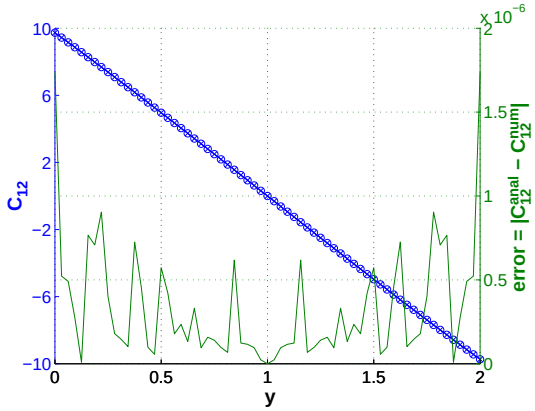

(b) C_{12} and its absolute error as functions of y

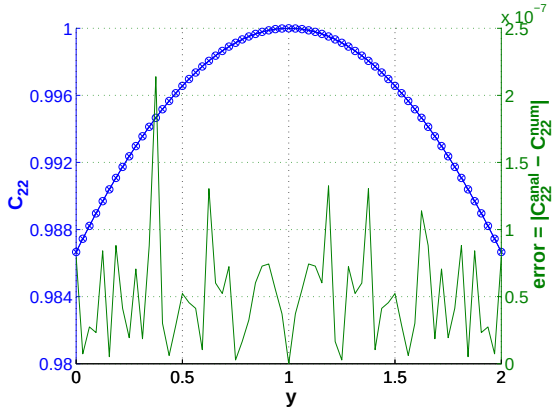

(c) $C_{22} = C_{33}$ and its absolute error as functions of y

Figure 5.2: Validation of the FENE-P model for an imposed laminar Poiseuille flow. $-\times$: analytical solution, $-\circ$: numerical solution, —: absolute error.

as functions of the distance y from the channel's walls. Here, only the components C_{11}, C_{12} and C_{22} are considered for illustration, since the numerical solution gives $C_{33} = C_{22}$ and $C_{13} = C_{23} = 0$ in agreement with the analytical solution. The absolute errors in the plots are very low, essentially denoting machine accuracy and

this is also obvious from the fact that the numerical and analytical profiles of C_{ij} are indistinguishable. The shear in the flow causes the stretching of the FENE-P dumbbells and most of it comes from near the walls (see Fig. 5.2), where the velocity gradient is the highest. The conformation tensor is strongly anisotropic, i.e. $C_{11} > C_{12} > C_{22}$, reflecting a persistent preferential alignment of the stretched polymers in the x direction with a slight inclination in the wall-normal direction y. This anisotropic behaviour resembles the behaviour of $\langle C_{ij} \rangle$ in turbulent channel flow, i.e. $\langle C_{11} \rangle > \langle C_{12} \rangle > \langle C_{22} \rangle$, as it will be shown in the next chapter.

Chapter 6

Polymer dynamics in viscoelastic turbulent channel flow

Recent progress in DNS of viscoelastic turbulence has begun to elucidate some of the dynamical interactions between polymers and turbulence, which are responsible for drag reduction. The aim in this chapter is to study polymer-induced turbulent drag reduction reproduced by numerical computations. The necessary details on the numerical parameters and procedures followed to perform DNS in viscoelastic turbulent channel flow using the FENE-P model are provided in section 6.1. Various viscoelastic turbulent statistics are analysed in section 6.2 for all the drag reduction regimes achieved in this study, with the novel numerical approach in wall-bounded flows for the FENE-P model described in chapter 5. Specifically, the effects of polymer extensibility and Reynolds number are briefly considered, whereas the statistics of mean velocity, fluctuating velocities and vorticities are examined in depth demonstrating that the current computations are closer to experimental observations than previous numerical studies. Section 6.3 presents extensively the conformation tensor statistics and the scaling of polymer stress tensor components at the high Weissenberg number limit, which assists in a new asymptotic result for the shear stress balance (see section 6.4). Finally, the polymer-turbulence interactions are studied in section 6.5 through the energy balance, where a refined and extended picture of a conceptual model for drag reduction based on viscoelastic dissipation is proposed (see section 6.6) before summing up the important results in section 6.7.

6.1 DNS of viscoelastic turbulent channel flow

Incompressible viscoelastic turbulence in a channel was simulated in a rectangular geometry (see Fig. 2.1) by numerically solving the non-dimensional Eqs. (5.2)-(5.4) in Cartesian co-ordinates employing the methodology of chapter 5. Periodic boundary conditions for $\boldsymbol{u} \equiv (u, v, w)$ are applied in the x and z homogeneous directions and no-slip boundary conditions at the walls (see Eq. (2.33)). The mean flow is in the x direction, i.e. $\langle \boldsymbol{u} \rangle = (\langle u(y) \rangle, 0, 0)$, where $\langle\ \rangle$ in this chapter denotes average in x, z spatial directions and time (see Eq. (3.3)). The bulk velocity U_b in the x direction was kept constant for all computations at all times by adjusting the mean pressure gradient $-\mathrm{d}\langle p \rangle / \mathrm{d}x$ at each time step. The choice of U_b in the computations for the Newtonian fluid is made based on Dean's formula $\mathcal{R}e_{\tau_0} \simeq 0.119 \mathcal{R}e_c^{7/8}$ (Dean, 1978; Lesieur, 1997) for a required $\mathcal{R}e_{\tau_0} \equiv \frac{u_{\tau_0}\delta}{\nu}$, where u_{τ_0} is the friction velocity for Newtonian fluid flow, i.e. $\beta = 1$ (see N cases in Table 6.1).

The procedure used for the computation of the viscoelastic turbulent channel flows of Table 6.1 is the following. First DNS of the Newtonian fluid, i.e. $\beta = 1$, were performed for the various Reynolds numbers until they reached a steady state. Then, the initial conditions for the viscoelastic DNS were these turbulent Newtonian velocity fields as well as Eqs. (5.22) and (5.24) for the C_{ij} tensor components, with $\frac{\mathrm{d}}{\mathrm{d}y}U = -6(y-1)^7$ given that $U(y) = 0.75(1-(y-1)^8)\ \forall\, y \in [0,2]$ is a close approximation to the averaged velocity profile of a Newtonian fully developed turbulent channel flow at moderate Reynolds numbers (Moin and Kim, 1980). Initially, the governing equations were integrated uncoupled, i.e. $\beta = 1$, until the conformation tensor achieved a stationary state. From then on the fully coupled system of equations, i.e. $\beta \neq 1$, was marched far in time, while $\boldsymbol{u}$ and $\boldsymbol{C}$ statistics were monitored for several successive time integrals until a fully developed steady state is reached, which satisfies the total shear stress balance across the channel, viz.

$$\frac{\beta}{\mathcal{R}e_c}\frac{\mathrm{d}\langle u \rangle}{\mathrm{d}y} - \langle uv \rangle + \langle \sigma_{12} \rangle = u_\tau^2 \left(1 - \frac{y}{\delta}\right) \tag{6.1}$$

where $\langle \sigma_{12} \rangle = \frac{1-\beta}{\mathcal{R}e_c \mathcal{W}e_c} \left\langle \frac{L_p^2 - 3}{L_p^2 - C_{kk}} C_{12} \right\rangle$ is the mean polymer shear stress, avoiding for convenience thereafter the superscript (p), which denotes the polymeric nature of the stress. Finally, after reaching a statistically steady state, statistics were collected for several decades of through-flow time scales L_x/U_b. In addition, existing turbulent

velocity and conformation tensor fields were restarted for computations where $\mathcal{W}e_c$ or L_p was modified. In these cases, the flow undergoes a transient time, where again sufficient statistics were collected after reaching a stationary state.

According to Eqs. (5.2)-(5.4), the four dimensionless groups that can fully characterise the velocity and the conformation tensor fields are $\mathcal{W}e_c$, L_p, β and $\mathcal{R}e_c$, and they are tabulated below. The main purpose of this study is to investigate the polymer dynamics and their influence on flow quantities in the different drag reduction regimes. Having that in mind, the reasons behind the choice of the particular parameter values is outlined below. The rationale here follows the thorough parametric study by Li et al. (2006).

Case	$\mathcal{W}e_c$	$\mathcal{W}e_{\tau_0}$	L_p	β	$\mathcal{R}e_c$	$\mathcal{R}e_\tau$	$L_x \times L_y \times L_z$	$N_x \times N_y \times N_z$	$\%DR$
N1	-	-	-	1	2750	123.8	$6.5\pi\delta \times 2\delta \times 1.5\pi\delta$	$200 \times 65 \times 100$	0
N2	-	-	-	1	4250	181	$4.5\pi\delta \times 2\delta \times \pi\delta$	$200 \times 97 \times 100$	0
N3	-	-	-	1	10400	392.6	$2\pi\delta \times 2\delta \times 0.5\pi\delta$	$200 \times 193 \times 100$	0
A	2	15.4	120	0.9	4250	167.7	$4.5\pi\delta \times 2\delta \times \pi\delta$	$200 \times 97 \times 100$	-14.2
B	4	30.8	120	0.9	4250	147.3	$4.5\pi\delta \times 2\delta \times \pi\delta$	$200 \times 97 \times 100$	-33.8
C	7	54	120	0.9	4250	121.8	$4.5\pi\delta \times 2\delta \times \pi\delta$	$200 \times 97 \times 100$	-54.7
D	9	69.4	120	0.9	4250	118.3	$4.5\pi\delta \times 2\delta \times \pi\delta$	$200 \times 97 \times 100$	-57.3
D1	9	69.4	60	0.9	4250	124.7	$4.5\pi\delta \times 2\delta \times \pi\delta$	$200 \times 97 \times 100$	-52.5
D2	9	69.4	30	0.9	4250	150.3	$4.5\pi\delta \times 2\delta \times \pi\delta$	$200 \times 97 \times 100$	-31
E	11	84.8	120	0.9	4250	113.3	$4.5\pi\delta \times 2\delta \times \pi\delta$	$200 \times 97 \times 100$	-60.8
F	13	100.2	120	0.9	4250	112.4	$4.5\pi\delta \times 2\delta \times \pi\delta$	$200 \times 97 \times 100$	-61.4
G	15	115.6	120	0.9	4250	111.4	$4.5\pi\delta \times 2\delta \times \pi\delta$	$200 \times 97 \times 100$	-62.1
H	17	131	120	0.9	4250	107.8	$8\pi\delta \times 2\delta \times \pi\delta$	$200 \times 97 \times 100$	-64.5
I	2	29.6	120	0.9	10400	323.3	$2\pi\delta \times 2\delta \times 0.5\pi\delta$	$200 \times 193 \times 100$	-32.2
J	4	22.3	120	0.9	2750	106.9	$6.5\pi\delta \times 2\delta \times 1.5\pi\delta$	$200 \times 65 \times 100$	-25.4
K	7	39	120	0.9	2750	91.1	$6.5\pi\delta \times 2\delta \times 1.5\pi\delta$	$200 \times 65 \times 100$	-45.9

Table 6.1: Parameters for the DNS of viscoelastic turbulent channel flow. The friction Weissenberg number is defined by $\mathcal{W}e_{\tau_0} \equiv \frac{\tau_p u_{\tau_0}^2}{\nu}$. LDR cases: A, B, D2, I, J; HDR cases: C, D, D1, E, F, G, K; MDR case: H.

Drag reduction effects are expected to be stronger at high Weissenberg numbers but also higher levels of $\%DR$ even at MDR have been measured for higher $\mathcal{R}e_\tau$ (Virk, 1975), showing the Reynolds number dependence on drag reduction amplitude. In this work, an extensive parametric study has been carried out by mainly varying $\mathcal{W}e_c$ for the computationally affordable $\mathcal{R}e_c = 4250$ to determine the impact of polymer dynamics on the extent of drag reduction. Note that the Weissenberg number is not a direct measure of the concentration which is the usual parameter

in drag reduction experiments, however, they are related through Eq. (4.1). The Reynolds numbers considered here, $\mathcal{R}e_c = 2750, 4250$ and 10400 which correspond to $\mathcal{R}e_{\tau_0} \simeq 125, 180$ and 395 respectively using Dean's formula, are small in comparison to most experimental studies but fall within the range of most DNS studies of polymer-induced turbulent drag reduction. Nevertheless, these Reynolds numbers are sufficiently large for the flow to be always turbulent and allow to study the dynamics of viscoelastic turbulence. Different maximum dumbbell lengths were also taken into account to check their effects for the same $\mathcal{W}e_c$ and $\mathcal{R}e_c$. The chosen $L_p^2 = b + 3$ values are representative of real polymer molecule extensibilities, which can be related through Eq. (4.16).

Low β values were used in most prior DNS to achieve high levels of drag reduction, in view of the attenuation of the polymer-turbulence interactions due to the additional artificial diffusion term in the FENE-P model and their low Reynolds numbers, usually $\mathcal{R}e_\tau \leq 395$. In fact, values as low as $\beta = 0.4$ have been applied amplifying viscoelastic effects to reach the HDR regime (Ptasinski et al., 2003). However, such low β values may lead to significant shear-thinning* (Joseph, 1990) unlike in experiments of polymer drag reduction. The fact that the current numerical scheme for the FENE-P model (see section 5.2.1) is expected to provide stronger polymer-turbulence interactions allows the value of β, which is inversely proportional to the polymer concentration, to be high in this study, i.e. $\beta = 0.9$, representative of dilute polymer solutions used in experiments.

The box sizes $L_x \times L_y \times L_z$, where subscripts indicate the three Cartesian coordinates (see Fig. 2.1), were chosen with reference to the systematic study by Li et al. (2006) on how the domain size influences the numerical accuracy. In detail, they point out that long boxes are required in DNS of polymer drag reduction, particularly in the streamwise direction because of longer streamwise correlations at higher $\%DR$, as opposed to the minimal flow unit (Jiménez and Moin, 1991) used in many earlier works. Different grid resolutions $N_x \times N_y \times N_z$ were tested for convergence. In particular, the following set of resolutions $128 \times 65 \times 64$, $200 \times 97 \times 100$ and $256 \times 129 \times 128$ were tried for $\mathcal{R}e_{\tau_0} \simeq 180$ with the two latter giving identical mean velocity profiles and not significantly different rms velocity and vorticity profiles. Similar, grid sensitivity tests were carried out for the other $\mathcal{R}e_{\tau_0}$ cases. Eventually, the sufficient

*the shear stress increases slower than linear $\sigma_{12} \propto S_{12}$

resolutions for each Newtonian fluid computation were validated against previously published databases for the corresponding $\mathcal{R}e_{\tau_0}$ cases (Moser et al., 1999; Iwamoto et al., 2002; Hu et al., 2006). Note that if the resolutions for Newtonian turbulent computations are adequately resolving the flow scales, then the same resolutions are sufficient for viscoelastic turbulent computations, since the size of vortex filaments in these flows increases while their number decreases as drag reduces (White and Mungal, 2008).

For a given resolution, viscoelastic computations require approximately 4 times more memory and 2 times more CPU time per time step compared to the Newtonian case. The time step Δt used in viscoelastic computations is typically a factor of 5 smaller than that used in the Newtonian cases due to the stricter CFL condition of the present numerical method for the FENE-P model (see Eq. (5.13) and (Lele, 1992) for more details on the time step constraint using compact schemes). Ultimately, the viscoelastic computations require approximately 10 times more CPU resources than the Newtonian computations for a given computational time period.

6.2 Viscoelastic turbulence statistics

6.2.1 Polymer drag reduction

Since the computations are performed with a constant flow rate by adjusting the pressure gradient, $\%DR$ is manifested via a decrease in skin friction, i.e. lower $\mathcal{R}e_\tau$ values, defined by Eq. (4.28). Figure 6.1 depicts the capability of the current numerical scheme used for the FENE-P model to enable stronger polymer-turbulence interactions than artificial diffusion methods. Higher values of percentage drag reduction as function of Weissenberg number are obtained comparing with earlier DNS studies without the need for their low β values (see e.g. Fig. 1b in Min et al. (2003a) or Table 1 in Ptasinski et al. (2003)). These $\%DR$ values extend throughout the drag reduction regimes (see Fig. 6.1), based on Warholic et al. (1999) classification of drag reduction (see also section 4.3). The MDR limit is approached in this case at $|\%DR| \simeq 65$ because of the moderate $\mathcal{R}e_c$ in these computations. Even so, this amount of drag reduction falls within the MDR regime, allowing to study the MDR dynamics of the polymer molecules and their effects on the flow in this asymptotic state.

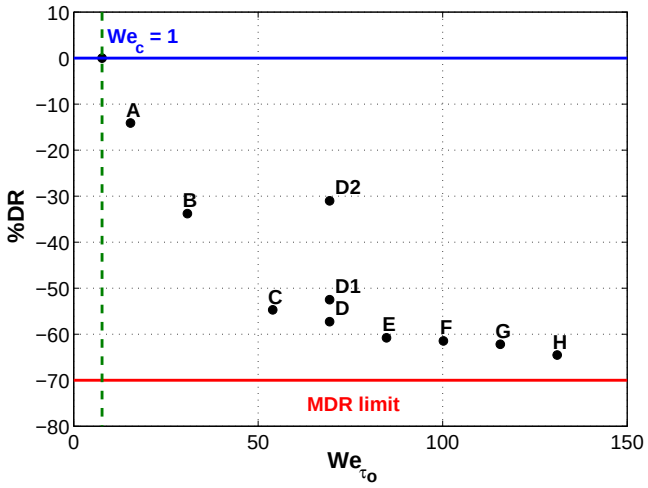

Figure 6.1: Variation of percentage drag reduction with Weissenberg number.

6.2.2 Effects of polymer extensibility and Reynolds number

The effects of maximum dumbbell extensibility is briefly considered for three different extensibilities $L_p = 30, 60$ and 120 for the same $\mathcal{W}e_c$ and $\mathcal{R}e_c$ (see D cases in Table 6.1). Figure 6.1 shows that the extent of drag reduction is amplified by longer polymer chains consistent with other DNS studies (Dimitropoulos et al., 1998; Li et al., 2006). This effect is related to the fact that the average actual length of the dumbbells, represented by the trace of the conformation tensor $\langle C_{kk} \rangle$, increases further for larger L_p according to Fig. 6.2a, inducing stronger influence of the polymers on the flow. The percentage increase, however, of the polymers extension is less for larger FENE-P dumbbells (see Fig. 6.2b), suggesting that large polymer molecules could be less susceptible to chain scission degradation[†], which causes loss of drag reduction in experiments (White and Mungal, 2008). The near-wall turbulence dynamics play an important role for all three cases, as most of the stretching happens near the wall, where the highest fluctuating strain rates are expected. Eventually, the largest maximum length, i.e. $L_p = 120$, was used for the rest of the computations considered in this work in order to explore the polymer dynamics at effective drag reductions, which are interesting not only fundamentally but also in many real life applications.

Based on DNS using the GAD methodology (see section 5.1), Housiadas and

[†]The degradation of polymers by breakage of the chemical bonds forming smaller molecules.

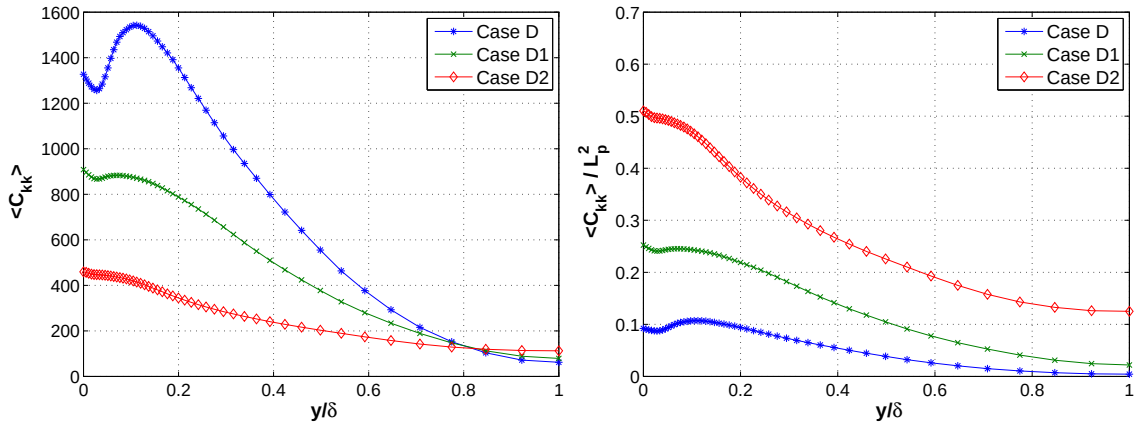

(a) $\langle C_{kk} \rangle$ with respect to y/δ (b) $\langle C_{kk} \rangle / L_p^2$ with respect to y/δ

Figure 6.2: Effect of maximum dumbbell length. Plots of (a) average actual dumbbell extensibility and (b) percentage average dumbbell extensibility as functions of y/δ.

Beris (2003) claim that the extent of drag reduction is rather insensitive to Reynolds numbers ranging between $125 \leq \mathcal{R}e_{\tau_0} \leq 590$ for LDR flows. On the other hand, avoiding the use of artificial diffusion in this study, the Reynolds number dependence on drag reduction for cases with identical $\mathcal{W}e_c$ values but different Reynolds numbers, i.e. $\mathcal{R}e_c = 2750, 4250$ and 10400, is obvious by comparing $\%DR$ of case A with I and case B with J (LDR regime), as well as case C with K (HDR regime), where the $\%DR$ increases for higher $\mathcal{R}e_c$ at all instances (see Table 6.1). This Reynolds number dependence is further depicted in the polymer dynamics of viscoelastic turbulence through the profiles of $\langle C_{kk} \rangle / L_p^2$ in Fig. 6.3, which amplify closer to the wall, due to more intense strain rates in this region at increasing $\mathcal{R}e_c$ and collapse towards the centre of the channel. The disparate behaviour of $\langle C_{kk} \rangle$ with respect to y/δ due to the Reynolds number dependence is anticipated by the broader spectra of flow time scales that are encountered at higher $\mathcal{R}e_c$ by the dumbbells with fixed relaxation time scale. As a final comment, the fact that the current DNS could capture the Reynolds number dependence on drag reduction and polymer dynamics, emphasises once more the strong polymer-turbulence interactions that can be attained by the present numerical approach even at low levels of drag reduction.

It is essential to note at this point that the intermediate dynamics between the von Kármán and the MDR law, i.e. the LDR and HDR regimes (see section 4.3), are non-universal because they depend on polymer concentration, chemical characteristics of

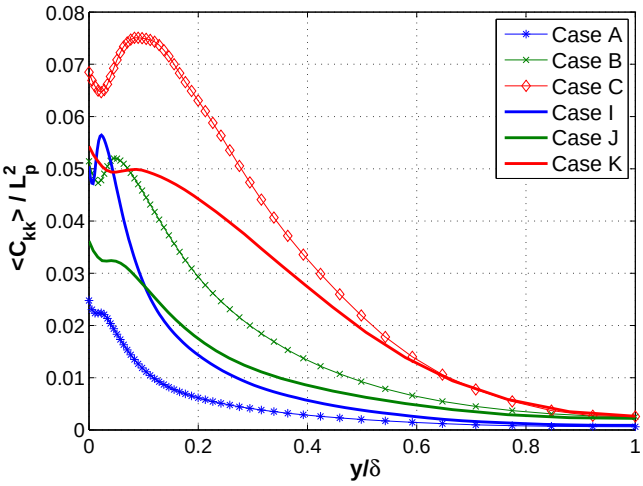

Figure 6.3: Effect of Reynolds number on percentage average dumbbell extensibility as function of y/δ. Identical colours correspond to cases with the same $\mathcal{W}e_c$ values.

polymers, Reynolds number, etc. (Virk, 1975; Procaccia et al., 2008). Here, this is illustrated by the maximum dumbbell length and Reynolds number dependencies of the polymer dynamics in Figs. 6.2 and 6.3, respectively. However, at the MDR limit, which is achieved at $\mathcal{W}e_c \gg 1$ and $\mathcal{R}e_c \gg 1$, the dynamics are known to be universal (Virk, 1975; Procaccia et al., 2008), i.e. independent of polymer and flow conditions.

6.2.3 Mean and fluctuating velocity statistics

The picture of drag reduction can be analysed in further detail with the statistics of the turbulent velocity field introduced in Fig. 6.4. The distinct differences in the statistical trends of the turbulent velocity field between the LDR and HDR regime, that have been observed experimentally (Warholic et al., 1999; Ptasinski et al., 2001), are clearly identified in these results. For clarity, a few indicative cases from the data of Table 6.1 have been chosen for plotting, representing the LDR, HDR and MDR regimes for different Weissenberg numbers at $\mathcal{R}e_c = 4250$.

According to Fig. 6.4a and noting that $\beta = 0.9$ for all viscoelastic cases, all mean velocity profiles collapse in the viscous sublayer $y_+ \lesssim 10$ to the linear variation $U_+ = \beta^{-1} y_+$, which can be deduced for viscoelastic flows by rewriting Eq. (6.1) in viscous scales

$$\beta \frac{\mathrm{d}U_+}{\mathrm{d}y_+} - \frac{\langle uv \rangle}{u_\tau^2} + \frac{\langle \sigma_{12} \rangle}{u_\tau^2} = 1 - \frac{y_+}{\mathcal{R}e_\tau} \tag{6.2}$$

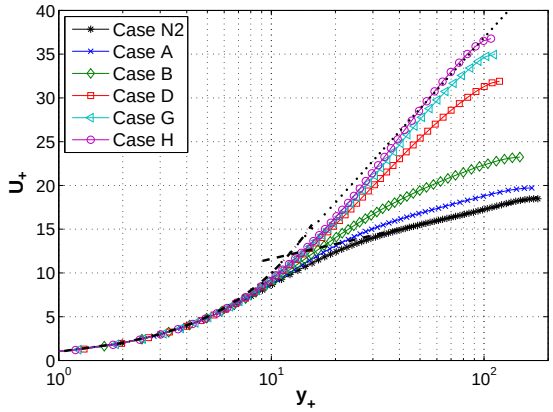

(a) Mean velocity profiles versus y_+. $-\cdot-$: $U_+ = y_+$, - - -: $U_+ = \frac{1}{0.41}\log y_+ + 6.0$, $\cdots$: $U_+ = \frac{1}{11.7}\log y_+ - 17$

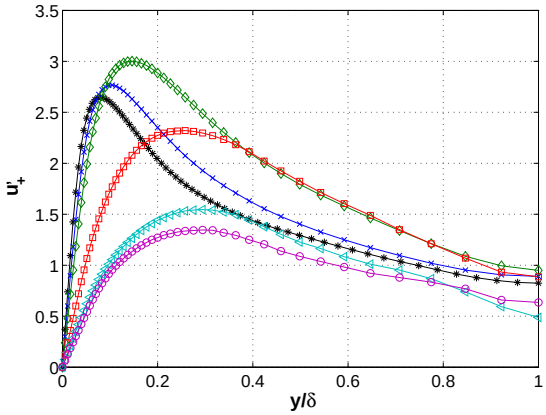

(b) Steamwise rms velocity profiles versus y/δ

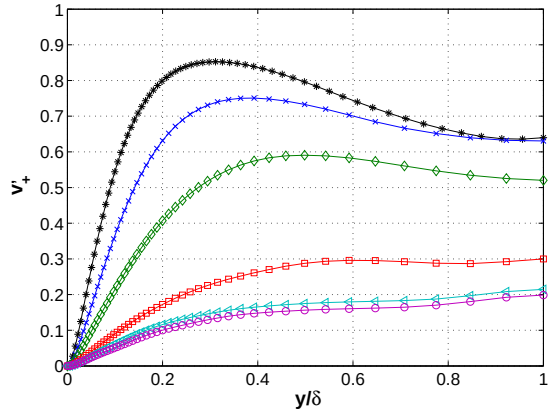

(c) Wall-normal rms velocity profiles versus y/δ

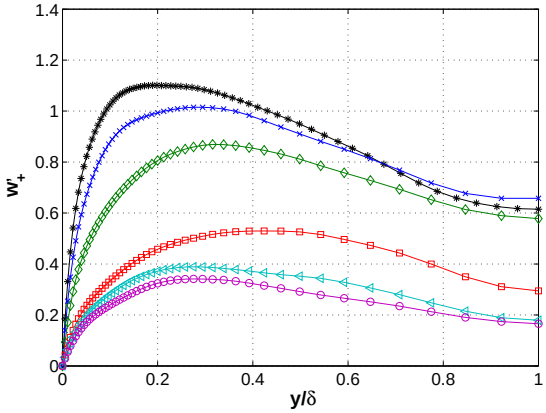

(d) Spanwise rms velocity profiles versus y/δ

Figure 6.4: Mean and rms velocity profiles for the LDR, HDR and MDR regimes.

and neglecting the normalised Reynolds and mean polymer shear stress in the viscous sublayer $y_+ \to 0$ (see also section 6.4). Figure 6.4a presents the clear impact of $\%DR$ on the mean flow with the skin friction decreasing and the mean velocity increasing away from the wall in comparison to the Newtonian case N2 as a result of higher $\mathcal{W}e_c$ values at the same $\mathcal{R}e_c$. The profile of the Newtonian case N2 is in agreement with the von Kármán law Eq. (2.49), which does not hold for viscoelastic turbulent flows. Specifically, the curves of cases A and B (LDR regime) are shifted upwards with higher values of the intercept constant B, i.e. parallel to the profile of the Newtonian flow (see Fig. 6.4a), increasing $\%DR$. This picture is consistent with the phenomenological description by Lumley (1969, 1973), where the upward shift of the inertial sublayer can be interpreted as a thickening of the buffer or elastic

layer for viscoelastic flows, which is equivalent to drag reduction. HDR cases D and G exhibit different statistical behaviour than LDR flows with the slope of the log-region increasing until the MDR asymptote is reached by case H. Overall, the same behaviour across the extent of drag reduction in viscoelastic turbulent flows have been seen in several experimental and numerical results (White and Mungal, 2008).

Different statistical trends between low and high drag reduction have also been observed experimentally (see Figs. 4 and 11 in Warholic et al. (1999) and Fig. 5 in Ptasinski et al. (2001)) for the rms streamwise velocity fluctuations normalised with u_τ. Figure 6.4b illustrates the growth of the peak in the profile of u'_+ for LDR case A and B at low $\mathcal{W}e_c$ and a notable decrease for the rest of the cases at HDR/MDR with high $\mathcal{W}e_c$ values. The peaks move monotonically away from the wall throughout the drag reduction regimes indicating the thickening of the elastic layer, which is compatible with that of the mean velocity profile.

Note that this is the first time that a DNS computation can so distinctly attain this behaviour. This is attributed to the accurate shock-capturing numerical scheme applied for the FENE-P model in this study. It has to be mentioned however that there have been three earlier studies (Min et al., 2003a; Ptasinski et al., 2003; Dubief et al., 2004), which use the artificial diffusion algorithms for FENE-P and showed similar but not as clear trends for u'_+ in a DNS of viscoelastic turbulent channel flow. In fact, Min et al. (2003a) reached the HDR/MDR regime at roughly $|\%DR| \simeq 40$, clearly very low to afford the correct dynamics and Ptasinski et al. (2003) had to use $\beta = 0.4$ to approach HDR/MDR, encountering considerable shear-thinning effects. It is interesting to mention that other recent studies (Handler et al., 2006; Li et al., 2006), using the artificial diffusion methodology, with more extensive Weissenberg number data and high β values, have not been able to obtain this transition effect on the statistics of u'_+ between the drag reduction regimes.

Finally, the wall-normal v'_+ and spanwise w'_+ rms velocity fluctuations in Figs. 6.4c and 6.4d, respectively, are continuously attenuated while $\%DR$ is enhanced by increasing the polymer relaxation time scale. Again, the monotonic displacement of their peaks towards the centre of the channel as drag reduction amplifies is consistent with that of the mean velocity profile and with experimental and other numerical studies (White and Mungal, 2008).

6.2.4 Fluctuating vorticity statistics

The rms statistics of the fluctuating vorticity field normalised by viscous scales, i.e. $\boldsymbol{\omega}'_+ \equiv \boldsymbol{\omega}'\delta_\nu/u_\tau$, are presented in Fig. 6.5 for representative cases from Table 6.1 at various levels of drag reduction. The streamwise vorticity fluctuations ω'_{x_+} demon-

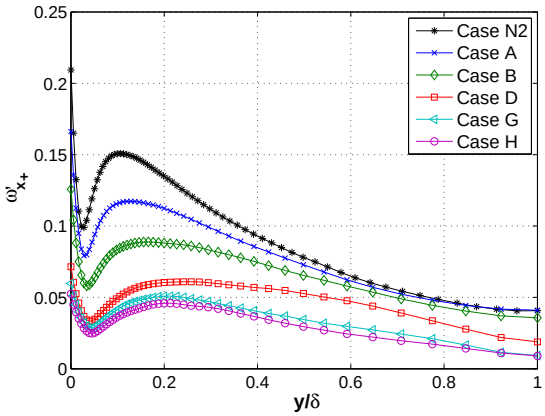

(a) Steamwise rms vorticity profiles versus y/δ

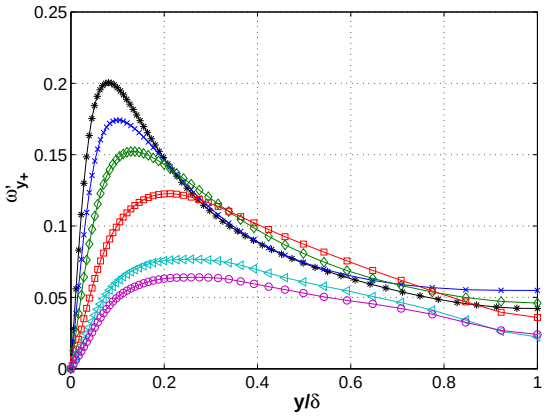

(b) Wall-normal rms vorticity profiles versus y/δ

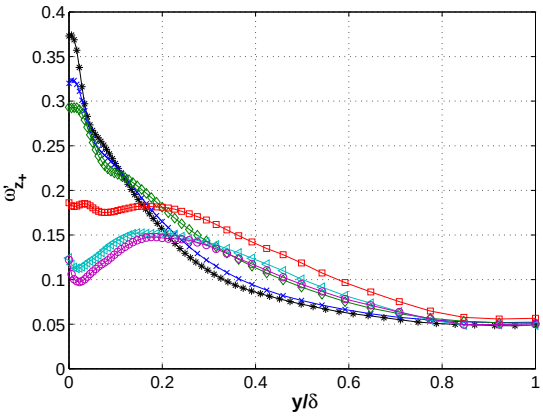

(c) Spanwise rms vorticity profiles versus y/δ

Figure 6.5: Rms vorticity profiles for the LDR, HDR and MDR regimes.

strate a persistent attenuation along the normalised distance y/δ as drag reduction enhances due to the increase of $\mathcal{W}e_c$ (see Fig. 6.5a). In the near-wall region $y/\delta < 0.2$ of Fig. 6.5a there is a characteristic local minimum and maximum that could be interpreted to correspond to the average edge and centre of the streamwise vortices, respectively (Kim et al., 1987; Li et al., 2006). Then, the average size of these large streamwise vortices is roughly equal to the distance between these two peaks. The fact that these peaks are displaced away from each other and at the same time away from the wall, as $\%DR$ builds up, implies an increase in the average size of the

streamwise vortices and a thickening of the buffer layer, respectively, in agreement with earlier works (Sureshkumar et al., 1997; Li et al., 2006; Kim et al., 2007; White and Mungal, 2008). The attenuation in the intensity of ω'_{x_+} provides evidence for a drag reduction mechanism based on the suppression of the near-wall counter-rotating steamwise vortices (Kim et al., 2007, 2008), which underpin considerable amount of the turbulence production (Kim et al., 1971).

The wall-normal rms vorticity is zero at the wall due to the no-slip boundary condition and reaches its peak within the buffer layer (see Fig. 6.5b). The intensity of ω'_{y_+} is reduced for all levels of drag reduction according to Fig. 6.5b, with the position of the near-wall peaks moving towards the centre of the channel as $\mathcal{W}e_c$ becomes larger, representing once more the thickening of the elastic layer in a consistent way. Most of the inhibition of ω'_{y_+} happens near the wall and slightly towards the centre of the channel only for the HDR/MDR cases G and H, i.e. for $|\%DR| > 60$.

Figure 6.5c shows a more interesting behaviour for ω'_{z_+}, where the spanwise vorticity fluctuations decrease in the near-wall region $y/\delta \lesssim 0.2$ and increase further away while drag reduces. This effect may be related to the transitional behaviour of u'_+ between the LDR and HDR/MDR regimes (see Fig. 6.4b) plus the continuous drop of v'_+ (see Fig. 6.4c) in viscoelastic drag reduced flows. As a final note, $\omega'_{z_+} > \omega'_{x_+} > \omega'_{y_+}$ in the viscous sublayer, i.e. $y/\delta < 0.05$ for all cases and $\omega'_{z_+} \simeq \omega'_{x_+} \simeq \omega'_{y_+}$ in the inertial and outer layer for the Newtonian case N2. However, $\omega'_{z_+} > \omega'_{y_+} > \omega'_{x_+}$ away from the wall when drag reduces for viscoelastic flows, which manifests the dominance of anisotropy in the inertial and outer layer at HDR and MDR.

6.3 Conformation and polymer stress tensor

Before looking at the mean momentum and energy balance, the study of the conformation tensor field is essential to get an understanding of the polymer dynamics in support of the results provided by this new numerical method for the FENE-P model in turbulent channel flow. The symmetries in the flow geometry determine properties of tensor components in the average sense (Pope, 2000). In the current DNS of turbulent channel flow, statistics are independent of the z direction and the flow is also statistically invariant under reflections of the z co-ordinate axis. Therefore, for the probability density function $f(\boldsymbol{Q}; \boldsymbol{x}, t)$ of a vector $\boldsymbol{Q}$, these two conditions imply $\partial f/\partial z = 0$ and $f(Q_1, Q_2, Q_3; x, y, z, t) = f(Q_1, Q_2, -Q_3; x, y, -z, t)$. Then, at $z = 0$

reflectional symmetry suggests that $\langle Q_3 \rangle = -\langle Q_3 \rangle \Rightarrow \langle Q_3 \rangle = 0$ and similarly for $\langle Q_1 Q_3 \rangle = \langle Q_2 Q_3 \rangle = 0$. So, in this case the mean conformation tensor reduces to

$$\langle C_{ij} \rangle = \begin{pmatrix} \langle C_{11} \rangle & \langle C_{12} \rangle & 0 \\ \langle C_{12} \rangle & \langle C_{22} \rangle & 0 \\ 0 & 0 & \langle C_{33} \rangle \end{pmatrix} \tag{6.3}$$

where the non-zero components normalised with L_p are presented in Fig. 6.6 with respect to y/δ for cases at various drag reduction regimes (see Table 6.1). In this study, the zero components have been found to be zero within the machine accuracy. Turbulent channel flow is also statistically symmetric about the plane $y = \delta$. Therefore, this reflectional symmetry imposes $f(Q_1, Q_2, Q_3; x, y, z, t) = f(Q_1, -Q_2, Q_3; x, -y, z, t)$, which implies that the normal components of $\langle C_{ij} \rangle$ are even functions and $\langle C_{12} \rangle$ is an odd function comparable to the Reynolds stress tensor components.

The normalised trace of the mean conformation tensor $\langle C_{kk} \rangle / L_p^2$ is plotted in Fig. 6.6a together with $\langle C_{11} \rangle / L_p^2$. Notice that the dominant contribution in the trace comes from $\langle C_{11} \rangle$, i.e. $\langle C_{kk} \rangle \simeq \langle C_{11} \rangle$ at all Weissenberg numbers, reflecting on average a strong preferential orientation of the stretched dumbbells along the streamwise direction. The fact that $\langle C_{11} \rangle \gg \langle C_{12} \rangle \simeq \langle C_{33} \rangle > \langle C_{22} \rangle$ denotes the strong anisotropic behaviour of the mean conformation tensor caused by the mean shear in turbulent channel flow. This anisotropy influences the statistics of the fluctuating velocity field particularly at small scales, as was mentioned in section 6.2.4 for the vorticity fluctuations. The curves of $\langle C_{11} \rangle / L_p^2$ and consequently of $\langle C_{kk} \rangle / L_p^2$ constantly rise with most of the stretching happening close to the wall and growing towards the centre of the channel, since higher values of polymer time scale are influenced from a wider spectrum of flow time scales. A local minimum and a maximum emerge in the near-wall region $y/\delta < 0.2$, induced by the streamwise vortices (Dubief et al., 2004; Dimitropoulos et al., 2005). These peaks move apart from each other and away from the wall for higher $\mathcal{W}e_c$ values. Figure 6.6a also shows that the amplitudes of these peaks seem inversely proportional to the peak amplitudes of ω'_{x_+} as drag reduces (see also Fig. 6.5a).

Moreover, as $\mathcal{W}e_c$ increases the profiles of $\langle C_{12} \rangle / L_p^2$ and $\langle C_{33} \rangle / L_p^2$ amplify, reaching their peaks at not much different y/δ for each $\mathcal{W}e_c$ case (see Figs. 6.6b and 6.6d). In particular, the values of $\langle C_{12} \rangle / L_p^2$ at the wall are dependent on the polymer re-

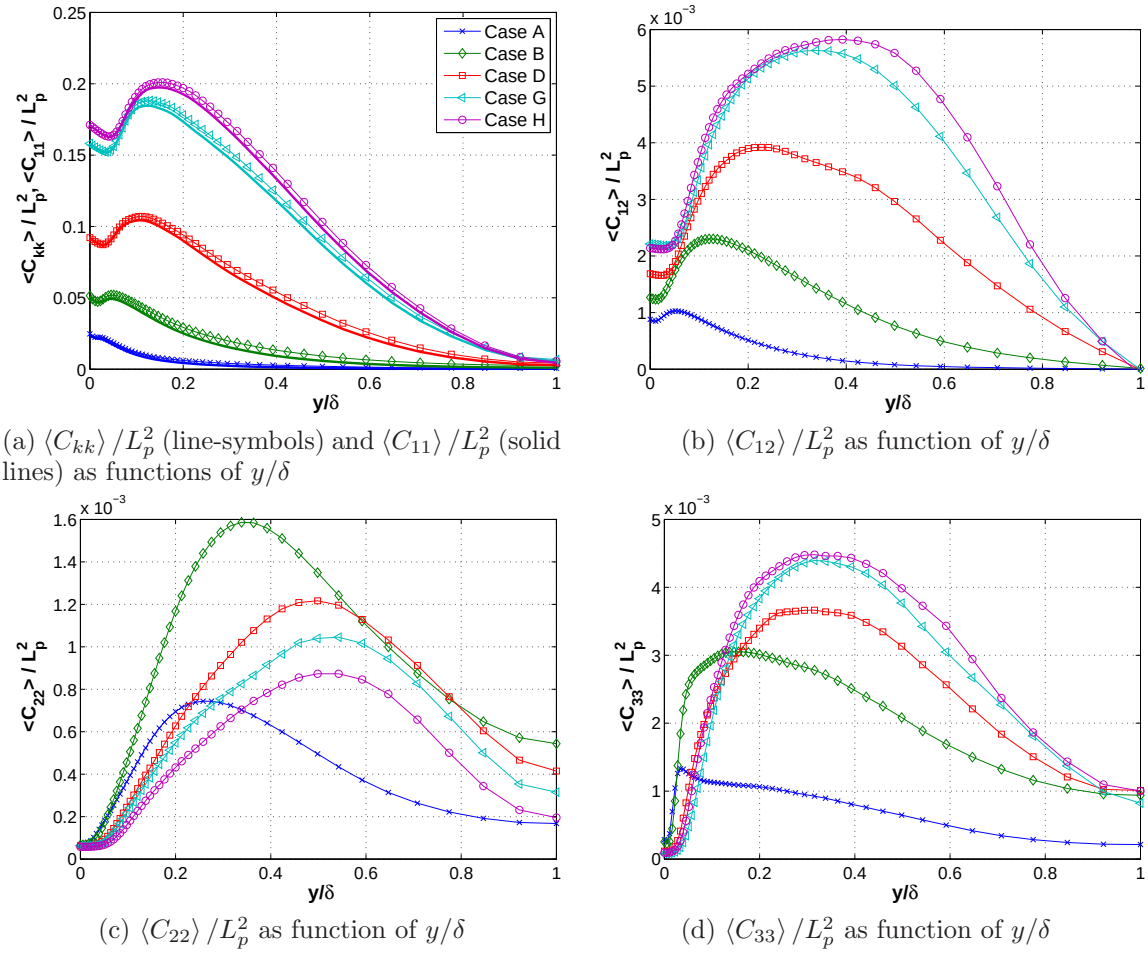

(a) $\langle C_{kk} \rangle / L_p^2$ (line-symbols) and $\langle C_{11} \rangle / L_p^2$ (solid lines) as functions of y/δ

(b) $\langle C_{12} \rangle / L_p^2$ as function of y/δ

(c) $\langle C_{22} \rangle / L_p^2$ as function of y/δ

(d) $\langle C_{33} \rangle / L_p^2$ as function of y/δ

Figure 6.6: Profiles of the mean conformation tensor components for the LDR, HDR and MDR regimes.

laxation time scale unlike for $\langle C_{33} \rangle / L_p^2$. On the other hand, the values of $\langle C_{33} \rangle / L_p^2$ depend on Weissenberg number at $y = \delta$ in contrast to $\langle C_{12} \rangle / L_p^2$, which is zero for all cases because of the symmetry mentioned above. The behaviour of $\langle C_{22} \rangle / L_p^2$ in Fig. 6.6c is more peculiar with respect to $\mathcal{W}e_c$, with the profiles increasing within the LDR regime and attenuate for HDR and MDR cases, in a similar manner to u'_+ (see Fig. 6.4b). Its peak values are achieved closer to the core of the channel in comparison to the rest of the conformation tensor components. This points out the different flow time scales that are important for $\langle C_{22} \rangle$, exemplifying the complex dynamics of the polymers, even in this simple mechanical model.

It is interesting to mention that the components of $\langle C_{ij} \rangle$ have different asymptotic rates of convergence towards the limit $\mathcal{W}e_c \to \infty$. It is known that for $\mathcal{W}e_c \gg 1$ the

upper bound for the trace is $\langle C_{kk} \rangle \leq L_p^2$ and subsequently in this case $\langle C_{11} \rangle \lesssim L_p^2$ (see Fig. 6.6a), where this upper bound is far from achieved in these computations. This result demonstrates that highly stretched polymers are not required for the manifestation of drag reduction or even of the MDR asymptote, as De Gennes (1990) claims against Lumley's assumption of a coil-stretch transition (Lumley, 1969), i.e. highly stretched polymer molecules, for the enhancement of intrinsic viscosity (see section 4.3). The components $\langle C_{12} \rangle / L_p^2$ and $\langle C_{33} \rangle / L_p^2$ seem to have almost reached their asymptotic limit with the MDR case H according to Figs. 6.6b and 6.6d, respectively. Finally, $\langle C_{22} \rangle / L_p^2$ has not yet converged to its limit, decreasing with a slow rate towards very small values for high $\mathcal{W}e_c$. In fact, L'vov et al. (2005); Procaccia et al. (2008) argued theoretically that $\langle C_{22} \rangle \to 0$ in the limit of infinite Weissenberg number.

Polymer stresses are nonlinear with respect to the conformation tensor and their asymptotic scaling with Weissenberg number is a key element for the understanding of the polymer dynamics at MDR. Hence, following Benzi et al. (2006) consider the FENE-P model integrated over the x, z spatial directions and time, assuming statistical stationarity and homogeneity in x and z

$$\langle u_2 \partial_{x_2} C_{ij} \rangle = \langle C_{ik} \partial_{x_k} u_j \rangle + \langle C_{jk} \partial_{x_k} u_i \rangle - \frac{1}{\mathcal{W}e_c} \langle f(C_{kk}) C_{ij} - \delta_{ij} \rangle . \tag{6.4}$$

Taking the Reynolds decomposition of the velocity field $u_i = \langle u_i \rangle + u_i'$, one obtains

$$\frac{1}{\mathcal{W}e_c} \langle f(C_{kk}) C_{ij} - \delta_{ij} \rangle = \langle C_{ik} \rangle \partial_{x_k} \langle u_j \rangle + \langle C_{jk} \rangle \partial_{x_k} \langle u_i \rangle + Q_{ij} \tag{6.5}$$

where $Q_{ij} = \langle C_{ik} \partial_{x_k} u_j' \rangle + \langle C_{jk} \partial_{x_k} u_i' \rangle - \langle u_2' \partial_{x_2} C_{ij} \rangle$. Therefore, the average polymer stress tensor defined by Eqs. (5.3) and (4.22) takes the form

$$\langle \sigma_{ij} \rangle = \frac{1-\beta}{\mathcal{R}e_c} \begin{pmatrix} 2 \langle C_{12} \rangle \partial_{x_2} \langle u_1 \rangle + Q_{11} & \langle C_{22} \rangle \partial_{x_2} \langle u_1 \rangle + Q_{12} & Q_{13} \\ \langle C_{22} \rangle \partial_{x_2} \langle u_1 \rangle + Q_{12} & Q_{22} & Q_{23} \\ Q_{13} & Q_{23} & Q_{33} \end{pmatrix} . \tag{6.6}$$

Now, the important assumption at the limit of a local $\mathcal{W}e_S \equiv \tau_p \frac{\mathrm{d}}{\mathrm{d}y} \langle u \rangle \to \infty$ is that Q_{11} and Q_{12} can be neglected, considering the polymers to be stiff, i.e. $C_{ij} \to \langle C_{ij} \rangle$, mostly in the main stretching directions and the correlations between fluctuating

conformation tensor and velocity fields in the other Cartesian directions to remain minimal at this limit. In this case, as a result

$$\langle \sigma_{11} \rangle = A_1 \frac{1-\beta}{\mathcal{R}e_c} 2 \langle C_{12} \rangle \partial_{x_2} \langle u_1 \rangle \tag{6.7}$$

$$\langle \sigma_{12} \rangle = A_2 \frac{1-\beta}{\mathcal{R}e_c} \langle C_{22} \rangle \partial_{x_2} \langle u_1 \rangle \tag{6.8}$$

where A_1 and A_2 are expected to be independent of y and equal to 1 in a region somewhere between the wall and the centreline of the channel as $\mathcal{W}e_S \gg 1$. This hypothesis is checked in Fig. 6.7 against various viscoelastic DNS from Table 6.1.

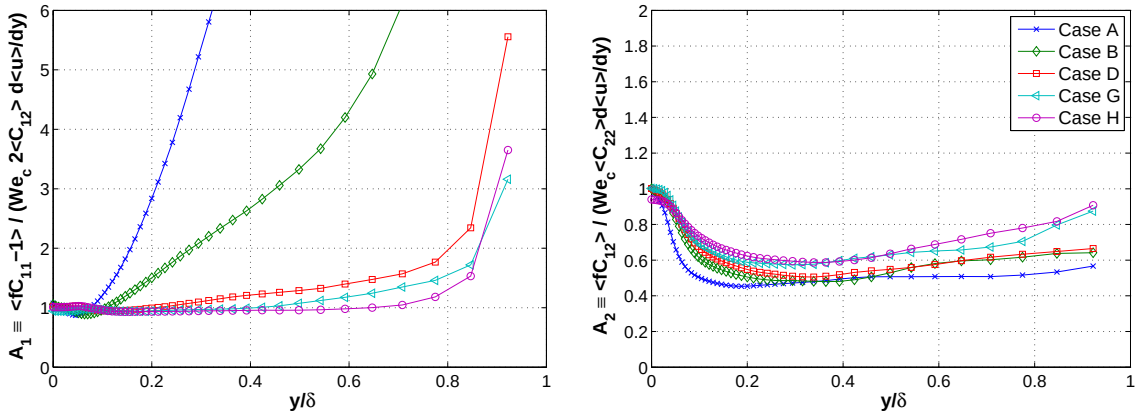

(a) $A_1 \equiv \langle \sigma_{11} \rangle \,/\, \left(\frac{1-\beta}{\mathcal{R}e_c} 2 \langle C_{12} \rangle \frac{\mathrm{d}\langle u \rangle}{\mathrm{d}y} \right)$ versus y/δ (b) $A_2 \equiv \langle \sigma_{12} \rangle \,/\, \left(\frac{1-\beta}{\mathcal{R}e_c} \langle C_{22} \rangle \frac{\mathrm{d}\langle u \rangle}{\mathrm{d}y} \right)$ versus y/δ

Figure 6.7: Scalings of the polymer stress components $\langle \sigma_{11} \rangle$ and $\langle \sigma_{12} \rangle$.

Figure 6.7a shows clearly that A_1 tends to 1 in the region $0 \lesssim y/\delta \lesssim 0.8$ for high $\mathcal{W}e_S$ values justifying that Q_{11} can be neglected for HDR and MDR cases. Note that A_1 deviates from 1 towards the centre of the channel because $\mathcal{W}e_S$ becomes small in this region. A_2 is approximately independent of y in some intermediate region in the flow for almost all cases and appears to tend towards 1 as $\mathcal{W}e_S$ increases (see Fig. 6.7b). However, the polymer relaxation time scales used in this study are not sufficiently high for $A_2 \to 1$. So, in this case the polymer shear stress can be considered to be $\langle \sigma_{12} \rangle \propto \frac{1-\beta}{\mathcal{R}e_c} \langle C_{22} \rangle \partial_{x_2} \langle u_1 \rangle$ in the range $0.2 \lesssim y/\delta \lesssim 0.6$. It is appealing to see that $\langle C_{22} \rangle$ is the component involved in the MDR dynamics, bearing in mind that $\langle C_{11} \rangle \gg \langle C_{12} \rangle \simeq \langle C_{33} \rangle > \langle C_{22} \rangle$. In the end, both Figs. 6.6 and 6.7 confirm the claims that $\langle C_{12} \rangle$ has reached its asymptotic limit within the Weissenberg numbers considered here at this particular Reynolds number, unlike $\langle C_{22} \rangle$.

6.4 Shear stress balance

The balance of shear stresses Eq. (6.1) is considered in this section. The total shear stress in viscoelastic turbulent channel flow contains an extra stress term in contrast to Eq. (2.38), as has already been shown. This extra term is the mean polymer shear stress and it is also referred to as the Reynolds stress deficit since $\nu \frac{\mathrm{d}}{\mathrm{d}y} \langle u \rangle - \langle uv \rangle \neq u_\tau^2 (1 - y/\delta)$. The viscous stress of the solvent, the Reynolds shear stress and the mean polymer shear stress normalised with viscous scales are presented in Fig. 6.8 at different levels of $\%DR$ for cases with the same $\mathcal{R}e_c$ from Table 6.1.

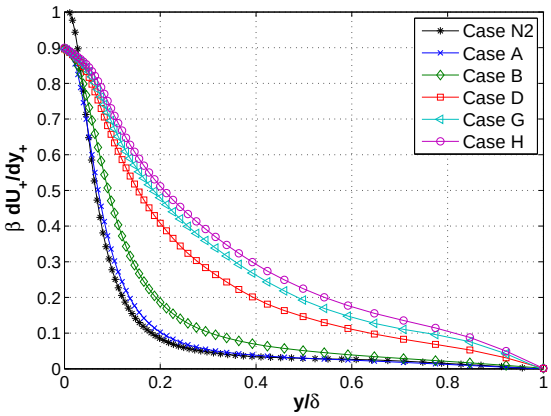

(a) Viscous shear stress versus y/δ

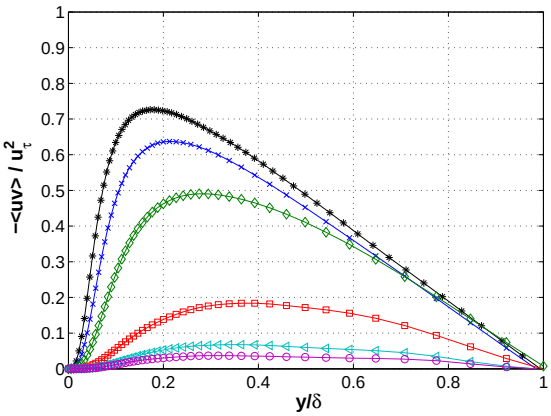

(b) Reynolds shear stress versus y/δ

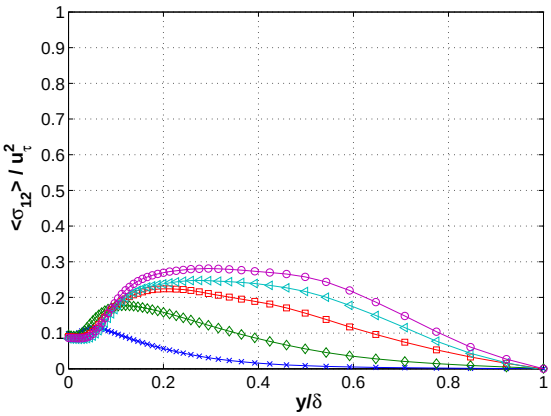

(c) Mean polymer shear stress versus y/δ

Figure 6.8: Mean shear stresses profiles for the LDR, HDR and MDR regimes.

At the wall, the no-slip boundary condition enforces $-\langle uv \rangle \big|_{y=0} = 0$. Then, the wall shear stress and the viscous sublayer are governed by 90% viscous as well as 10% polymer contribution for all viscoelastic cases as opposed to the Newtonian case

N2. Viscosity is the dominant parameter in the near-wall region but becomes more influential in the outer regions as drag reduction enhances. This is clear from Fig. 6.8a where $\beta\frac{\mathrm{d}}{\mathrm{d}y_+}U_+$ increases monotonically towards the centre of the channel as $\mathcal{W}e_c$ increases. Viscoelastic effects become also more significant towards the centre of the channel for higher $\mathcal{W}e_c$ cases. Reynolds shear stress, on the other hand, is constantly decorrelated at higher $\%DR$ with its peak shifting away from the wall. It is interesting to see that for the HDR case D $-\langle uv\rangle$ and $\langle\sigma_{12}\rangle$ are comparable and as MDR is approached the polymer shear stress plays an increasingly fundamental role in sustaining turbulence due to the vast attenuation of the Reynolds shear stress at these finite Reynolds number computations. This becomes apparent in the next section by analysing the turbulent kinetic energy budget.

Notice that Reynolds shear stress remains finite at MDR confirming the experimental measurements by Ptasinski et al. (2001) against the complete depletion of $-\langle uv\rangle$ reported by Warholic et al. (1999) and their subsequent claim that turbulence is sustained entirely by polymer stresses. What can be said theoretically on this controversy is the following. Consider first the limit of $\mathcal{W}e_S \to \infty$, where $A_2 \to 1$ for Eq. (6.8) even at finite Reynolds numbers, as Fig. 6.7b indicated. Then, the total shear stress balance can be rewritten using Eq. (6.8)

$$\nu(\beta + (1-\beta)\langle C_{22}\rangle)\frac{\mathrm{d}\langle u\rangle}{\mathrm{d}y} - \langle uv\rangle \simeq u_\tau^2\left(1-\frac{y}{\delta}\right) \tag{6.9}$$

where $\nu_{eff}(y) \equiv \nu(\beta + (1-\beta)\langle C_{22}\rangle)$ is an effective viscosity similar to the one encountered in Lumley's phenomenology (Lumley, 1973; Procaccia et al., 2008). Now, when $\mathcal{W}e_S \gg 1$ assume that $\langle C_{22}\rangle$ becomes minimal based on theoretical claims by L'vov et al. (2005); Procaccia et al. (2008) and observational indications in this study. Then, for high enough Reynolds number along the universal MDR asymptotic line, i.e. taking first the infinite Weissenberg number limit and then the infinite Reynolds number limit, one might expect an intermediate region $\delta_\nu \ll y \ll \delta$ of approximately constant Reynolds shear stress, i.e. $-\langle uv\rangle/u_\tau^2 \to 1$, implied by Eq. (6.9) when taking the limits of $y/\delta \to 0$ and $y/\delta_\nu \to \infty$ with the reasonable assumption that $\nu\beta\frac{\mathrm{d}}{\mathrm{d}y}\langle u\rangle \to 0$ as $y \gg \delta_\nu$. This statement denotes that the classical way of turbulence production does not vanish in the infinite Weissenberg and Reynolds number limit. Ultimately, the conjecture here is that $\langle\sigma_{12}\rangle$ can be minor under both limits. This, however, does not indicate that drag reduction is depleted, it rather suggests that

the MDR asymptote could be entirely determined by the energetics in these infinite limits. Nevertheless, polymers play a crucial role in the dynamics at MDR and this will be explored further in the next section.

6.5 Polymer-turbulence dynamical interactions

The balance equation for the turbulent kinetic energy of a viscoelastic fluid provides further insight into the dynamical interactions between polymers and turbulence. Following a similar procedure to section 2.2 and assuming statistical stationarity and homogeneity in x and z directions, an equivalent energy balance to Eq. (2.29) can be derived for this case

$$0 = -\partial_y \left(\frac{1}{\rho} \left\langle u_j' p' \right\rangle + \frac{1}{2} \left\langle u_i' u_j' u_j' \right\rangle - 2 \frac{\beta}{\mathcal{R}e_c} \left\langle u_i' s_{ij} \right\rangle + \left\langle u_i' \sigma_{ij}' \right\rangle \right) + \mathcal{P} - \varepsilon_N - \varepsilon_P \quad (6.10)$$

where two extra terms arise due to polymers, a transport term $\partial_y \left\langle u_i' \sigma_{ij}' \right\rangle$ and a dissipation rate of energy $\varepsilon_P \equiv \left\langle \sigma_{ij}' \partial_{x_j} u_i' \right\rangle$ due to fluctuating viscoelastic stresses. Note that ε_P has a dual nature, i.e. it can serve either as dissipation or production depending on the signs of the polymer stress fluctuations and that of the fluctuating velocity gradients. All energy balance terms are made dimensionless according to the variables in Eq. (5.1). Integration of Eq. (6.10) over the y direction yields

$$\int \mathcal{P} \, \mathrm{d}y = \int \varepsilon_N \, \mathrm{d}y + \int \varepsilon_P \, \mathrm{d}y \quad (6.11)$$

with no contribution from the transport terms in the parenthesis due to the no-slip boundary condition, using the divergence theorem. The viscous dissipation of turbulent kinetic energy is denoted here as $\varepsilon_N \equiv 2\frac{\beta}{\mathcal{R}e_c} \left\langle s_{ij} s_{ij} \right\rangle$ and turbulence production $\mathcal{P}$ by Reynolds shear stress is defined in Eq. (2.59).

Figure 6.9 presents each term of Eq. (6.11) normalised by δ_ν / u_τ^3 with respect to $\mathcal{W}e_{\tau_0}$ for all cases from Table 6.1 at $\mathcal{R}e_c = 4250$. An asymptotic behaviour to a marginal flow state can be observed by increasing the polymer relaxation time scale with a vast attenuation occurring in the total production and viscous dissipation, while viscoelastic dissipation grows mildly in the LDR regime and constantly decays within HDR and MDR. Overall, $\int \varepsilon_P \, \mathrm{d}y$ becomes pivotal in the dynamics of the flow relative to $\int \mathcal{P} \, \mathrm{d}y$ and $\int \varepsilon_N \, \mathrm{d}y$ for HDR and MDR flows. Most importantly

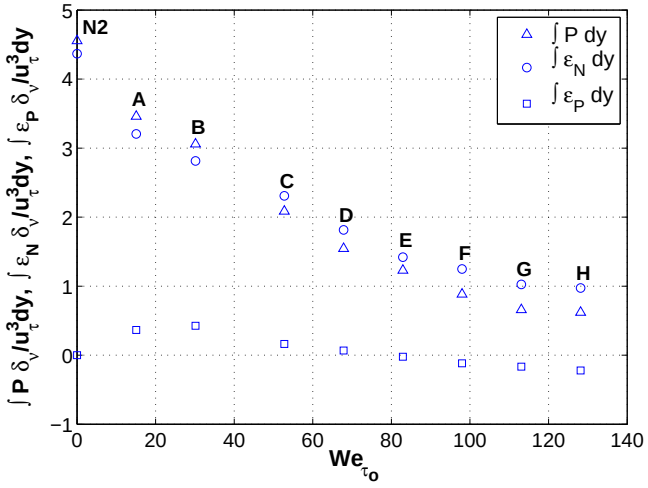

Figure 6.9: Terms of the y-integrated turbulent energy balance with respect to $\mathcal{W}e_{\tau_0}$.

$\int \varepsilon_P \, \mathrm{d}y < 0$ for high $\mathcal{W}e_{\tau_0}$ values according to Fig. 6.9, in agreement with experimental measurements (see Table V in Ptasinski et al. (2001)), implying that polymers somehow can sustain turbulence by producing turbulent kinetic energy. Notice, that in this plot both dissipations are presented as positive quantities and this was done on purpose to emphasise the interplay between production and viscous dissipation from LDR to HDR. It is noteworthy that $\int \mathcal{P} \, \mathrm{d}y > \int \varepsilon_N \, \mathrm{d}y$ for LDR cases A and B but $\int \mathcal{P} \, \mathrm{d}y < \int \varepsilon_N \, \mathrm{d}y$ for HDR cases and gets even smaller as drag reduction approaches its maximum limit. This observation hints that polymer dynamics get somehow involved in the production of turbulent kinetic energy so that turbulence does not die out at HDR and MDR. Such a mechanism will be analysed in the next section.

Let us now look in more detail at the profiles of $\mathcal{P}$, ε_N and ε_P scaled by δ_ν/u_τ^3 with respect to normalised distance from the wall y/δ for representative cases at various levels of drag reduction from Table 6.1 (see Fig. 6.10). Dissipation represents drain of energy, hence, ε_N and ε_P have been plotted here as negative quantities.

The production of turbulent energy by Reynolds stresses, which is continuously reduced over the extend of drag reduction as a function of $\mathcal{W}e_c$, serves to exchange kinetic energy between the mean flow and the turbulence. The local peak of $\mathcal{P}$ is reached within the buffer layer and in fact for Newtonian flows it can be easily shown that the maximum production occurs where $-\langle uv \rangle = \nu \frac{\mathrm{d}}{\mathrm{d}y} \langle u \rangle$ and $\mathcal{P}_{max} \delta_\nu / u_\tau^3 < \frac{1}{4}$ (Pope, 2000). The peak turbulence production within the LDR regime also occurs at

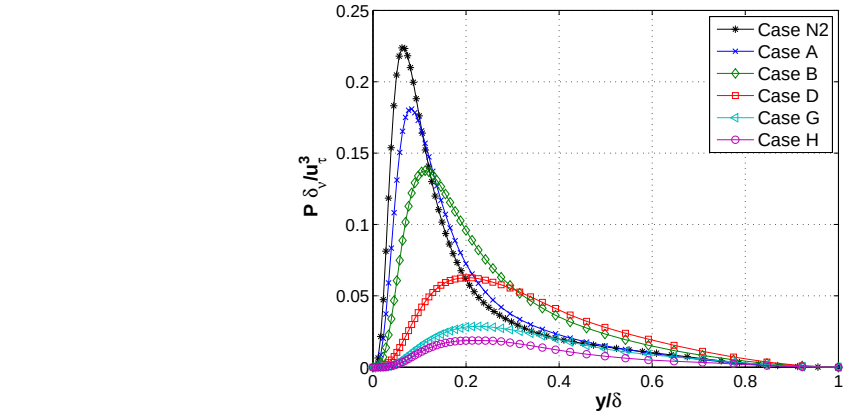

(a) $\mathcal{P}\delta_\nu/u_\tau^3$ as function of y/δ

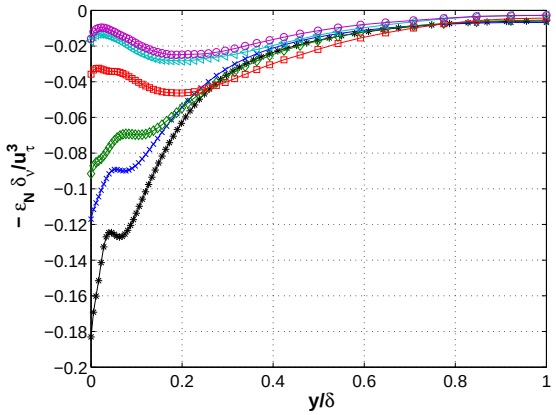

(b) $-\varepsilon_N\delta_\nu/u_\tau^3$ as function of y/δ

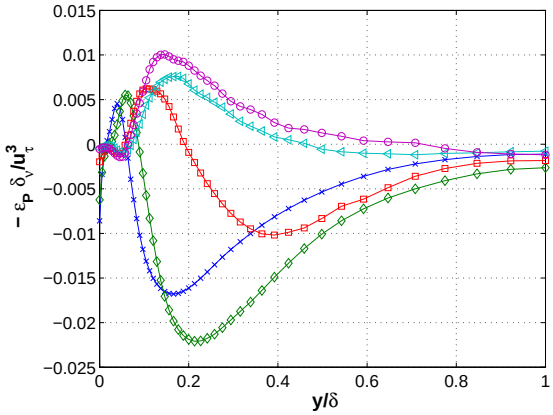

(c) $-\varepsilon_P\delta_\nu/u_\tau^3$ as function of y/δ

Figure 6.10: Profiles of turbulence production, viscous and viscoelastic dissipation for the LDR, HDR and MDR regimes.

the intersection point of viscous and Reynolds shear stress (compare Figs. 6.8a and 6.8b with Fig. 6.10a), which shifts away from the wall as $\mathcal{W}e_c$ increases, indicating the thickening of the elastic layer. However, for HDR and MDR cases $\mathcal{P}_{max}\delta_\nu/u_\tau^3$ is within $0.1 < y/\delta \lesssim 0.3$, where the maximum Reynolds stress roughly appears, without following the $-\langle uv\rangle = \beta\nu\frac{\mathrm{d}}{\mathrm{d}y}\langle u\rangle$ intersection point, which does not even exist for cases G and H (see Figs. 6.8a and 6.8b).

Viscous dissipation exhibits monotonic attenuation as drag reduces for higher values of $\mathcal{W}e_c$ with the maximum dissipation arising at the wall for the Newtonian case N2 and the LDR cases A and B (see Fig. 6.10b). Although the kinetic energy is zero at the wall since $\boldsymbol{u}'|_{y=0} = 0$ imposed by the no-slip boundary conditions, the fluctuating strain rate and consequently ε_N is non-zero. At high $\%DR$, it is surprising

to observe that the highest fluctuating strain rates are encountered away from the wall providing a completely different picture of the near-wall dissipation dynamics. The local kink in the buffer/elastic layer, which arises due to intense activity in this region, exists at corresponding y/δ with $\mathcal{P}_{max}\delta_\nu/u_\tau^3$ for all cases considered in Fig. 6.10b and becomes a global minimum for the HDR and MDR cases, dominating the profiles of viscous dissipation.

The profiles of viscoelastic dissipation obey a characteristic transitional trend similar to what has been already observed for u'_+ (see Fig. 6.4b) and $\langle C_{22}\rangle$ (see Fig. 6.6c) from LDR to HDR regime, as $\mathcal{W}e_c$ increases. In detail, the curves of LDR cases A and B shift downwards increasing viscoelastic dissipation but those of the HDR/MDR cases move upwards enhancing the positive nature of $-\varepsilon_P\delta_\nu/u_\tau^3$. The dual nature of ε_P is clearly depicted in Fig. 6.10c with polymers dissipating and producing turbulent kinetic energy in different regions, which depend on the polymer relaxation time scale at a given Reynolds number. A Reynolds number dependence of these regions is expected owing to the effect of different flow time scales on dumbbells with a particular relaxation time scale. Figure 6.11 compares cases of identical Weissenberg numbers and different Reynolds numbers (see Table 6.1), illustrating a weaker $\mathcal{R}e_c$ dependence on viscoelastic dissipation in comparison to the stronger $\mathcal{W}e_c$ dependence in Fig. 6.10c, particularly at HDR and MDR.

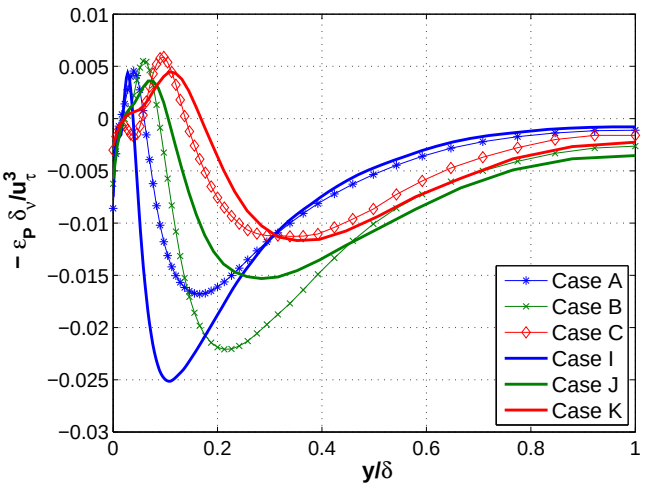

Figure 6.11: Effect of Reynolds number on viscoelastic dissipation as function of y/δ. Identical colours correspond to cases with the same $\mathcal{W}e_c$ values.

Now, considering each component of the correlation matrix $\varepsilon_P \equiv \left\langle \sigma'_{ij} \partial_{x_j} u'_i \right\rangle$, where summation applies over the indices i and j, it can be observed that components with $i = 2, 3$ can be ignored, with most of the contribution ascribed to $i = 1$ components according to Fig. 6.12a which is very similar to Fig. 6.10c. The quali-

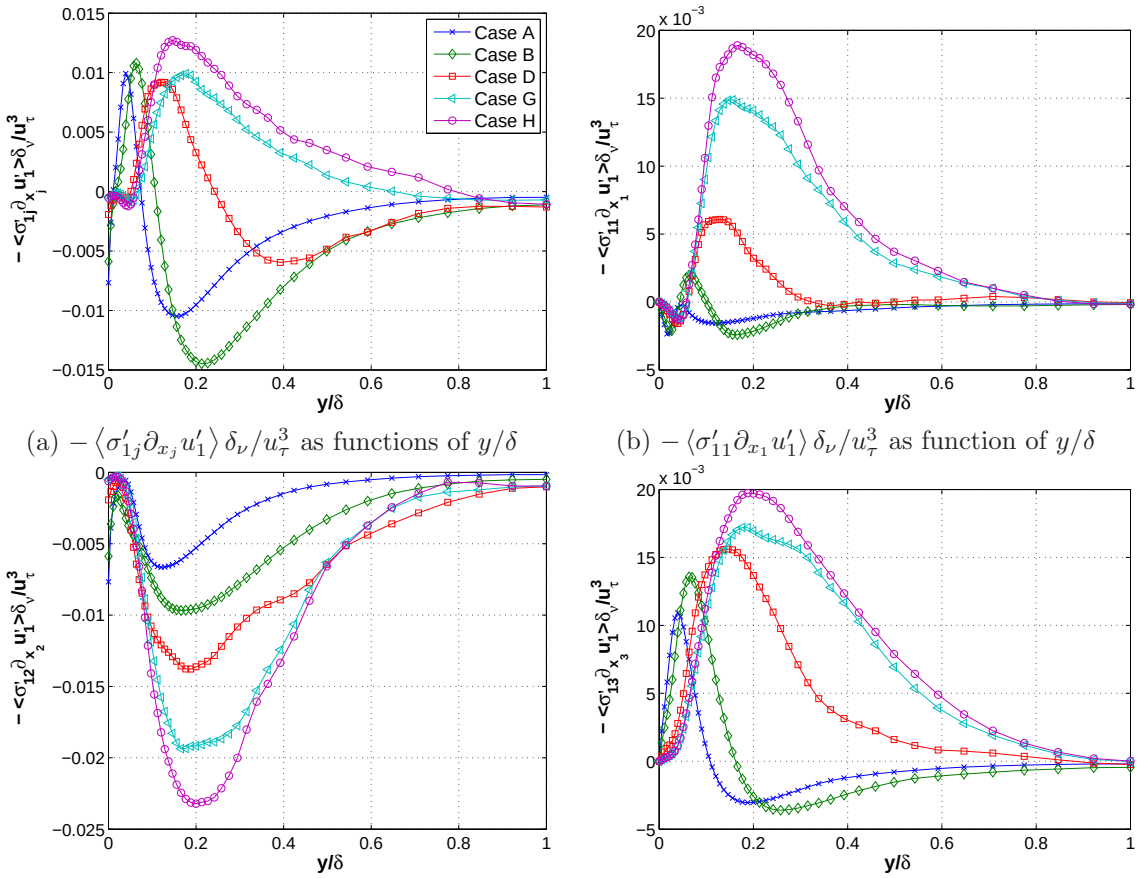

(a) $-\left\langle \sigma'_{1j} \partial_{x_j} u'_1 \right\rangle \delta_\nu / u_\tau^3$ as functions of y/δ

(b) $-\left\langle \sigma'_{11} \partial_{x_1} u'_1 \right\rangle \delta_\nu / u_\tau^3$ as function of y/δ

(c) $-\left\langle \sigma'_{12} \partial_{x_2} u'_1 \right\rangle \delta_\nu / u_\tau^3$ as function of y/δ

(d) $-\left\langle \sigma'_{13} \partial_{x_3} u'_1 \right\rangle \delta_\nu / u_\tau^3$ as function of y/δ

Figure 6.12: Profiles of viscoelastic dissipation components for the LDR, HDR and MDR regimes.

tative features of ε_P are clearly captured by $\left\langle \sigma'_{1j} \partial_{x_j} u'_1 \right\rangle$, simplifying the underpining dynamics of viscoelastic dissipation. However, to be precise ε_P is neither exactly approximate nor proportional to $\left\langle \sigma'_{1j} \partial_{x_j} u'_1 \right\rangle$. Note that the positive nature of ε_P is caused by the correlations $-\left\langle \sigma'_{11} \partial_{x_1} u'_1 \right\rangle$ and $-\left\langle \sigma'_{13} \partial_{x_3} u'_1 \right\rangle$ (see Figs. 6.12b and 6.12d). The rest of the components are negative for all cases considered here and decrease monotonically as $\mathcal{W}e_c$ increases like $-\left\langle \sigma'_{12} \partial_{x_2} u'_1 \right\rangle$ in Fig. 6.12c. The only exception though is $-\left\langle \sigma'_{32} \partial_{x_2} u'_3 \right\rangle$, which also exhibits a dual trend, negligible however in com-

parison to the components presented in Fig. 6.12. Finally, the correlations in Figs. 6.12b and 6.12d are also responsible for the transitional behaviour of viscoelastic dissipation profiles from LDR to HDR discussed earlier.

The current picture of the dual nature of ε_P was first predicted by Min et al. (2003b) at low Weissenberg numbers, using the LAD scheme to numerically solve the FENE-P model (see section 5.1). However, the present DNS are the first to capture so clearly these regions throughout the drag reduction regimes, predicting the appropriate dynamics at corresponding $\mathcal{W}e_c$ values. Once more, this is attributed to the numerical approach applied here for the FENE-P model that is able to provide stronger polymer-turbulence interactions than algorithms based on artificial diffusion. There are even results using the artificial diffusion methodologies that erroneously predict polymers never feeding energy back to the flow (Ptasinski et al., 2003; Procaccia et al., 2008). Hence, in view of the current distinctly transparent observations a conceptual model for the mechanism of drag reduction is deduced in the next section.

6.6 Drag reduction mechanism

The recent review on polymer drag reduction by White and Mungal (2008) reports that the numerical evidence is somewhat conflicting regarding the flow regions where polymers extend and contract. In this study, these regions can be identified by applying the Reynolds decompositions $u_i = \langle u_i \rangle + u_i'$ and $\sigma_{ij} = \langle \sigma_{ij} \rangle + \sigma_{ij}'$ to Eq. (4.27), following the spirit of Min et al. (2003b); Ptasinski et al. (2003). Then, it can be noticed that $\left\langle \sigma_{ij}' \partial_{x_j} u_i' \right\rangle$ appears as a production term due to turbulence for the mean polymer elastic energy. Now, from the definition of polymer elastic energy Eq. (4.24), it is evident that $\langle E_p \rangle \propto \ln \langle f(C_{kk}) \rangle$. So, the FENE-P dumbbells are stretched when $-\varepsilon_P \delta_\nu / u_\tau^3 < 0$ in Fig. 6.10c and then elastic energy is stored on polymers, absorbing turbulent kinetic energy from the flow. Hence, a mechanism of drag reduction can be proposed based on the polymers stretching or in other words the behaviour of viscoelastic dissipation as a function of the distance y from the wall.

According to Figs. 6.10c and 6.11 there are three main regions in the profiles of viscoelastic dissipation

$$-\varepsilon_P \delta_\nu / u_\tau^3 = \begin{cases} -\text{ve} & \text{for } 0 \leq y/\delta < \delta_1(\mathcal{W}e_c, \mathcal{R}e_c) \\ +\text{ve} & \text{for } \delta_1(\mathcal{W}e_c, \mathcal{R}e_c) \leq y/\delta \leq \delta_2(\mathcal{W}e_c, \mathcal{R}e_c) \\ -\text{ve} & \text{for } \delta_2(\mathcal{W}e_c, \mathcal{R}e_c) < y/\delta \leq 1. \end{cases} \tag{6.12}$$

The first region is at the proximity of the wall, where polymers unravel because of the high mean shear, consistent with other studies (Massah and Hanratty, 1997; Min et al., 2003b; Terrapon et al., 2004; Dubief et al., 2004), storing elastic potential energy. The range of this region has a weak dependence on Weissenberg and Reynolds number with its upper bound being within the viscous sublayer $\delta_1(\mathcal{W}e_c, \mathcal{R}e_c) \lesssim 0.05$ for all $\mathcal{W}e_c$ and $\mathcal{R}e_c$ cases considered.

The second region is the most interesting since polymers release energy back to the flow, contracting towards their equilibrium length, as they are convected away from the wall by the near-wall vortical motions. The manifestation of turbulence production by polymers can be interpreted in terms of the correlation of the polymers with the local fluctuating strain rates and their persistence in this region. In particular, $-\left\langle \sigma'_{ij} \partial_{x_j} u'_i \right\rangle$ reveals that $-\langle \sigma'_{11} \partial_{x_1} u'_1 \rangle$ as well as $-\langle \sigma'_{13} \partial_{x_3} u'_1 \rangle$ are responsible for the contraction of the dumbbells and consequently for the release of the stored elastic energy, since they are positively correlated in this region away from the wall (see Figs. 6.12b and 6.12d). This region exists in an intermediate y/δ range, whose upper bound $\delta_2(\mathcal{W}e_c, \mathcal{R}e_c)$ is strongly dependent on $\mathcal{W}e_c$ and less on $\mathcal{R}e_c$ values. As drag reduction amplifies for larger polymer relaxation time scales this positive region expands to a wider y/δ range, which dominates the nature of $-\varepsilon_P \delta_\nu / u_\tau^3$ at MDR (see Fig. 6.10c).

Finally, polymers transported away from the wall get also negatively correlated with the persistent fluctuating strain rates (see Fig. 6.12c) and are extended in the region $\delta_2(\mathcal{W}e_c, \mathcal{R}e_c) < y/\delta \leq 1$, which is a sink for turbulent kinetic energy, prevailing the LDR flows. However, this region is diminished for HDR and MDR flows (see Fig. 6.10c) due to the interplay between the productive and dissipative inherent features of ε_P, which mainly depend on the polymer relaxation time scale and the existence of intense velocity fluctuations that are able to stretch the polymers.

The phenomenology of the proposed mechanism shares many similarities with various conceptual models of earlier works (White and Mungal, 2008). In this study, the basic idea is that the transport of the elastic potential energy, stored by polymers near the wall, is mainly associated with the polymer relaxation time scale. The latter determines the distribution of energy away from the wall and as a consequence the near-wall turbulence dynamics weaken. Up to this point, the mechanism agrees with the interpretation of Min et al. (2003b), which is essentially confirmed by the present illustrative computations. However, the novelty here is that this mechanism is valid for higher $\mathcal{W}e_c$ values and levels of $\%DR$ in contrast to Min et al. (2003a), who claim that it is not valid for HDR/MDR flows basing their arguments on their debatable numerical results (see also section 6.2.3).

In addition, the refinement of the proposed conceptual mechanism resides on the reduction of ε_P with $\left\langle \sigma'_{1j}\partial_{x_j}u'_1 \right\rangle$ and even more on the correlations $\langle \sigma'_{11}\partial_{x_1}u'_1 \rangle$ and $\langle \sigma'_{13}\partial_{x_3}u'_1 \rangle$, which are responsible for the turbulence production by polymer coils. The existence of a third dissipative region away from the wall is also emphasised in this mechanism, where polymers, after their contraction, are now stretched again by the intense fluctuating velocity field. This outer region dominates the viscoelastic dissipative dynamics of the LDR regime and diminishes asymptotically as $\mathcal{W}e_c$ increases but it never disappears. Ultimately, this picture along with the anisotropy introduced into the components of turbulent kinetic energy, i.e. $E = \frac{1}{2}(u'^2+v'^2+w'^2)$, comprise the present drag reduction mechanism deduced in this study.

6.7 Summary

This chapter is devoted to the polymer dynamics in viscoelastic turbulent channel flow and their effects on the flow, reproducing turbulent drag reduction by DNS using a novel numerical scheme in wall-bounded flows to solve the FENE-P model. The potential of this methodology to capture the strong polymer-turbulence dynamical interactions led to the following observations. (*i*) All the statistical quantities are qualitatively closer to experimental measurements than prior numerical studies using the artificial diffusion algorithms. (*ii*) The onset of drag reduction and the MDR asymptote are realisable without polymers undergoing coil-stretch transition in contrast to Lumley's (1969) theory, since $\langle C_{kk} \rangle / L_p^2 \ll 1$ for all $\mathcal{W}e_c$ values. (*iii*) The increase of anisotropy in the fluctuating flow field, particularly at HDR and

MDR, is due to the strong anisotropic behaviour of the mean conformation tensor, i.e. $\langle C_{11}\rangle \gg \langle C_{12}\rangle \simeq \langle C_{33}\rangle > \langle C_{22}\rangle$ caused by the mean shear. (*iv*) The dependence of dynamics on L_p and $\mathcal{R}e_c$ for $\%DR$ between the von Kármán and the MDR law confirm the non-universal aspects of polymer-induced drag reduction. On the other hand, the MDR universal asymptote is reached for high enough $\mathcal{W}e_c$ values at a moderate $\mathcal{R}e_c$. (*v*) Assuming that polymers can be considered as almost rigid, i.e. $C_{ij} \simeq \langle C_{ij}\rangle$, mostly in the main extending direction in the limit of $\mathcal{W}e_S \to \infty$, then $\langle\sigma_{12}\rangle \simeq A_2 \frac{1-\beta}{\mathcal{R}e_c} \langle C_{22}\rangle \frac{\mathrm{d}}{\mathrm{d}y} \langle u\rangle$, with $A_2 \to 1$ for $0 \lesssim y/\delta \lesssim 0.8$ at finite $\mathcal{R}e_c$. (*vi*) It is conjectured that $\langle C_{22}\rangle$ becomes negligible in the limit of $\mathcal{W}e_S \to \infty$. Then, at high enough Reynolds number along the universal MDR asymptotic line, one might expect $-\langle uv\rangle / u_\tau^2 \to 1$ in an intermediate region $\delta_\nu \ll y \ll \delta$ when taking the limits of $y/\delta \to 0$ and $y/\delta_\nu \to \infty$ with $\nu\beta \frac{\mathrm{d}}{\mathrm{d}y} \langle u\rangle \to 0$ for $y \gg \delta_\nu$. (*vii*) The $\int \varepsilon_P \,\mathrm{d}y$ substantiates that polymer molecules dissipate energy at LDR but remarkably produce energy at HDR and MDR. (*viii*) The redistribution of energy away from the wall by the polymers weakens the dynamics of near-wall turbulence in the spirit of Min et al. (2003b). The present computations extend this conceptual mechanism to higher $\mathcal{W}e_c$ and levels of $\%DR$ and refine it by identifying the important correlations that induce the production of energy by polymer molecules.

Chapter 7

Conclusions

An attempt is made in this thesis to contribute to the advance of our understanding on two main topics of vital importance in hydrodynamic wall-bounded turbulence, the mean velocity in terms of its scaling with Reynolds number, re-examining the basis of the asymptotic scaling relationships from a different viewpoint and the phenomenon of turbulent drag reduction in viscoelastic turbulence, adapting a state-of-the-art numerical method for the first time in a wall-bounded flow. The main results of this numerical and theoretical study are reviewed here, conveying their implications and where these lead in terms of future research directions.

DNS of turbulent channel flows considered in this work suggest that $B_1 = \lambda/\ell_s$ and $C_s = n_s\delta_\nu^3 y_+$ are approximately constant in the region $\delta_\nu \ll y \lesssim \delta$. In view of these DNS cases, these well-defined approximate constancies were demonstrated for $\mathcal{R}e_\tau$ as low as a few hundred. These constancies imply that, in the region $\delta_\nu \ll y \lesssim \delta$, the eddy turnover time $\tau = \frac{3}{2}\kappa_s y/u_\tau$ with $\kappa_s = B_1^2/C_s$. Assuming the constancies of B_1 and C_s to be early manifestations of a high Reynolds number behaviour, i.e. that B_1, C_s and therefore κ_s are independent of y in $\delta_\nu \ll y \lesssim \delta$ as $\mathcal{R}e_\tau \to \infty$, it follows that $\frac{\mathrm{d}\langle u\rangle}{\mathrm{d}y} \simeq \frac{2}{3}E_+\frac{u_\tau}{\kappa_s y}$ in the equilibrium region $\delta_\nu \ll y \ll \delta$ where production may be expected to balance dissipation and $-\langle uv\rangle \simeq u_\tau^2$. The asymptotic equality $-\langle uv\rangle \simeq u_\tau^2$ is mathematically supported only for turbulent channel/pipe flows.

The classical intermediate asymptotics, which assume no dependence of the mean velocity gradient on ν and δ where $\delta_\nu \ll y \ll \delta$, do not consider the effect that Townsend's inactive motions may or may not have on $\frac{\mathrm{d}}{\mathrm{d}y}\langle u\rangle$. However, if a new intermediate asymptotic approach is taken where the assumption of no dependence

on ν and δ is applied to $\tau \equiv E/\varepsilon$ instead of $\frac{\mathrm{d}}{\mathrm{d}y}\langle u\rangle$, then $\tau \propto y/u_\tau$, and the small effects of Townsend's inactive motions on $\frac{\mathrm{d}}{\mathrm{d}y}\langle u\rangle$ may not be neglected because $\tau \simeq \frac{3}{2}\kappa_s y/u_\tau$, $-\langle uv\rangle \simeq u_\tau^2$ and $-\langle uv\rangle \frac{\mathrm{d}}{\mathrm{d}y}\langle u\rangle \simeq \varepsilon$ yield Eq. (3.16) which explicitly contains E_+. If E does not scale as u_τ^2 as a result of inactive motions, then this revised intermediate asymptotic approach will not predict a log-law for the mean profile even though a stagnation point von Kármán coefficient κ_s exists and is well defined within the approach. The mean flow prediction of this approach is instead controlled by the intermediate asymptotic dependence of E_+ on y_+ and $\mathcal{R}e_\tau$. If this dependence on y_+ is a power-law $E_+ \propto y_+^{-n}$ in the intermediate range $\delta_\nu \ll y \ll \delta$, then the mean flow profile will also be a power law, i.e. $\frac{\mathrm{d}}{\mathrm{d}y_+}U_+ \propto y_+^{-(1+n)}$, in that intermediate layer.

DNS of turbulent channel flow with the highest values of $\mathcal{R}e_\tau$ currently available (Hoyas and Jiménez, 2006) suggest $n = 2/15$ in both $E_+ \propto y_+^{-n}$ and $\frac{\mathrm{d}}{\mathrm{d}y_+}U_+ \propto y_+^{-(1+n)}$ in support of the present procedure and Eq. (3.16). However, caution should be taken against extrapolating this value of the exponent n to higher values of $\mathcal{R}e_\tau$, in particular in the laboratory where the boundary conditions are in fact different from the DNS which is periodic in x and z directions. It has to be stressed that the main point of value here is the support that these elaborate high $\mathcal{R}e_\tau$ DNS (Hoyas and Jiménez, 2006) bring to the present approach and especially to the new Eq. (3.16).

Note also that the stagnation point von Kármán coefficient is defined by $\varepsilon = \frac{2}{3}E_+\frac{u_\tau^3}{\kappa_s y}$ in the range $\delta_\nu \ll y \lesssim \delta$ irrespective of whether the mean flow profile is a log-law or a power-law. Power-law profiles of E_+ and $\frac{\mathrm{d}}{\mathrm{d}y_+}U_+$ in the intermediate layer $\delta_\nu \ll y \ll \delta$, simply force $\varepsilon \simeq \frac{2}{3}E_+\frac{u_\tau^3}{\kappa_s y}$ to imply that the classical relation $\varepsilon \simeq \frac{u_\tau^3}{\kappa y}$ does not hold in that layer.

DNS observations that Eqs. (3.9) and (3.11) are valid in the region $\delta_\nu \ll y \lesssim \delta$ support this new intermediate asymptotic approach because Eqs. (3.9) and (3.11) imply $\tau \simeq \frac{3}{2}\kappa_s y/u_\tau$ with $\kappa_s = B_1^2/C_s$. The relation $\kappa_s = B_1^2/C_s$ offers a link between the underlying flow structure, described in terms of stagnation points, and the dissipation/cascade statistics of the turbulence. The universality in terms of both $\mathcal{R}e_\tau$ and flow-type dependencies of κ_s becomes a question concerning the universality of the stagnation point structure of the turbulent fluctuations. To what extent does this structure depend on boundary and wall forcing conditions? Is it the same in turbulent channel and turbulent pipe flows? Is it the same in DNS of such flows where periodic boundary conditions are used and in laboratory realisations of such flows where boundary conditions are clearly not periodic? These are questions which must

be left for future investigation, but the approach here makes them fully legitimate as there is no reason to expect the stagnation point structure of turbulent velocity fluctuations to be exactly the same in all these cases.

The implications of this new approach for the mean flow profile in turbulent channel/pipe flows come by invoking a local balance between production and dissipation as well as $-\langle uv\rangle \simeq u_\tau^2$ in the intermediate range $\delta_\nu \ll y \ll \delta$ as $\mathcal{R}e_\tau \to \infty$. A direct test against data of $\frac{\mathrm{d}}{\mathrm{d}y_+}U_+ \simeq \frac{2}{3}\frac{E_+}{\kappa_s y_+}$ in that same range and limit cannot be expected to be successful if $\mathcal{R}e_\tau$ is not large enough for $-\langle uv\rangle$ to equal u_τ^2 over the range $\delta_\nu \ll y \ll \delta$. As clearly shown by various experimental and numerical data, this equality is well beyond the highest Reynolds numbers currently available both numerically and in the laboratory. The significant finite Reynolds number deviations from $-\langle uv\rangle \simeq u_\tau^2$ appears to compensate the deviations from a log-law and from the local production-dissipation balance with the result that plots of $y\frac{\mathrm{d}}{\mathrm{d}y}U_+$ have a less varying appearance than plots of $\frac{3}{2}\frac{y}{E_+}\frac{\mathrm{d}}{\mathrm{d}y}U_+$. At face value this could be misinterpreted as better support for the log-law $\frac{\mathrm{d}}{\mathrm{d}y_+}U_+ \simeq \frac{1}{\kappa y_+}$ than for $\frac{\mathrm{d}}{\mathrm{d}y_+}U_+ \simeq \frac{2}{3}\frac{E_+}{\kappa_s y_+}$. However, plots of B_2/κ_s look significantly better than plots of B_2/κ thus demonstrating that $\frac{3}{2}\frac{y}{E_+}\frac{\mathrm{d}}{\mathrm{d}y}U_+ = B_2/(B_3\kappa_s)$ looks worse than $y\frac{\mathrm{d}}{\mathrm{d}y}U_+ = B_2/(B_3\kappa)$ only because $B_3 = -\langle uv\rangle/u_\tau^2$ is so significantly non-constant (see Fig. 3.16).

Future investigations should attempt to uncover the small-scale intermittency corrections to the new scalings presented in this chapter by determining the weak dependencies that B_1 may have on $\mathcal{R}e_\tau$ and y_+ as a result of small-scale intermittency. These dependencies will cause dependencies of κ_s on $\mathcal{R}e_\tau$ and y_+. It is remarkable that small-scale intermittency may have an impact, even if small, on the scalings of mean flow profiles. These Reynolds number parts of their scalings should be distinguished from those that Townsend's attached eddies may be contributing via the scaling of E_+ on $\mathcal{R}e_\tau$.

Moving now to the study of the polymer-induced turbulent drag reduction phenomenon, strong polymer-turbulence interactions can be captured in view of the advanced and novel algorithm for the DNS of viscoelastic turbulent channel flow employed in this study. This allowed β values to remain high, more representative of dilute polymer solutions used in experiments. Even then higher $\%DR$ for given $\mathcal{W}e_c$ values are obtained than previous numerical studies. The experimentally observed distinct differences in the statistical trends of the turbulent velocity field, particularly for u'_+ (see Fig. 6.4b), are also clearly identified with the current nu-

merical approach in comparison with other simulations, most of which do not even approach such a characteristic trend. Overall, the peaks of the statistical profiles of velocity and vorticity fluctuations shift away from the wall as $\%DR$ increases, in agreement with other experimental and numerical studies, indicating the thickening of the buffer layer. At the same time, $\nu\beta\frac{\mathrm{d}}{\mathrm{d}y}\langle u\rangle$ increases towards the centre of the channel for higher $\mathcal{W}e_c$, denoting the importance of viscosity away from the wall at these moderate Reynolds number DNS.

Lumley's phenomenology on the manifestation of drag reduction is based on the conjecture of coil-stretch transition, i.e. exponential full uncoiling of polymer molecules, for the build-up of intrinsic viscosity. However, the numerical results of this work illustrate that the onset of drag reduction and even the MDR asymptotic state can be reached while $\langle C_{kk}\rangle \ll L_p^2$ with L_p large enough. This is in agreement with the initial claim by Tabor and de Gennes (1986) that even high space-time strain rate fluctuations near the wall can only partially stretch polymer coils. It is also shown that the percentage polymer extension is less but the actual extension is more for larger L_p, amplifying $\%DR$. Thus, large polymer coils that do not reach their critical full extensibility should be of interest to experimental investigations on scission degradation of polymer chains and drag reduction effectiveness. Such macromolecules would be less vulnerable to rupture avoiding the loss of the drag reduction effect. Besides, they should be able to stretch substantially making a stronger impact on turbulent activity and consequently enhance $\%DR$. The effects of L_p and $\mathcal{R}e_c$ on the results support the claims for non-universality of the dynamics for intermediate levels of $\%DR$ between the von Kármán and the MDR law. The universal MDR asymptote, on the other hand, is reached in this study at high enough $\mathcal{W}e_c$ and L_p values for a given moderate $\mathcal{R}e_c$.

The analysis of the conformation tensor field provides great insight into the polymer dynamics and their influence on the flow. The dominant anisotropic behaviour of the mean conformation tensor, i.e. $\langle C_{11}\rangle \gg \langle C_{12}\rangle \simeq \langle C_{33}\rangle > \langle C_{22}\rangle$, due to the mean shear in viscoelastic turbulent channel flow, influences the anisotropy of the fluctuating flow field. The anisotropy in the HDR and MDR regimes is depicted at the small scales of the present DNS outside the buffer layer and towards the centre of the channel by $\omega'_{z_+} > \omega'_{y_+} > \omega'_{x_+}$. Different asymptotic rates of convergence are observed for the conformation tensor components towards the limit of infinite Weissenberg number demonstrating the complex polymer dynamics even in this sim-

plified dumbbell model. In the limit $\mathcal{W}e_S \to \infty$ polymers can be considered as stiff, i.e. $C_{ij} \to \langle C_{ij} \rangle$, mostly in the main directions of elongation and the correlations of the fluctuating conformation tensor and velocity fields in the other directions are assumed to remain minimal at this limit. Therefore, $\langle \sigma_{11} \rangle = A_1 \frac{1-\beta}{\mathcal{R}e_c} 2 \langle C_{12} \rangle \frac{\mathrm{d}}{\mathrm{d}y} \langle u \rangle$ and $\langle \sigma_{12} \rangle = A_2 \frac{1-\beta}{\mathcal{R}e_c} \langle C_{22} \rangle \frac{\mathrm{d}}{\mathrm{d}y} \langle u \rangle$, with $A_1 \to 1$ and $A_2 \to 1$ in a region somewhere between the wall and the centre of the channel in that limit. Our numerical results show that $A_1 \to 1$ in such a region but not A2. A2 on the other hand is about contant in the range $0.2 \lesssim y/\delta \lesssim 0.6$ and shows a tendency towards 1 as $\mathcal{W}e_S$ increases.

The following theoretical view could be stated with regards to the controversy over the existence or not of Reynolds shear stress at the MDR limit, which is of fundamental importance to the dynamics of turbulence production at this limit. It is conjectured that at the MDR limit $\langle \sigma_{12} \rangle$ is negligible. This is based on the idea mentioned above about the stiffness of polymers at $\mathcal{W}e_S \to \infty$ plus the assumption that $\langle C_{22} \rangle$ becomes negligible at the same limit. Then, it is supposed that this behaviour is also valid under both the infinite Weissenberg and Reynolds number limits by taking carefully these limits, so that one is going along the universal MDR asymptotic line. Hence, one might expect an intermediate region $\delta_\nu \ll y \ll \delta$ of approximately constant Reynolds shear stress, i.e. $-\langle uv \rangle / u_\tau^2 \to 1$, implied by the balance of shear stresses when taking the limits of $y/\delta \to 0$ and $y/\delta_\nu \to \infty$ with the reasonable assumption that $\nu\beta \frac{\mathrm{d}}{\mathrm{d}y} \langle u \rangle \to 0$ for $y \gg \delta_\nu$. In summary, the classical turbulence generation by $-\langle uv \rangle$ seems to survive at the MDR limit, based on the above assumptions.

Polymer-turbulence dynamical interactions can be expressed through viscoelastic dissipation $\varepsilon_P \equiv \left\langle \sigma'_{ij} \partial_{x_j} u'_i \right\rangle$, which can either dissipate or produce turbulent kinetic energy. This dual nature is determined by the signs of σ'_{ij} and $\partial_{x_j} u'_i$. For HDR and MDR flows, $\int \varepsilon_P \, \mathrm{d}y$ becomes vital in the flow dynamics in proportion to $\int \mathcal{P} \, \mathrm{d}y$ and $\int \varepsilon_N \, \mathrm{d}y$ due to the vast inhibition of Reynolds shear stress and fluctuating strain rates, respectively. In particular, a different view of the near-wall dissipation dynamics is shown for HDR/MDR flows, with the maximum dissipation arising away from the wall. It is intriguing to note that ε_P follows a transitional pattern from LDR to HDR regime (see Fig. 6.10c) similar to u'_+ (see Fig. 6.4b) and $\langle C_{22} \rangle$ (see Fig. 6.6c). This characteristic behaviour is also reproduced on average in $\int \varepsilon_P \, \mathrm{d}y$, where its dissipative feature enhances in the LDR regime but attenuates for HDR/MDR flows, with the productive nature dominating for high $\%DR$. Thus, polymers get

somehow involved in the production dynamics of turbulent kinetic energy.

In view of the current viscoelastic DNS the following conceptual picture of drag reduction is deduced, which is an extension to and refinement of the mechanism proposed by Min et al. (2003b). Polymers in the near-wall region extract energy from the flow due to the uncoiling caused by the mean shear and release some portion of this stored elastic energy back to the flow by contracting as they move away from the wall. This transport of energy depends on Weissenberg number which determines the distribution of energy away from the wall. Ultimately, this process undermines the dynamics of near-wall turbulence. Note that polymers also unravel due to velocity fluctuations, as they move towards the core region of the flow, extracting again energy from the flow. This mechanism appears to be valid for all drag reduction regimes with the dissipative and productive elements of viscoelastic dissipation competing in an intermediate region $0 < y/\delta < 1$ for the different levels of $\%DR$. It is also observed that the correlation $\left\langle \sigma'_{1j}\partial_{x_j}u'_1 \right\rangle$ is able to resemble the dynamics of ε_P and that $\langle \sigma'_{11}\partial_{x_1}u'_1 \rangle$ and $\langle \sigma'_{13}\partial_{x_3}u'_1 \rangle$ are specifically the correlations responsible for the production of turbulent kinetic energy by polymers.

So far, in the limited context of the FENE-P model and at moderate Reynolds number DNS, the proposed phenomenology agrees with the majority of experimental and numerical data, where dampening of near-wall turbulence has long been speculated with various analyses and interpretations. Here, the transfer of energy from the flow to the polymers, its redistribution by the latter in the flow field and the prevalence of anisotropy over the components of $E = \frac{1}{2}\langle |\boldsymbol{u}'|^2 \rangle$ in the three Cartesian directions is suggested as a possible cause of drag reduction. However, further work is required to enhance our understanding.

In this respect, higher Reynolds number experiments and computations at MDR are necessary to shed light on the role of Reynolds shear stress and accordingly disprove or support the related arguments presented in this work. An important refinement specifically to the present mechanism would be the study of alignments between σ'_{ij} and $\partial_{x_j}u'_i$. This would uncover the detailed dynamics of polymer molecules in relation to the fluctuating strain rates that could lead to the clarification of the dual nature of ε_P. The understanding of the dynamics of viscoelastic dissipation and its scaling with Reynolds and Weissenberg numbers are crucial for the elucidation of the MDR asymptote.

Appendix A

Navier-Stokes solver

In this study, the Navier-Stokes equations (3.2) are discretised on a Cartesian grid using Finite Difference (FD) schemes. The method of FDs was preferred for this study rather than spectral methods (Kim et al., 1987) for the ease of compatibility with the peculiar numerical scheme for the FENE-P model (see section 5.2.1), which was constructed by FD schemes. A concise description of the numerical method of the Navier-Stokes solver follows. For more detailed description of the code the reader can refer to Laizet and Lamballais (2009).

A.1 Time advancement

The time integration of Eq. (3.2) is done using a three stage third-order Runge-Kutta scheme (RK3) (Williamson, 1980), based on the following projection or fractional step method (Peyret, 2002)

$$\frac{\boldsymbol{u}^* - \boldsymbol{u}^n}{\Delta t} = a_k \boldsymbol{F}^n + b_k \boldsymbol{F}^{n-1} \tag{A.1}$$

$$\frac{\boldsymbol{u}^{n+1} - \boldsymbol{u}^*}{\Delta t} = -c_k \boldsymbol{\nabla} \tilde{p}^{n+1} \tag{A.2}$$

with

$$\boldsymbol{F} = -\frac{1}{2}\left[\boldsymbol{\nabla}(\boldsymbol{u} \otimes \boldsymbol{u}) + (\boldsymbol{u} \cdot \boldsymbol{\nabla})\boldsymbol{u}\right] + \frac{1}{\mathcal{R}e_c}\boldsymbol{\Delta u} \tag{A.3}$$

and

$$\tilde{p}^{n+1} = \frac{1}{c_k \Delta t}\int_{t_n}^{t_{n+1}} p \, dt. \tag{A.4}$$

The coefficients a_k, b_k and c_k of the RK3 scheme are tabulated below.

Scheme	**Order**	a_k	b_k	c_k
RK3	$\sim O(\Delta t)^3$	$a_1 = 8/15$	$b_1 = 0$	$c_1 = a_1 + b_1$
		$a_2 = 5/12$	$b_2 = -17/60$	$c_2 = a_2 + b_2$
		$a_3 = 3/4$	$b_3 = -5/12$	$c_3 = a_3 + b_3$

Table A.1: Coefficients of the three stage Runge-Kutta scheme.

The incompressibility condition $\boldsymbol{\nabla} \cdot \boldsymbol{u}^{n+1} = 0$ is verified by solving the Poisson equation

$$\boldsymbol{\nabla} \cdot \boldsymbol{\nabla} \tilde{p}^{n+1} = \frac{\boldsymbol{\nabla} \cdot \boldsymbol{u}^*}{c_k \Delta t}. \tag{A.5}$$

A.2 Spatial discretisation in physical space

The spatial discretisation of the terms in the Navier-Stokes equations (3.2) is done using sixth-order compact schemes with "spectral-like resolution" (Lele, 1992), meaning that the schemes have high resolution, representing accurately a wide range of scales. In this code, the pressure is stored on a staggered grid and the velocities on a collocated grid (see Fig. A.1) to avoid any numerical instabilities (Ferziger and Perić, 2002). The approximation for the first derivative of a function $f(x)$ on a collocated

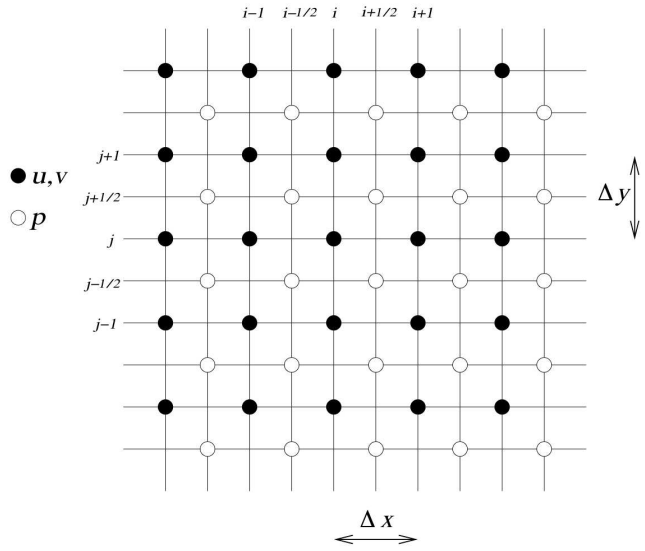

Figure A.1: Staggered grid. Courtesy Laizet and Lamballais (2009).

uniformly spaced grid with distance Δx can be expressed in terms of $f(x)$ as follows

$$\alpha f'_{i-1} + f'_i + \alpha f'_{i+1} = a\frac{f_{i+1} - f_{i-1}}{2\Delta x} + b\frac{f_{i+2} - f_{i-2}}{4\Delta x} \tag{A.6}$$

where $\alpha = 1/3$, a $= 14/9$ and b $= 1/9$ in order to achieve sixth-order accuracy (Lele, 1992). Similarly, for the second derivative of the function $f(x)$, one gets

$$\alpha f''_{i-1} + f''_i + \alpha f''_{i+1} = a\frac{f_{i+1} - 2f_i + f_{i-1}}{\Delta x^2} + b\frac{f_{i+2} - 2f_i + f_{i-2}}{4\Delta x^2} \tag{A.7}$$

with $\alpha = 2/11$, a $= 12/11$ and b $= 3/11$ for sixth-order accuracy (Lele, 1992). For the computation of the first derivative $f'_{i+1/2}$ on the nodes staggered by $\Delta x/2$ (see Fig. A.1) one needs the following expression for a compact scheme of the sixth-order

$$\alpha f'_{i-1/2} + f'_{i+1/2} + \alpha f'_{i+3/2} = a\frac{f_{i+1} - f_i}{\Delta x} + b\frac{f_{i+2} - f_{i-1}}{3\Delta x} \tag{A.8}$$

where $\alpha = 9/62$, a $= 63/62$ and b $= 17/62$. Although the staggered schemes are more accurate than the collocated (Lele, 1992), they are computationally more expensive, because they require a midpoint interpolation. The sixth order compact midpoint interpolation to obtain an approximation for $f_{i+1/2}$ is of the following form

$$\alpha f^I_{i-1/2} + f^I_{i+1/2} + \alpha f^I_{i+3/2} = a\frac{f_{i+1} - f_i}{2} + b\frac{f_{i+2} - f_{i-1}}{2} \tag{A.9}$$

with $\alpha = 3/10$, a $= 3/4$ and b $= 1/20$.

Generally, FD methods are restricted at the boundaries, since the stencil of the scheme can lie outside the boundaries, particularly when the stencil contains a lot of grid points, as in the case of sixth-order compact shemes, i.e. five-point stencil. In a channel flow, periodic boundary conditions are applied in the homogeneous directions and no-slip conditions at the walls (see section 2.3). In the periodic directions there is no problem implementing the full stencil at the boundaries, since one can use the adjacent nodes, however, these schemes are constrained at the wall boundaries. In this case, there are usually two main approaches, either to use the same stencil by "extending" the grid using ghost nodes and extrapolating or reduce the stencil by reducing the accuracy of the schemes near the boundaries. In this Navier-Stokes solver the latter approach has been implemented. Thus, third-order single sided

approximations are used for the first and second derivatives at the wall boundaries

$$f_1' + 2f_2' = \frac{1}{2\Delta x}(-5f_1 + 4f_2 + f_3) \tag{A.10}$$

$$f_1'' + 11f_2'' = \frac{1}{\Delta x^2}(13f_1 - 27f_2 + 15f_3 - f_4) \tag{A.11}$$

and for the adjacent grid points a three-point stencil was employed with the implementation of the following fourth-order Padé schemes

$$\frac{1}{4}f_1' + f_2' + \frac{1}{4}f_3' = \frac{3}{2}\frac{f_3 - f_1}{2\Delta x} \tag{A.12}$$

$$\frac{1}{10}f_1'' + f_2'' + \frac{1}{10}f_3'' = \frac{6}{5}\frac{f_3 - 2f_2 + f_1}{\Delta x^2}. \tag{A.13}$$

The computational cost for the convective and diffusive terms with the sixth-order compact FD schemes is the inversion of tridiagonal matrices and an extra computational cost comes for periodic boundary conditions, where cyclic matrices need to be inverted.

A.3 Nonlinear convection term

In this study, the convection term of the Navier-Stokes equations (3.2) has been implemented in its skew-symmetric form. Kravchenko and Moin (1997) noticed that numerical errors have different effects for the following different forms of the nonlinear term in the Navier-Stokes equations

$$\begin{aligned}
\textbf{Convective} &\equiv (\boldsymbol{u}\cdot\boldsymbol{\nabla})\boldsymbol{u} \\
\textbf{Divergence} &\equiv \boldsymbol{\nabla}(\boldsymbol{u}\otimes\boldsymbol{u}) \\
\textbf{Rotational} &\equiv \boldsymbol{u}\cdot\left(\boldsymbol{\nabla}\boldsymbol{u} - \boldsymbol{\nabla}\boldsymbol{u}^{\top}\right) + \frac{1}{2}\boldsymbol{\nabla}(\boldsymbol{u}\cdot\boldsymbol{u}) \\
\textbf{Skew-symmetric} &\equiv \frac{1}{2}[\boldsymbol{\nabla}(\boldsymbol{u}\otimes\boldsymbol{u}) + (\boldsymbol{u}\cdot\boldsymbol{\nabla})\boldsymbol{u}].
\end{aligned} \tag{A.14}$$

It was shown that for the divergence and convective forms, spectral methods are energy conserving only if dealiasing* is performed (Peyret, 2002). For the skew-symmetric and rotational forms, both spectral and FD methods are energy preserv-

*Cancellation of spurious modes generated by the nonlinear terms

ing. Moreover, turbulent channel flow computations were performed (Kravchenko and Moin, 1997) to show the effect on the numerical errors for each formulation of Eqs. (A.14). Kravchenko and Moin (1997) concluded that the skew-symmetric form had the smallest aliasing error and the differences between aliased and dealiased results were minimal among the various forms of the nonlinear term. Furthermore, the divergence form is conservative for FD schemes when a staggered grid and/or suitable averaging operators are used. However, staggered FD schemes are more expensive computationally than collocated, as it was noted in section A.2. Ultimately, due to the above reasons the skew-symmetric form was chosen to be used for this study.

A.4 Spatial discretisation in Fourier space

The spatial discretisation for the solution of Eq. (A.5) is done in Fourier space using discrete Fourier transforms. In the case of periodic function $f(x + L_x) = f(x)$ the Fourier transform takes the following form

$$\hat{f}_l = \frac{1}{n_x} \sum_{i=1}^{n_x} f_i e^{-ik_x x_i} \tag{A.15}$$

and its inverse

$$f_i = \sum_{l=-n_x/2}^{n_x/2-1} \hat{f}_l e^{-ik_x x_i} \tag{A.16}$$

where $k_x = 2\pi l/L_x$ is the wave number. However, in the case of symmetric boundary conditions, i.e. $f(x) = \pm f(-x)$ and $f(x + L_x) = \pm f(-x + L_x)$ at $x = 0$ and $x = L_x$, respectively

$$\hat{f}_l = \frac{1}{n_x} \sum_{i=1}^{n_x} f_i \cos(k_x x_i) \tag{A.17}$$

and its inverse

$$f_i = \frac{\hat{f}_0}{2} \sum_{l=1}^{n_x-1} \hat{f}_l \cos(k_x x_i) + (-1)^n \frac{\hat{f}_n}{2} \tag{A.18}$$

where $k_x = \pi l/L_x$. The equivalent shifted transforms ($i \to i+1/2$) for the staggering of the pressure can be also computed using Fast Fourier Transforms (FFTs) and this is shown in Canuto et al. (1988).

A.4.1 Spectral equivalence

The Fourier transform of the first derivative of a function f, given by Eq. (A.6) on a collocated grid, is equal to ik'_x times the transform of the original function given by Eq. (A.15), viz.

$$\hat{f}'_l = ik'_x \hat{f}_l \tag{A.19}$$

where k'_x is the modified wavenumber and according to Lele (1992) it is a function of the actual wavenumber k_x, i.e.

$$k'_x \Delta x = \frac{a \sin(k_x \Delta x) + (b/2) \sin(2k_x \Delta x)}{1 + 2\alpha \cos(k_x \Delta x)} \tag{A.20}$$

with the coefficients a, b and α being identical to the coefficients of Eq. (A.6). In the case of a staggered derivative approximation, the modified wavenumber takes the following form

$$k'_x \Delta x = \frac{2a \sin(k_x \Delta x/2) + (2b/3) \sin(3k_x \Delta x/2)}{1 + 2\alpha \cos(k_x \Delta x)} \tag{A.21}$$

where the coefficients a, b and α being the same as for Eq. (A.8).

Similarly, the Fourier transform of the midpoint interpolation is related to the transform of the function f, as follows

$$\hat{f}^I_l = T_x(k_x \Delta x) \hat{f}_l \tag{A.22}$$

where $T_x(k_x \Delta x)$ is the transfer function defined as

$$T_x(k_x \Delta x) = \frac{2a \cos(k_x \Delta x/2) + (2b/3) \cos(3k_x \Delta x/2)}{1 + 2\alpha \cos(k_x \Delta x)} \tag{A.23}$$

with the coefficients a, b and α correspond to the coefficients of Eq. (A.9).

A.5 Numerical solution of the Poisson equation

The solution of the Poisson equation is a necessary step in the projection method to satisfy the incompressibility condition, as was mentioned in section A.1. Equation (A.5) is the most computationally expensive part of the whole computation, due to

the non-local nature of the inverse Laplacian operator (see section 2.1), especially when using high-order numerical schemes in combination with iterative techniques. There are different techniques in the literature to tackle this problem (Ferziger and Perić, 2002; Peyret, 2002). In this code, the Poisson equation is solved using Fourier series, which is clearly much cheaper than iterative methods and easy to code using conventional FFTs. Using this method, one could think that the problem is constrained to periodic boundary conditions. However, the Fourier representation for the pressure treatment does not have to get restricted to the same boundary conditions with the Navier-Stokes equations. It has been shown that the solution of the Poisson equation using spectral methods introduces a second-order error locally by non-periodic boundary conditions (Wilhelmson and Ericksen, 1977; Swarztrauber, 1977). Even then, using the modified wavenumbers, the incompressibility can be enforced up to the machine accuracy, providing satisfactory results for the pressure (Laizet and Lamballais, 2009).

The Poisson step in this fractional step method starts with the computation of the divergence. To preserve compatibility between the discrete differentiation operators in physical and Fourier spaces for the pressure, the calculation of $\boldsymbol{\nabla} \cdot \mathbf{u}^*$ must be done using the staggered schemes, preserving the set of boundary conditions considered. Then, the following 3D discrete Fourier transform and its inverse are applied using conventional FFT routines to solve Eq. (A.5) in Fourier space,

$$\hat{\tilde{p}}_{lmn} = \frac{1}{n_x n_y n_z} \sum_i \sum_j \sum_k p_{ijk} W_x(k_x x_i) W_y(k_y y_j) W_z(k_z z_k) \tag{A.24}$$

$$p_{ijk} = \sum_l \sum_m \sum_n \hat{\tilde{p}}_{lmn} W_x(-k_x x_i) W_y(-k_y y_j) W_z(-k_z z_k) \tag{A.25}$$

where the sums, the base functions (W_x, W_y, W_z) and the wave numbers (k_x, k_y, k_z) correspond to the ones defined in section A.4.

Now, let $D = \boldsymbol{\nabla} \cdot \mathbf{u}^*$. Then, taking the Fourier transform of the Poisson equation

$$F_{lmn} \hat{\tilde{p}}^{n+1}_{lmn} = \hat{D}_{lmn} \Rightarrow \hat{\tilde{p}}^{n+1}_{lmn} = \frac{\hat{D}_{lmn}}{F_{lmn}} \tag{A.26}$$

where the factor F_{lmn} depends on the grid configuration and for the staggered case it must take into account the midpoint interpolation through the use of the transfer

functions, i.e.

$$F_{lmn} = -\left[\left(k'_x T_y T_z\right)^2 + \left(k'_y T_x T_z\right)^2 + \left(k'_z T_x T_y\right)^2\right] \Delta t. \tag{A.27}$$

Finally, to compute the pressure in the physical space, the inverse Fourier transform Eq. (A.25) is applied and the pressure gradient $\boldsymbol{\nabla}\tilde{p}^{n+1}$ can be obtained using the staggered compact schemes of section A.2.

A.6 Non-uniform grids using Fourier Transforms

In this code, the Fourier method provides favourable properties such as spectral accuracy and fast solution of the Poisson equation (A.5). However, the discrete Fourier transform is restricted to the use of an equally spaced co-ordinate in a finite domain. In order to overcome this constraint, first Cain et al. (1984) and then Avital et al. (2000) suggested a grid stretching technique that maps an equally space co-ordinate in the computational space to a non-equally spaced co-ordinate in the physical space.

In detail, let x be the physical space co-ordinate and let the computational co-ordinate s to be introduced through a mapping

$$x = h(s) = -\beta \cot(\pi s), \;\; 0 \leqslant s < 1 \text{ and } -\infty \leqslant x < \infty. \tag{A.28}$$

Then the first and second derivatives of a function f in the two co-ordinate systems are related via the chain rule, as follows

$$\frac{\partial f}{\partial x} = \frac{\partial f}{\partial s}\frac{\mathrm{d}s}{\mathrm{d}x} = \frac{1}{h'}\frac{\partial f}{\partial s} \tag{A.29}$$

$$\frac{\partial^2 f}{\partial x^2} = \frac{\partial^2 f}{\partial s^2}\left(\frac{\mathrm{d}s}{\mathrm{d}x}\right)^2 + \frac{\partial f}{\partial s}\frac{\mathrm{d}^2 s}{\mathrm{d}x^2} = \frac{1}{h'^2}\frac{\partial^2 f}{\partial s^2} + \frac{h''}{h'^3}\frac{\mathrm{d}^2 s}{\mathrm{d}x^2}. \tag{A.30}$$

Hence, the spatial derivatives are first calculated using the FFT and then multiplied

by the stretching ratio of the mapping to yield the derivatives in the physical space

$$\begin{aligned}\alpha\frac{\partial f}{\partial x}\bigg|_{i-1} + \frac{\partial f}{\partial x}\bigg|_{i} + \alpha\frac{\partial f}{\partial x}\bigg|_{i+1} &= \alpha h'_{i-1}\frac{\partial f}{\partial s}\bigg|_{i-1} + h'_i\frac{\partial f}{\partial s}\bigg|_{i} + \alpha h'_{i+1}\frac{\partial f}{\partial s}\bigg|_{i+1} \\ &= a\frac{f_{i+1} - f_{i-1}}{\Delta s} + b\frac{f_{i+2} - f_{i-2}}{\Delta s} \qquad \text{(A.31)}\end{aligned}$$

where $h'_i = \partial_s h(s_i)$ and α, a and b take the values previously denoted in section A.2. The final result yields alias-free differentiation operators (Cain et al., 1984; Avital et al., 2000).

Appendix B

Numerical method for the computation of stagnation points

This study of turbulent channel flow focuses on stagnation points of the fluctuating velocity field, i.e.

$$\boldsymbol{u}'(\boldsymbol{x},t) \equiv \boldsymbol{u}(\boldsymbol{x},t) - \langle \boldsymbol{u} \rangle = 0 \tag{B.1}$$

where $\langle\ \rangle$ denotes here an average in space over the homogeneous directions x and z at a particular instant in time. These zero-velocity points are Galilean invariant and result from the intersections of the three random surfaces $u'(\boldsymbol{x},t) = 0$, $v'(\boldsymbol{x},t) = 0$ and $w'(\boldsymbol{x},t) = 0$. Intersections of two random surfaces gives lines and the intersections of these lines with a third random surface gives points.

A root finding method is required to obtain where in space the random function $\boldsymbol{u}'(\boldsymbol{x},t)$ is locally zero. Here, the iterative Newton-Raphson method is applied

$$\boldsymbol{x}_{new} = \boldsymbol{x}_{old} + \delta\boldsymbol{x} \text{ with } [\boldsymbol{\nabla u}']_{\mathcal{L}}\, \delta\boldsymbol{x} = -\boldsymbol{u}'_{\mathcal{L}} \tag{B.2}$$

where $\boldsymbol{\nabla u}'(\boldsymbol{x},t) \equiv \boldsymbol{\nabla u}(\boldsymbol{x},t) - \langle \boldsymbol{\nabla u} \rangle$ and the subscript $\mathcal{L}$ stands for an interpolated quantity. The interpolation of the velocity and its gradient was done using fourth-order Lagrangian interpolation (Press et al., 1996). The particular choice of the interpolation was chosen based on robustness, accuracy and computational efficiency. The 3×3 linear system of equations was solved for $\delta\boldsymbol{x}$ simply using the Cramer's

rule

$$\delta \boldsymbol{x} = -\frac{\left[\det(\boldsymbol{u}'_{\mathcal{L}}, \frac{\partial \boldsymbol{u}'}{\partial y}\big|_{\mathcal{L}}, \frac{\partial \boldsymbol{u}'}{\partial z}\big|_{\mathcal{L}}), \det(\frac{\partial \boldsymbol{u}'}{\partial x}\big|_{\mathcal{L}}, \boldsymbol{u}'_{\mathcal{L}}, \frac{\partial \boldsymbol{u}'}{\partial z}\big|_{\mathcal{L}}), \det(\frac{\partial \boldsymbol{u}'}{\partial x}\big|_{\mathcal{L}}, \frac{\partial \boldsymbol{u}'}{\partial y}\big|_{\mathcal{L}}, \boldsymbol{u}'_{\mathcal{L}})\right]}{\det(\frac{\partial \boldsymbol{u}'}{\partial x}\big|_{\mathcal{L}}, \frac{\partial \boldsymbol{u}'}{\partial y}\big|_{\mathcal{L}}, \frac{\partial \boldsymbol{u}'}{\partial z}\big|_{\mathcal{L}})} \tag{B.3}$$

assuming that $\det(\frac{\partial \boldsymbol{u}'}{\partial x}\big|_{\mathcal{L}}, \frac{\partial \boldsymbol{u}'}{\partial y}\big|_{\mathcal{L}}, \frac{\partial \boldsymbol{u}'}{\partial z}\big|_{\mathcal{L}}) \neq 0$.

The Newton-Raphson method gives a very rapid local convergence to a root if the initial guess is sufficiently good. So, to have a chance at good starting points, these were taken midway between two consecutive grid points throughout the computational domain. It is well known that different initial guesses can converge to the same solution, due to the unpredictable global convergence properties of this iterative method. To avoid this issue the root finding was bounded no further than the neighbouring computational cells and it was also ensured that no more than one stagnation point exists in a cell, which is what should be expected from a smooth velocity field of a well resolved DNS.

This method was also compared to an algorithm proposed in Schmelcher and Diakonos (1998) for the detection of unstable periodic orbits in chaotic dynamical systems, which has good global convergence due to its attracting nature. This method is based on a universal set of linear transformations, which transform unstable fixed points to stable ones whilst mainting their positions. However, this method can be expensive in more than two dimensions and this is the reason why Newton-Raphson was chosen here, which is as accurate.

The number of zero-velocity points N_s are computed within thin slabs of dimensions $L_x \times \delta_y \times L_z$, with $\delta_y \propto \delta_\nu$, parallel to the channel's wall. Time averages of N_s were taken by repeating the same procedure for several time instances.

Appendix C

Kronecker and Vec operator

The Kronecker product of an $n \times n$ matrix $\boldsymbol{A}$ with the $n \times n$ identity matrix $\boldsymbol{I}$ is an $n^2 \times n^2$ matrix, taking the following form

$$\boldsymbol{A} \otimes \boldsymbol{I} = \begin{pmatrix} A_{11}\boldsymbol{I} & A_{12}\boldsymbol{I} & \cdots & A_{1n}\boldsymbol{I} \\ A_{21}\boldsymbol{I} & A_{22}\boldsymbol{I} & \cdots & A_{1n}\boldsymbol{I} \\ \vdots & \vdots & \ddots & \vdots \\ A_{n1}\boldsymbol{I} & A_{n2}\boldsymbol{I} & \cdots & A_{nn}\boldsymbol{I} \end{pmatrix} \tag{C.1}$$

and

$$\boldsymbol{I} \otimes \boldsymbol{A} = \begin{pmatrix} I_{11}\boldsymbol{A} & & & \\ & I_{22}\boldsymbol{A} & & \\ & & \ddots & \\ & & & I_{nn}\boldsymbol{A} \end{pmatrix} \tag{C.2}$$

The vec operator applied on an $m \times n$ matrix $\boldsymbol{B}$ stacks the columns into a vector, viz.

$$\text{vec}(\boldsymbol{B}) = (B_{11}, B_{12}, \cdots, B_{1n}, B_{21}, B_{22}, \cdots, B_{2n}, \cdots\cdots, B_{m1}, B_{m2}, \cdots, B_{mn})^\top \tag{C.3}$$

Bibliography

Arfken, G. B. and Weber, H. J. *Mathematical methods for physicists*. Academic press New York, 2000.

Aris, R. *Vectors, tensors, and the basic equations of fluid mechanics*. Prentice-Hall, 1962.

Avital, E. J., Sandham, N. D., and Luo, K. H. Stretched cartesian grids for solution of the incompressible Navier-Stokes equations. *Int. J. Numer. Methods Fluids*, 33: 897–918, 2000.

Barenblatt, G. I. *Scaling, self-similarity, and intermediate asymptotics*. Cambridge University Press, 1996.

Batchelor, G. K. *An introduction to fluid mechanics*. Cambridge University Press, 1967.

Batchelor, G. K. *The theory of homogeneous turbulence*. Cambridge University Press, 1982.

Benzi, R., Ching, E. S. C., Lo, T. S., L'vov, V. S., and Procaccia, I. Additive equivalence in turbulent drag reduction by flexible and rodlike polymers. *Phys. Rev. E*, 72:16305, 2005.

Benzi, R., De Angelis, E., L'vov, V. S., Procaccia, I., and Tiberkevich, V. Maximum drag reduction asymptotes and the cross-over to the newtonian plug. *J. Fluid Mech.*, 551:185 – 195, 2006.

Bewersdorff, H. W. Effect of a centrally injected polymer thread on drag in pipe flow. *Rheol. Acta*, 21:587 – 589, 1982.

Bewersdorff, H. W. Heterogeneous drag production in turbulent pipe flow. *Rheologica Acta*, 23(5):522 – 43, 1984.

Bird, R. B., Curtis, C. F., Armstrong, R. C., and Hassager, O. *Dynamics of Polymeric Liquids*, volume 2: Kinetic Theory. John Wiley and Sons, 1987.

Bird, R. B., Dotson, P. J., and Johnson, N. L. Polymer solution rheology based on a finitely extensible bead–spring chain model. *J. Non-Newtonian Fluid Mech.*, 7 (2-3):213 – 235, 1980.

Birkhoff, G. and Mac Lane, S. *A Survey of Modern Algebra*. Macmillan Publishing Co., 1977.

Bismarck, A., Chen, L., Griffen, J. M., Hewitt, G. F., and Vassilicos, J. C. Polymer drag reduction. *Heat Exchanger Design Handbook*, 11(3):21421, 2008.

Bradshaw, P. 'Inactive' motion and pressure fluctuations in turbulent boundary layers. *J. Fluid Mech.*, 30(02):241–258, 1967.

Brouwers, J. J. H. Dissipation equals production in the log layer of wall-induced turbulence. *Phys. Fluids*, 19(10):101702, 2007.

Cain, A. B., Ferziger, J. H., and Reynolds, W. C. Discrete orthogonal function expansions for non-uniform grids using the fast Fourier transform. *J. Comput. Phys.*, 56:272–286, 1984.

Cantwell, B. J. Organized motion in turbulent flow. *Ann. Rev. Fluid Mech.*, 13(1): 457–515, 1981.

Canuto, C., Hussaini, M., Quarteroni, A., and Zang, T. A. *Spectral Methods in Fluid Dynamics*. Springer-Verlag, 1988.

Chakraborty, P., Balachandar, S., and Adrian, R. J. On the relationships between local vortex identification schemes. *J. Fluid Mech.*, 535:189–214, 2005.

Chandrasekhar, S. Stochastic problems in physics and astronomy. *Rev. Mod. Phys.*, 15(1):1–89, Jan 1943.

Choi, H., Moin, P., and Kim, J. Active turbulence control for drag reduction in wall-bounded flows. *J. Fluid Mech.*, 262:75–110, 1994.

Chorin, A. J. and Marsden, J. E. *A mathematical introduction to fluid mechanics*. Springer-Verlag, 1979.

Courant, R., Friedrichs, K., and Lewy, H. On the partial difference equations of mathematical physics. *IBM J.*, 11:215–234, 1967.

Davidson, P. A. *Turbulence: an introduction for scientists and engineers*. Oxford University Press, 2004.

Dávila, J. and Vassilicos, J. C. Richardson's pair diffusion and the stagnation point structure of turbulence. *Phys. Rev. Lett.*, 91:144501, 2003.

De Angelis, E., Casciola, C. M., Benzi, R., and Piva, R. Homogeneous isotropic turbulence in dilute polymers. *J. Fluid Mech.*, 531:1–10, 2005.

De Angelis, E., Casciola, C. M., L'vov, V. S., Pomyalov, A., Procaccia, I., and Tiberkevich, V. Drag reduction by a linear viscosity profile. *Phys. Rev. E*, 70(5): 055301, 2004.

De Angelis, E., Casciola, C. M., and Piva, R. DNS of wall turbulence: dilute polymers and self-sustaining mechanisms. *Computers & Fluids*, 31(4-7):495 – 507, 2002.

De Gennes, P. G. *Introduction to polymer dynamics*. Cambridge University Press, 1990.

Dean, R. B. Reynolds number dependence of skin friction and other bulk flow variables in two-dimensional rectangular duct flow. *ASME J. Fluids Eng.*, 100:215, 1978.

Dennis, J. and Schnabel, R. *Numerical methods for unconstrained optimization and nonlinear equations*. Prentice-Hall, 1983.

Dimitropoulos, C. D., Dubief, Y., Shaqfeh, E. S. G., Moin, P., and Lele, S. K. Direct numerical simulation of polymer-induced drag reduction in turbulent boundary layer flow. *Phys. Fluids*, 17(1):011705 – 011705, 2005.

Dimitropoulos, C. D., Dublief, Y., Shaqfeh, E. S. G., and Moin, P. Direct numerical simulation of polymer-induced drag reduction in turbulent boundary layer flow of inhomogeneous polymer solutions. *J. Fluid Mech.*, 566:153 – 162, 2006.

Dimitropoulos, C. D., Sureshkumar, R., and Beris, A. N. Direct numerical simulation of viscoelastic turbulent channel flow exhibiting drag reduction: effect of the variation of rheological parameters. *J. Non-Newtonian Fluid Mech.*, 79:433 – 68, 1998.

Doering, C. R. and Gibbon, J. D. *Applied analysis of the Navier-Stokes equations*. Cambridge University Press, 1995.

Doi, M. and Edwards, S. F. *The Theory of Polymer Dynamics*. Oxford Science Publications, 1986.

Dubief, Y., Terrapon, V., White, C., Shaqfeh, E., Moin, P., and Lele, S. New answers on the interaction between polymers and vortices in turbulent flows. *Flow, Turbulence and Combustion*, 74(4):311–329, 2005.

Dubief, Y., White, M. C., Terrapon, V. E., Shaqfeh, E. S. G., Moin, P., and Lele, S. K. On the coherent drag-reducing and turbulence-enhancing behaviour of polymers in wall flows. *J. Fluid Mech.*, 514:271–280, 2004.

Dupret, F. and Marchal, J. Loss of evolution in the flow of viscoelastic fluids. *J. Non-Newtonian Fluid Mech.*, 20:143 – 171, 1986.

Falconer, K. J. *Fractal Geometry - Mathematical Foundations and Applications* . Wiley New York, 1990.

Ferziger, J. H. and Perić, M. *Computational methods for fluid dynamics*. Springer New York, 2002.

Flory, P. J. *Statistical Mechanics of Chain Molecules*. Hanser Publishers, 1989.

Frisch, U. *Turbulence: the legacy of A. N. Kolmogorov*. Cambridge University Press, 1995.

George, W. K. Is there a universal log law for turbulent wall-bounded flows? *Phil. Trans. R. Soc. A*, 365(1852):789–806, 2007.

Glendinning, P. *Stability, instability, and chaos: An introduction to the theory of nonlinear differential equations*. Cambridge University Press, 1994.

Goto, S. and Vassilicos, J. C. Particle pair diffusion and persistent streamline topology in two-dimensional turbulence. *New J. Phys.*, 6:65, 2004.

Goto, S. and Vassilicos, J. C. The dissipation rate coefficient of turbulence is not universal and depends on the internal stagnation point structure. *Phys. Fluids*, 21 (3):035104, 2009.

Gyr, A. and Bewersdorff, H. W. *Drag Reduction of Turbulent Flows by Additives*. Kluwer Academic Publishers, 1995.

Handler, R. A., Housiadas, K. D., and Beris, A. N. Karhunen-Loeve representations of turbulent channel flows using the method of snapshots. *Int. J. Numer. Methods Fluids*, 52:1339–1360, 2006.

Head, M. R. and Bandyopadhyay, P. New aspects of turbulent boundary-layer structure. *J. Fluid Mech.*, 107:297–338, 1981.

Holmes, P., Lumley, J. L., and Berkooz, G. *Turbulence, coherent structures, dynamical systems and symmetry*. Cambridge University Press, 1998.

Housiadas, K. D. and Beris, A. N. Polymer-induced drag reduction: Effects of the variations in elasticity and inertia in turbulent viscoelastic channel flow. *Phys. Fluids*, 15(8):2369 – 2384, 2003.

Hoyas, S. and Jiménez, J. Scaling of the velocity fluctuations in turbulent channels up to $Re_\tau = 2003$. *Phys. Fluids*, 18:011702, 2006. URL `http://torroja.dmt.upm.es`.

Hu, Z. W., Morfey, C. L., and Sandham, N. D. Wall pressure and shear stress spectra from direct simulations of channel flow. *AIAA Journal*, 44(7):1541, 2006. URL `http://www.dnsdata.afm.ses.soton.ac.uk`.

Hulsen, M. A. A sufficient condition for a positive definite configuration tensor indifferential models. *J. Non-Newtonian Fluid Mech.*, 38(1):93 – 100, 1990.

Ilg, P., De Angelis, E., Karlin, I., Casciola, C., and Succi, S. Polymer dynamics in wall turbulent flow. *Europhys. Lett.*, 58(4):616 – 622, 2002.

Iwamoto, K., Suzuki, Y., and Kasagi, N. Reynolds number effect on wall turbulence: Toward effective feedback control. *Int. J. Heat Fluid Flow*, 23:678, 2002. URL `http://www.thtlab.t.u-tokyo.ac.jp`.

Jiménez, J. and Moin, P. The minimal flow unit in near-wall turbulence. *J. Fluid Mech.*, 225:213–240, 1991.

Jin, S. and Collins, L. R. Dynamics of dissolved polymer chains in isotropic turbulence. *New Journal of Physics*, 9(10):360, 2007.

Joseph, D. and Saut, J. Change of type and loss of evolution in the flow of viscoelastic fluids. *J. Non-Newtonian Fluid Mech.*, 20:117 – 141, 1986.

Joseph, D. D. *Fluid dynamics of viscoelastic liquids*. Springer-Verlag, 1990.

Kalelkar, C., Govindarajan, R., and Pandit, R. Drag reduction by polymer additives in decaying turbulence. *Phys. Rev. E*, 72(1):17301 – 1, 2005.

Kemp, M. *Leonardo*. Oxford University Press, 2004.

Kim, H. T., Kline, S. J., and Reynolds, W. C. The production of turbulence near a smooth wall in a turbulent boundary layer. *J. Fluid Mech.*, 50:133–160, 1971.

Kim, J., Moin, P., and Moser, R. Turbulence statistics in fully developed channel flow at low Reynolds number. *J. Fluid Mech.*, 177:133 – 66, 1987.

Kim, K., Adrian, R. J., Balachandar, S., and Sureshkumar, R. Dynamics of hairpin vortices and polymer-induced turbulent drag reduction. *Phys. Rev. Lett.*, 100: 134504, 2008.

Kim, K., Li, C.-F., Sureshkumar, R., Balachandar, S., and Adrian, R. J. Effects of polymer stresses on eddy structures in drag-reduced turbulent channel flow. *J. Fluid Mech.*, 584:281 – 299, 2007.

Kline, S., Reynolds, W., Schraub, F., and Runstadler, P. The structure of turbulent boundary layers. *J. Fluid Mech.*, 30(04):741–773, 1967.

Kolmogorov, A. N. The local structure of turbulence in incompressible viscous fluid for very large Reynolds number. *Doklady Akademii Nauk SSSR*, 30:301–305, 1941.

Kolmogorov, A. N. A refinement of previous hypotheses concerning the local structure of turbulence in a viscous incompressible fluid at high Reynolds number. *J. Fluid Mech.*, 13:82–85, 1962.

Kravchenko, A. G. and Moin, P. On the effect of numerical errors in large eddy simulations of turbulent flows. *J. Comput. Phys.*, 131:310 – 22, 1997.

Kurganov, A. and Tadmor, E. New high-resolution central schemes for nonlinear conservation laws and convection-diffusion equations. *J. Comput. Phys.*, 160:241 – 82, 2000.

Laizet, S. and Lamballais, E. High-order compact schemes for incompressible flows: A simple and efficient method with quasi-spectral accuracy. *J. Comput. Phys.*, 228 (16):5989 – 6015, 2009.

Larson, R. *Constitutive Equations for Polymer Melts and Solutions*. Butterworths, 1988.

L'vov, V. S., Pomyalov, A., Procaccia, I., and Tiberkevich, V. Polymer stress tensor in turbulent shear flows. *Phys. Rev. E*, 71(1):016305, 2005.

Lele, S. K. Compact finite difference schemes with spectral-like resolution. *J. Comput. Phys.*, 103:16–42, 1992.

Lesieur, M. *Turbulence in Fluids*. Kluwer Academic Publishers, 1997.

LeVeque, R. *Finite volume methods for hyperbolic problems*. Cambridge University Press, 2002.

LeVeque, R. *Finite Difference Methods for Ordinary and Partial Differential Equations: Steady-State and Time-Dependent Problems*. Society for Industrial and Applied Mathematics (SIAM), 2007.

Li, C.-F., Sureshkumar, R., and Khomami, B. Influence of rheological parameters on polymer induced turbulent drag reduction. *J. Non-Newtonian Fluid Mech.*, 140 (1-3):23 – 40, 2006.

Liepmann, H. W. Aspects of the turbulence problem. *Z. Angew. Math. Phys.*, 3(5): 321, 1952.

Lumley, J. Drag reduction by additives. *Ann. Rev. Fluid Mech.*, 1:367–384, 1969.

Lumley, J. L. Drag reduction in turbulent flow by polymer additives. *J. Polym. Sci. Macromol. Rev.*, 7:263 – 90, 1973.

Massah, H. and Hanratty, T. J. Added stresses because of the presence of FENE-P bead-spring chains in a random velocity field. *J. Fluid Mech.*, 337:67–101, 1997.

Massah, H., Kontomaris, K., Schowalter, W. R., and Hanratty, T. J. The configurations of a FENE bead-spring chain in transient rheological flows and in a turbulent flow. *Phys. Fluids A*, 5(4):881–890, 1993.

Mazellier, N. and Vassilicos, J. C. The turbulence dissipation constant is not universal because of its universal dependence on large-scale flow topology. *Phys. Fluids*, 20 (1):015101, 2008.

McComb, W. D. *The Physics of Fluid Turbulence*. Oxford University Press, 1992.

McComb, W. D. and Rabie, L. H. Development of local turbulent drag reduction due to nonuniform polymer concentration. *Phys. Fluids*, 22(1):183–185, 1979.

McKeon, B., editor. *Theme issue on Scaling and structure in high Reynolds number wall-bounded flows*, volume 365. Phil. Trans. R. Soc. A, 2007.

McKeon, B. J., Li, J., Jiang, W., Morrison, J. F., and Smits, A. J. Further observations on the mean velocity distribution in fully developed pipe flow. *J. Fluid Mech.*, 501:135–147, 2004.

Min, T., Choi, H., and Yoo, J. Y. Maximum drag reduction in a turbulent channel flow by polymer additives. *J. Fluid Mech.*, 492:91–100, 2003a.

Min, T., Kang, S. M., Speyer, J. L., and Kim, J. Sustained sub-laminar drag in a fully developed channel flow. *J. Fluid Mech.*, 558:309–318, 2006.

Min, T., Yoo, J. Y., and Choi, H. Effect of spatial discretization schemes on numerical solutions of viscoelastic fluid flows. *J. Non-Newtonian Fluid Mech.*, 100:27–47, 2001.

Min, T., Yoo, J. Y., Choi, H., and Joseph, D. D. Drag reduction by polymer additives in a turbulent channel flow. *J. Fluid Mech.*, 486:213–38, 2003b.

Moin, P. and Kim, J. On the numerical solution of time-dependent viscous incompressible fluid flows involving solid boundaries. *J. Comput. Phys.*, 35(3):381–392, 1980.

Moser, R. D., Kim, J., and Mansour, N. N. Direct numerical simulation of turbulent channel flow up to $Re_\tau = 590$. *Phys. Fluids*, 11(4):943, 1999. URL `http://turbulence.ices.utexas.edu`.

Nagib, H. M. and Chauhan, K. A. Variations of von Kármán coefficient in canonical flows. *Phys. Fluids*, 20(10):101518, 2008.

Oertel, H. *Prandtl's essentials of fluid mechanics*. Springer, second edition, 2004.

Öttinger, H. C. *Stochastic processes in polymeric fluids*. Springer Berlin, 1996.

Ottino, J. M. *The kinematics of mixing: stretching, chaos, and transport*. Cambridge University Press, 1989.

Owens, R. G. and Phillips, T. N. *Computational Rheology*. Imperial College Press, 2002.

Papoulis, A. *Probability, Random Variables, and Stochastic Processes*. McGraw-Hill, 1991.

Perlekar, P., Mitra, D., and Pandit, R. Manifestations of drag reduction by polymer additives in decaying, homogeneous, isotropic turbulence. *Phys. Rev. Lett.*, 97(26): 264501 – 1, 2006.

Perry, A. E. and Chong, M. S. On the mechanism of wall turbulence. *J. Fluid Mech.*, 119:173 – 217, 1982.

Perry, A. E. and Chong, M. S. A description of eddying motions and flow patterns using critical-point concepts. *Ann. Rev. Fluid Mech.*, 19:125 – 155, 1987.

Perry, A. E., Henbest, S., and Chong, M. S. A theoretical and experimental study of wall turbulence. *J. Fluid Mech.*, 165:163–199, 1986.

Perry, A. E. and Marusic, I. A wall-wake model for the turbulence structure of boundary layers. Part 1. Extension of the attached eddy hypothesis. *J. Fluid Mech.*, 298:361–388, 1995.

Peterlin, A. Streaming birefringence of soft linear macromolecules with finite chain length. *Polymer*, 2:257–264, 1961.

Petersen, K. B. and Pedersen, M. S. *The Matrix Cookbook*. Technical University of Denmark, 2008.

Peyret, R. *Spectral methods for incompressible viscous flow*. Springer-Verlag, 2002.

Pope, S. B. *Turbulent Flows*. Cambridge University Press, 2000.

Prandtl, L. Uber die ausgebildete Turbulenz. *Zeitschrift für Angewandte Mathematik und Mechanik*, 5:136, 1925.

Press, W. H., Teukolsky, S. A., Vetterling, W. T., and Flannery, B. P. *Numerical recipes in Fortran 77*. Cambridge University Press, 1996.

Procaccia, I., L'vov, V. S., and Benzi, R. Colloquium: Theory of drag reduction by polymers in wall-bounded turbulence. *Rev. Mod. Phys.*, 80(1):225, 2008.

Ptasinski, P. K., Boersma, B. J., Nieuwstadt, F. T. M., Hulsen, M. A., Van den Brule, H. A. A., and Hunt, J. C. R. Turbulent channel flow near maximum drag reduction: simulations, experiments and mechanisms. *J. Fluid Mech.*, 490:251 – 91, 2003.

Ptasinski, P. K., Nieuwstadt, F. T. M., van den Brule, B. H. A. A., and Hulsen, M. A. Experiments in turbulent pipe flow with polymer additives at maximum drag reduction. *Flow, Turbul. Combust.*, 66:159 – 82, 2001.

Reynolds, O. An experimental investigation of the circumstances which determine whether the motion of water shall be direct or sinuous, and of the law of resistance in parallel channels. *Phil. Trans. Royal Soc. London*, 174:935–982, 1883.

Robinson, S. K. Coherent motions in the turbulent boundary layer. *Ann. Rev. Fluid Mech.*, 23(1):601–639, 1991.

Ruelle, D. *Chaotic evolution and strange attractors*. Cambridge University Press, 1992.

Saffman, P. G. *Vortex dynamics*. Cambridge University Press, 1995.

Salazar, J. P. L. C. and Collins, L. R. Two-particle dispersion in isotropic turbulent flows. *Ann. Rev. Fluid Mech.*, 41(1):405–432, 2009.

Schlichting, H. and Gersten, K. *Boundary-layer theory*. Springer, 2000.

Schmelcher, P. and Diakonos, F. K. General approach to the localization of unstable periodic orbits in chaotic dynamical systems. *Phys. Rev. E*, 57(3):2739–2746, 1998.

Sibilla, S. and Baron, A. Polymer stress statistics in the near-wall turbulent flow of a drag-reducing solution. *Phys. Fluids*, 14(3):1123–1136, 2002.

Sreenivasan, K. R. and White, C. M. The onset of drag reduction by dilute polymer additives, and the maximum drag reduction asymptote. *J. Fluid Mech.*, 409:149 – 64, 2000.

Strang, G. *Linear algebra and its applications*. Thompson Learning, Inc., 1988.

Sureshkumar, R. and Beris, A. N. Effect of artificial stress diffusivity on the stability of numerical calculations and the flow dynamics of time-dependent viscoelastic flows. *J. Non-Newtonian Fluid Mech.*, 60:53–80, 1995.

Sureshkumar, R., Beris, A. N., and Handler, R. A. Direct numerical simulation of the turbulent channel flow of a polymer solution. *Phys. Fluids*, 9:743 – 55, 1997.

Swarztrauber, P. N. The methods of cyclic reduction, Fourier analysis and the FACR algorithm for the discrete solution of Poisson's equation on a rectangle. *SIAM Review*, 19:490–501, 1977.

Tabor, M. and de Gennes, P. G. A cascade theory of drag reduction. *Europhys. Lett.*, (7):519 – 522, 1986.

Taylor, G. I. Statistical theory of turbulence. *Proceedings of the Royal Society of London. Series A, Mathematical and Physical Sciences*, 151(873):421–444, 1935.

Tennekes, H. and Lumley, J. *A first course in turbulence*. MIT press, 1972.

Terrapon, V. E., Dubief, Y., Moin, P., Shaqfeh, E. S. G., and Lele, S. K. Simulated polymer stretch in a turbulent flow using Brownian dynamics. *J. Fluid Mech.*, 504: 61 – 71, 2004.

Toms, B. A. Some observations on the flow of linear polymer solutions through straight tubes at large Reynolds numbers. volume 2 of *Proceedings 1st International Congress on Rheology*, pages 135–141, Amsterdam, 1948. North-Holland.

Townsend, A. A. Equilibrium layers and wall turbulence. *J. Fluid Mech.*, 11(01): 97–120, 1961.

Townsend, A. A. *The Structure of Turbulent Shear Flow.* Cambridge University Press, 1976.

Tsinober, A. *An informal introduction to turbulence.* Kluwer Academic Publishers, 2002.

Vaithianathan, T., Brasseur, J. G., and Collins, L. R. *Personal communication.* Cornell University, USA, 2007.

Vaithianathan, T., Robert, A., Brasseur, J. G., and Collins, L. R. An improved algorithm for simulating three-dimensional, viscoelastic turbulence. *J. Non-Newtonian Fluid Mech.*, 140:3–22, 2006.

Van Heel, A. P. G., Hulsen, M. A., and Van den Brule, B. H. A. A. On the selection of parameters in the FENE-P model. *J. Non-Newtonian Fluid Mech.*, 75:253 – 271, 1998.

Virk, P. S. Drag reduction fundamentals. *AIChE Journal*, 21:625 – 656, 1975.

Virk, P. S., Merrill, E. W., Mickley, H. S., Smith, K. A., and Mollo-Christensen, E. L. The Toms phenomenon: turbulent pipe flow of dilute polymer solutions. *J. Fluid Mech.*, 30:305–328, 1967.

Virk, P. S., Sherman, D. C., and Wagger, D. L. Additive equivalence during turbulent drag reduction. *AIChE Journal*, 43:3257 – 3259, 1997.

von Kármán, T. Mechanische ähnlichkeit und turbulenz. *Nach. Ges. Wiss. Gottingen, Proc. Third Int. Congr. Applied Mechanics*, page 85, 1930.

Warholic, M. D., Massah, H., and Hanratty, T. J. Influence of drag-reducing polymers on turbulence: effects of Reynolds number, concentration and mixing. *Exp. Fluids*, 27:461 – 472, 1999.

Warner, H. R. J. Kinetic theory and rheology of dilute suspensions of finitely extendible dumbbells. *Ind. Eng. Chem. Fundam.*, 11:379 – 87, 1972.

Wedgewood, L. E. and Bird, R. B. From molecular models to the solution of flow problems. *Ind. Eng. Chem. Res.*, 27(7):1313–1320, 1988.

White, C. M. and Mungal, M. G. Mechanics and prediction of turbulent drag reduction with polymer additives. *Ann. Rev. Fluid Mech.*, 40(1):235–256, 2008.

Wilhelmson, R. B. and Ericksen, J. H. Direct solutions for Poisson's equation in three dimensions. *J. Comput. Phys.*, 25:319–331, 1977.

Williamson, J. H. Low-storage Runge-Kutta schemes. *J. Comput. Phys.*, 35:48–56, 1980.

Xu, J., Dong, S., Maxey, M. R., and Karniadakis, G. E. Turbulent drag reduction by constant near-wall forcing. *J. Fluid Mech.*, 582:79 – 101, 2007.

Zagarola, M. V. and Smits, A. J. Mean-flow scaling of turbulent pipe flow. *J. Fluid Mech.*, 373:33–79, 1998.

Zanoun, E. S., Durst, F., and Nagib, H. Evaluating the law of the wall in two-dimensional fully developed turbulent channel flows. *Phys. Fluids*, 15(10):3079–3089, 2003.

Zhou, Q. and Akhavan, R. A comparison of FENE and FENE-P dumbbell and chain models in turbulentflow. *J. Non-Newtonian Fluid Mech.*, 109(2-3):115 – 155, 2003.

Zimm, B. H. Dynamics of polymer molecules in dilute solution: Viscoelasticity, flow birefringence and dielectric loss. *J. Chem. Phys.*, 24(2):269–278, 1956.